Chem

CellPress

Article

Selective Surface PEGylation of UiO-66 Nanoparticles for Enhanced Stability, Cell Uptake, and pH-Responsive Drug Delivery

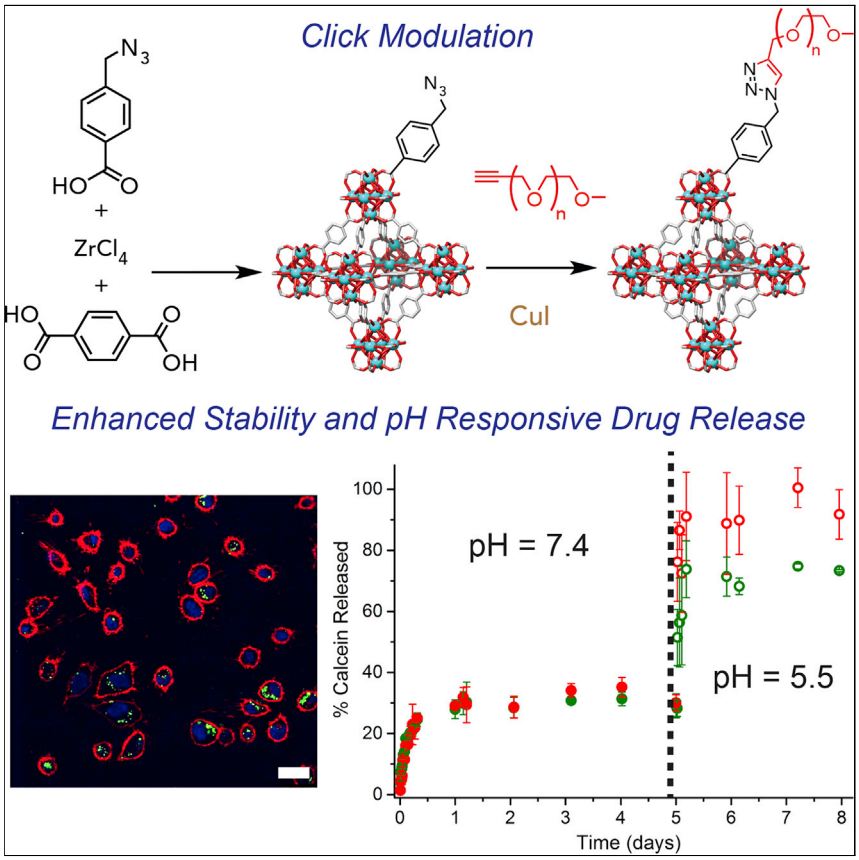

Porous nanoparticles that can store drug molecules have great potential in drug delivery, the use of nanocarriers to transport therapeutic agents around the body. Forgan and colleagues report on a method that controls the surface properties and functionality of metal-organic framework nanoparticles to enhance their stability, allow stimuli-responsive release of drug molecules, and enhance the anticancer therapeutic effect of loaded drugs by changing the route of cell uptake. Further development of these materials could enhance drug efficiencies and avoid unwanted side effects.

Isabel Abánades Lázaro, Salame Haddad, Sabrina Sacca, Claudia Orellana-Tavra, David Fairen-Jimenez, Ross S. Forgan

df334@cam.ac.uk (D.F.-J.)
ross.forgan@glasgow.ac.uk (R.S.F.)

HIGHLIGHTS

A surface modification protocol for MOFs compatible with cargo loading is reported

PEGylated UiO-66 nanoparticles show pH-responsive cargo release

Endocytosis routes are modified by the control of MOF surface chemistry

Enhanced cytotoxicity is observed for PEGylated UiO-66 loaded with dichloroacetate

Abánades Lázaro et al., Chem 2, 561–578
April 13, 2017
http://dx.doi.org/10.1016/j.chempr.2017.02.005

Chem

CellPress

Article

Selective Surface PEGylation of UiO-66 Nanoparticles for Enhanced Stability, Cell Uptake, and pH-Responsive Drug Delivery

Isabel Abánades Lázaro,[1] Salame Haddad,[2] Sabrina Sacca,[1] Claudia Orellana-Tavra,[2] David Fairen-Jimenez,[2,*] and Ross S. Forgan[1,3,*]

SUMMARY

The high storage capacities and excellent biocompatibilities of metal-organic frameworks (MOFs) have made them emerging candidates as drug-delivery vectors. Incorporation of surface functionality is a route to enhanced properties, and here we report on a surface-modification procedure—click modulation—that controls their size and surface chemistry. The zirconium terephthalate MOF UiO-66 is (1) synthesized as ~200 nm nanoparticles coated with functionalized modulators, (2) loaded with cargo, and (3) covalently surface modified with poly(ethylene glycol) (PEG) chains through mild bioconjugate reactions. At pH 7.4, the PEG chains endow the MOF with enhanced stability toward phosphates and overcome the "burst release" phenomenon by blocking interaction with the exterior of the nanoparticles, whereas at pH 5.5, stimuli-responsive drug release is achieved. The mode of cellular internalization is also tuned by nanoparticle surface chemistry, such that PEGylated UiO-66 potentially escapes lysosomal degradation through enhanced caveolae-mediated uptake. This makes it a highly promising vector, as demonstrated for dichloroacetic-acid-loaded materials, which exhibit enhanced cytotoxicity. The versatility of the click modulation protocol will allow a wide range of MOFs to be easily surface functionalized for a number of applications.

INTRODUCTION

Effective cancer therapy is one of the most challenging goals for the scientific community because of the lack of tumor selectivity of most therapeutics, which can lead to toxic dose dependence, serious hepatic problems, and diverse side effects.[1–3] Thus, drug-delivery systems have become one of the most promising applications for health care.[4–6] A large number of strategies have been studied, but for application, drug-delivery systems must overcome issues surrounding bioavailability,[7,8] the uncontrollable release of drugs (usually due to carrier instability),[9–11] loading capacities,[11–13] particle size,[14–16] nanoparticle cellular internalization routes,[14,17,18] and toxicity.[19,20] The exceptional storage capacities of metal-organic frameworks (MOFs), together with their robustness and structural tailorability, have made them attractive for a wide variety of applications,[21,22] including several promising breakthroughs in biomedicine.[9,10,23–33] One of their main advantages is that their cytotoxicity and properties can be tuned by the thoughtful choice of metal and linkers.[20,34,35]

Surface modifications of drug nanocarriers are of high importance because the carrier stability, drug-release kinetics, and particle cellular internalization can be

The Bigger Picture

Using artificial agents to deliver drugs selectively to sites of disease while protecting them from metabolism and clearance offers potential routes to new treatments. Porous metal-organic frameworks (MOFs) have emerged as potential candidates because they offer high storage capacities and easy clearance after delivery. We report on a method that controls the size and surface chemistry of MOFs and is compatible with cargo loading, showing that surface modification with biocompatible poly(ethylene glycol) chains improves stability toward phosphate and allows pH-responsive cargo release, which could enhance selectivity because cancerous cells are typically more acidic than healthy ones. Modes of cellular uptake are also altered, which could account for the enhanced cell death when polymer-coated MOFs are loaded with the anticancer drug dichloroacetic acid. Surface modification is mild and could be applied across a range of MOFs, opening up applications in selective molecular separation, blending into hybrids, and turn-on catalysis.

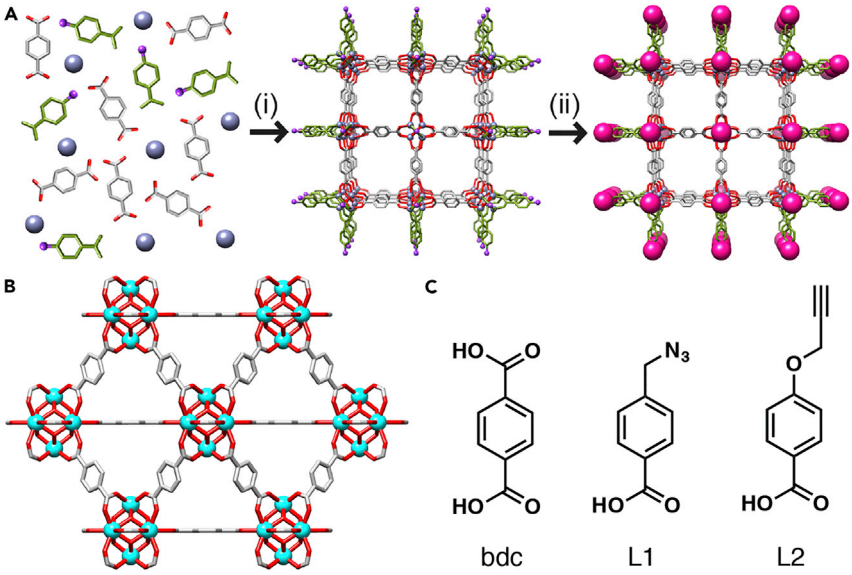

Figure 1. Click Modulation of UiO-66 MOFs

(A) Schematic of the "click modulation" protocol, where functionalized modulators are (i) incorporated onto MOF surfaces during synthesis and (ii) selectively chemically modified.
(B) The structure of UiO-66, which has been functionalized by click modulation.
(C) The ligand, bdc, and modulators (L1 and L2) applied in this study.

tuned.[9,18] Particle characteristics such as size, shape, and surface chemistry play key roles in determining the cellular-uptake pathways.[36–38] Although a considerable amount of work has been performed to modify the bulk structure and internal pore spaces of MOFs,[39–42] only a few studies have addressed their external surface chemistry, usually through surface-selective postsynthetic modification protocols designed for specific MOFs and surface substrates.[9,24,43–48] For example, coatings with different polymers have decreased immune system recognition and accumulation in the liver for nanoparticulate MOFs (NMOFs) and have shown promising in vitro and in vivo results in anticancer therapy.[9,24] In addition, they can be targeted to cancer cells by the attachment of different targeting units to their surface through postsynthetic modifications, avoiding non-specific distribution of the drug.[49,50]

The size and shape of NMOF particles can be tuned by the introduction of modulators—monotopic capping agents such as benzoic acid—to their syntheses.[51–55] Coordination modulation offers the prospect of decorating the external surfaces of NMOFs with desirable functionality during the synthetic process, but this remains a challenge.[56,57] Herein, we present a reproducible two-step method, which we have termed "click modulation," for the general surface modification of zirconium-based NMOFs (Figure 1A). This method introduces functionalized modulators to the NMOFs' external surfaces during the synthetic process to control particle size and subsequently transforms them in further postsynthetic modifications by using high-yielding "click" chemistry compatible with cargo-loaded NMOFs.

Incorporation of polymers onto the external surfaces of NMOFs has been suggested as a route to enhanced stability and effective application in drug delivery.[58] We have therefore used our click modulation protocol to covalently attach poly(ethylene glycol) (PEG) chains to the NMOFs' surfaces to improve their stability and drug-release kinetics and also facilitate pH-responsive release of cargo. The effect of

[1]WestCHEM School of Chemistry, University of Glasgow, Joseph Black Building, University Avenue, Glasgow G12 8QQ, UK

[2]Adsorption & Advanced Materials Laboratory, Department of Chemical Engineering & Biotechnology, University of Cambridge, Pembroke Street, Cambridge CB2 3RA, UK

[3]Lead Contact

*Correspondence: df334@cam.ac.uk (D.F.), ross.forgan@glasgow.ac.uk (R.S.F.)

http://dx.doi.org/10.1016/j.chempr.2017.02.005

postsynthetic surface modification on cancer cell endocytosis pathways was also studied,[14,38] revealing that cellular internalization routes of NMOFs can be mediated by their surface chemistry.

RESULTS AND DISCUSSION

The zirconium MOF UiO-66 (UiO stands for Universitetet i Oslo; Figure 1B)[59] is biocompatible and has a half maximal inhibitory concentration (IC_{50}) of 1.50 ± 0.15 mg/mL against the HeLa cell line after 24 hr of exposure.[60] Its idealized structure, $Zr_6O_4(OH)_4(bdc)_6$, where bdc stands for 1,4-benzenedicarboxylate, has been well characterized and possesses a remarkable thermal and chemical stability in comparison with that of other MOFs.[59,61,62] UiO-66 is also known to incorporate synthetic modulators at surface and defect sites[63–65] and so was chosen for study. *p*-Azidomethylbenzoic acid (L1) and *p*-propargyloxybenzoic acid (L2) were selected as click modulators (Figure 1C) for UiO-66 synthesis because of their structural similarities to the bdc linker and the fact that, if attached to the Zr_6 clusters, the desired functionalities should point outward,[46] resulting in accessible reactive groups as platforms for further postsynthetic modifications on its surface.

Synthesis and Characterization of UiO-66-L1 and UiO-66-L2

UiO-66 nanoparticles were synthesized under solvothermal conditions (Supplemental Information, Section S2) by the addition of 1, 3, or 5 equiv of the desired modulator (L1 or L2) and acetic acid (AcOH) as the co-modulator. Full characterization (Supplemental Information, Section S3) showed that the particles were highly crystalline, as confirmed by powder X-ray diffraction (PXRD) (Figure S1), and nuclear magnetic resonance (NMR) spectroscopy of acid-digested samples showed that modulator incorporation increased with the number of equivalents of modulator added to the reaction mixture (Figures S2 and S3); the estimated maximum content was 13.3 mol % of L1 (5 equiv added) in comparison with bdc and 17.1 mol % of L2 (5 equiv added). Infrared (IR) spectroscopy revealed an increase in the intensity of the azide vibration band at 2,100 cm^{-1} as the number of equivalents of L1 in UiO-66-L1 syntheses increased, whereas vibration bands characteristic of C≡C triple bonds were observed for UiO-66-L2 (Figure S4). Because of these encouraging results, all subsequent syntheses utilized 5 equiv of the corresponding modulator and 7% v/v of AcOH, and these samples are designated UiO-66-L1 and UiO-66-L2. A comparison sample, UiO-66-AcOH, was prepared in a synthesis modulated only by 7% v/v AcOH.

Quantifying modulator incorporation by thermogravimetric analysis (TGA) is difficult; compared with UiO-66-AcOH, modulated samples did not lose extra mass, indicating that the modulators, which are chemically similar to the bdc linkers and whose presence was confirmed by ^1H NMR spectroscopy, decompose at similar temperature (Figure S8). This suggests that L1 and L2 are attached to the external surface and at defect sites of the MOF and not simply loaded in the pores. UiO-66 has been reported to be highly porous; if defect free, its Brunauer-Emmet-Teller (BET) surface area is around 1,200 $m^2\ g^{-1}$, and its pore volume is 0.5 $cm^2\ g^{-1}$.[59] To characterize the porosity of UiO-66-L1 and UiO-66-L2, we collected N_2 adsorption isotherms at 77 K (Figure S9). The modulated samples exhibited higher surface areas (S_{BET} = 1,565 $m^2\ g^{-1}$ for UiO-66-L1 and 1,420 $m^2\ g^{-1}$ for UiO-66-L2), again suggesting that modulator incorporation induces defects rather than simply occupying and blocking pores,[57] and the pore-size distributions of the modulated samples were similar to those reported for UiO-66 (8 and 11 Å).[59]

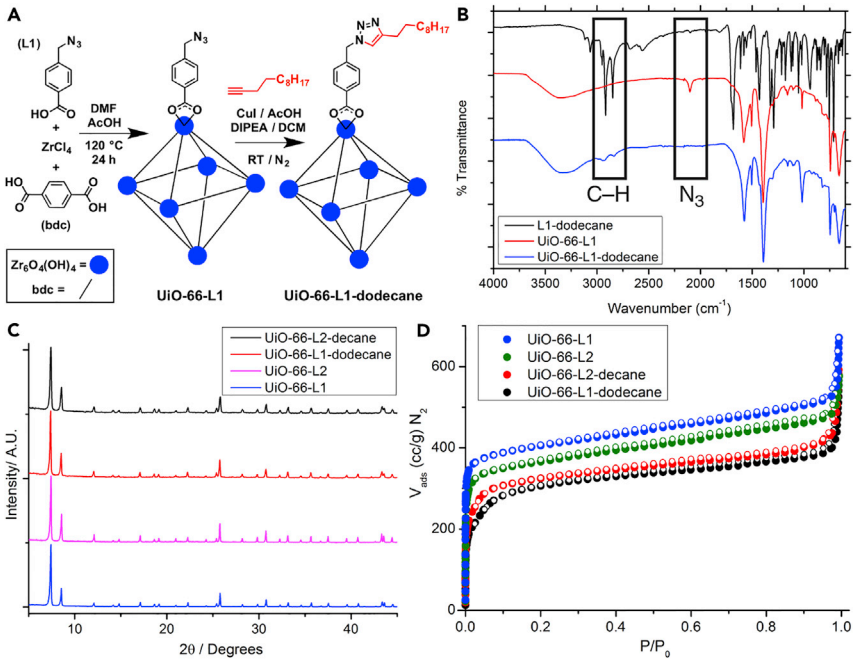

Figure 2. Proof-of-Concept Surface Modification of UiO-66 with Alkanes

(A) Schematic of the click modulation protocol in the preparation of UiO-66-L1-dodecane.

(B) Stacked IR spectra showing the disappearance of the azide stretch and appearance of C–H signals after the CuAAC surface reaction has taken place on UiO-66-L1.

(C) Stacked PXRD profiles of UiO-66-L1 and UiO-66-L2 before and after alkylation.

(D) N_2 adsorption isotherms (77 K) of the MOFs show a decrease in gravimetric uptake as additional mass is incorporated onto their surfaces. Closed symbols represent adsorption, and empty symbols represent desorption.

Proof-of-Concept Surface Functionalization

After confirming that the functionalized modulators were incorporated into the MOF structure, we attempted postsynthetic modification by copper(I)-catalyzed azide-alkyne cycloaddition (CuAAC)[66] (Supplemental Information, Section S4). Various catalysts were tested, including CuI and a mixture of $CuSO_4$ and sodium ascorbate, resulting in loss of the sample crystallinity each time. An efficient and economic approach, using CuI and 2 equiv of both acetic acid and *N,N*-diisopropylethylamine as an in situ stabilizing ligand for Cu(I),[67] was tolerated by the MOF structure, as confirmed by PXRD (Figure S10), and allowed further functionalization of the NMOFs.

Proof-of-concept reactions using this catalyst were carried out between UiO-66-L1 and 1-dodecyne (Figure 2A), as well as between UiO-66-L2 and 1-azidodecane. ^{1}H NMR spectra of acid-digested samples of UiO-66-L1-dodecane and UiO-66-L2-decane suggested significant conversions of the modulators into the respective triazole products; although the low modulator content makes analysis difficult, additional aromatic signals are present alongside peaks for the alkyl groups. Full conversion would not be expected, given that some modulators will be located at inaccessible internal defect sites rather than on the particle surface.

Fourier transform IR (FT-IR) spectra also showed the disappearance of signals for modulator azide and alkyne groups and the appearance of triazole bands and surface functionality, which compared well with spectra of authentic samples of

"clicked" modulators prepared separately in solution-phase reactions (Figure 2B), whereas high-resolution electrospray ionization mass spectrometry (HR-ESI-MS) of acid digests of the modified MOFs confirmed the presence of the triazole products. The crystallinity, as measured by PXRD (Figure 2C), and porosity (Figure 2D) of the samples after functionalization with alkyl chains were both maintained, such that surface areas were slightly lower (1,168 $m^2\ g^{-1}$ for UiO-66-L1-dodecane and 1,262 $m^2\ g^{-1}$ for UiO-66-L2-decane) that those of their precursors, UiO-66-L1 (1,565 $m^2\ g^{-1}$) and UiO-66-L2 (1,420 $m^2\ g^{-1}$). Surface functionalization with alkyl chains increases the mass of the particles, and so a decrease in gravimetric surface area is expected.[68] These decreases correlate well with the new mass-loss features observed in TGA profiles of UiO-66-L1-dodecane and UiO-66-L2-decane (10.1% and 10.0% w/w, respectively), which correspond to decomposition of the surface alkyl chains of the functionalized materials (Figures S12 and S13).

Scanning electron microscopy (SEM) showed that UiO-66-L1 forms well-defined nanoparticles around 100–200 nm in size (Figure S6) in a manner similar to a recently reported modulated synthesis of a related zirconium fumarate MOF.[69,70] In contrast, UiO-66-L2 has a larger particle size, around 400–600 nm (Figure S7), suggesting that click modulation can be used to control nanoparticle size as well as surface chemistry. Because the UiO-66-L1 nanoparticles have the appropriate size for drug-delivery applications,[16] we decided to continue our research toward surface functionalization of UiO-66-L1 for drug delivery. Specifically, PEG chains were chosen because they present an amphiphilic behavior that resembles that of human cellular membranes,[71] whereby the flexible and rapidly changing structure of the PEG hinders the immune system in the modeling of antibodies around it.[72]

The monomethyl ethers of PEG550 (average M_n = 550) and PEG2000 (average M_n = 2,000) were alkylated with propargyl units and used for conjugation with the azide-functionalized UiO-66-L1 under the previously determined Cu(I)-catalyzed conditions (Supplemental Information, Section S4). Full ^{1}H NMR spectroscopic analysis of the acid-digested products, UiO-66-L1-PEG550 and UiO-66-L1-PEG2000, is difficult because of the intensity of the polymer signals. However, a control experiment—stirring PEG2000-propargyl or PEG550-propargyl with UiO-66-L1 but without catalyst—revealed that, without Cu(I) catalyst, no polymer was present in the sample at all, confirming that covalent linkage is required for the PEG to remain attached to the MOF.

TGA profiles of UiO-66-L1-PEG550 and UiO-66-L1-PEG2000 (Figure 3A) showed extra mass losses (21.7% and 23.1% w/w, respectively) at temperatures corresponding to those reported for PEG in the literature,[73] whereas no extra mass losses were found in the control samples. HR-ESI-MS of digested UiO-66-L1-PEG550 (Figure 3B) confirmed that the click reaction between UiO-66-L1 and PEG550-propargyl had taken place, and although derivatives of the larger PEG2000 species did not ionize under the available conditions, functional-group conversion was observed by IR spectroscopy (Figure S16).

PXRD confirmed that the PEGylated NMOFs retained their crystallinity (Figure S17), and a decrease in their N_2 uptake was observed; the incorporated mass of the PEG chains led to BET surface areas of 865 $m^2\ g^{-1}$ for UiO-66-L1-PEG550 and 521 $m^2\ g^{-1}$ for UiO-66-L1-PEG2000 (Figure 3C). The pore-size distribution of UiO-66-L1-PEG550 corresponds with that reported for UiO-66, but in the case of UiO-66-L1-PEG2000, the adsorption and desorption isotherms reveal a type IV isotherm, typical of mesoporous materials, but with no closure point. In the case of nitrogen

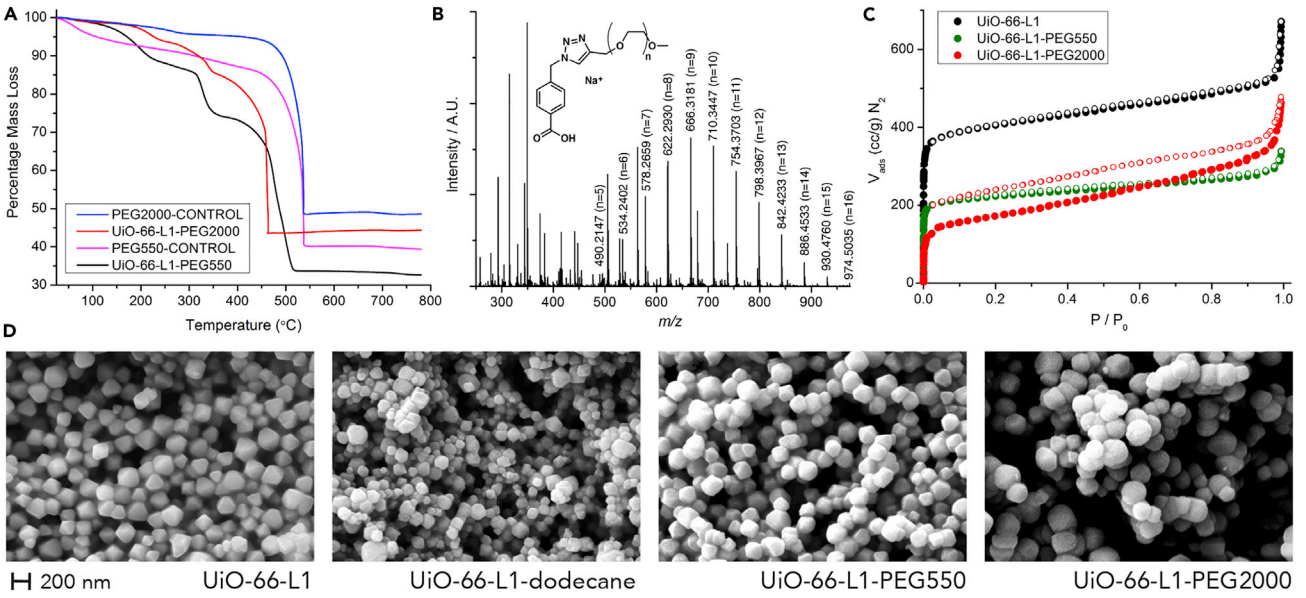

Figure 3. Surface Modification of UiO-66 with Poly(ethylene glycol)

(A) TGA profiles of UiO-66-L1-PEG550 and UiO-66-L1-PEG2000 are compared with those of control samples of UiO-66-L1 that had been exposed to propargyl-functionalized PEGs without any Cu(I) catalyst.

(B) HR-ESI-MS of digested UiO-66-L1-PEG550 confirms that the CuAAC reaction took place between the MOF and the PEG chain.

(C) N_2 uptake isotherms (77 K) of the PEGylated MOFs. Closed symbols represent adsorption, and empty symbols represent desorption.

(D) SEM images of UiO-66-L1 particles with differing surface functionality show the morphological changes as larger surface units are incorporated by click modulation. The scale bar (200 nm) applies to all images.

adsorption at 77 K, the lower closure point is usually located around $p/p_0 \sim 0.42$, and any hysteresis recorded below this point has been attributed to irreversible changes such as swelling of the adsorbent or surface impurities.[74] A similar phenomenon was found by Wang et al.[43] on UiO-66 functionalization with the phospholipid dihydroxyphenylalanine (DOPA), although to a lesser degree. The fact that PEG2000 chains are considerably bigger in size than DOPA could explain why it is more pronounced in this case.

Interestingly, the physical effects on nanoparticle morphology can be observed by SEM imaging (Figure 3D). As the chain length of the surface functionality increases, the particles become more rounded in shape with less-defined edges and vertices, because their surface features become dominated by the bulk of their capping polymers rather than the underlying MOF crystal structure. Image analysis (Figures S18–S20) also showed a gradual increase in particle size from 146.6 ± 29.3 nm for UiO-66-L1 to 160.2 ± 26.9 nm for UiO-66-L1-PEG550 and 172.9 ± 36.8 nm for UiO-66-L1-PEG2000, consistent with the addition of surface polymer chains of increasing size.

Solution stability and aggregation were investigated by dynamic light scattering (DLS). Measurements in methanol (0.25 mg/mL; Figure S21) showed stable dispersions of PEGylated particles at sizes around 150 nm, correlating well with the SEM data[70] and confirming that no aggregation takes place; in contrast, the unfunctionalized materials UiO-66-AcOH (~800 nm) and UiO-66-L1 (~300 nm) showed aggregation. The power of the surface functionalization protocol was further demonstrated by DLS measurements in aqueous media (Figures S22 and S23). UiO-66-L1 was observed to sediment and precipitate from 0.25 mg/mL aqueous

dispersions over time, with aggregates around 2,000–3,000 nm. UiO-66-L1-PEG550 aggregated to a lesser extent, with stable assemblies around 1,000–1,500 nm, but the larger PEG chains of UiO-66-L1-PEG2000 conferred further dispersive stability, such that assemblies around 250 nm were observed to aggregate to around 400 nm during the experiments. The dependence of aggregation on PEG chain size clearly demonstrates the stabilizing effects of surface modification and the advantages of MOF PEGylation for drug delivery.

In addition, the cytotoxicities of UiO-66-L1-PEG550 and UiO-66-L1-PEG2000, as well as modulators L1 and L2, were assessed by the bioreduction of a tetrazolium compound (MTS), known as the MTS assay (Figures S24 and S25). None of the materials showed any toxicity toward HeLa cells at concentrations up to 1 mg/mL.

The successful covalent surface modification of UiO-66 with both alkyl and PEG chains confirms the versatility and general applicability of the click modulation process. PEG chains have previously been incorporated onto silica-coated UiO-66(Hf), and although this approach facilitated in vivo imaging by computed tomography,[75] it might not be suitable for drug delivery because the silica coating can block access to the pores of the MOF and could affect clearance.

Degradation Kinetics of PEGylated and Uncoated UiO-66-L1

To be an efficient injectable treatment, the nanocarrier should be stable at the first stages of the treatment; ideally, it should not be degraded in extracellular conditions (i.e., blood [pH 7.4]) in order to avoid renal clearance of the drug yet not be persistent enough to be accumulated over longer treatment periods. The nature of the metal-linker coordination bonds in MOFs ensures total degradation of the structure at sufficiently acidic pH ranges as a result of linker protonation,[76] but strongly coordinating molecules, such as phosphates, are also able to displace the linkers in the structure at extracellular pH.[24] Although the rapid degradation of MOFs under physiological conditions ensures no accumulation of the carrier after it has reached its target and released the drug,[10,77] their instability toward phosphates, which are present in the blood, typically hinders NMOF bioapplications because of fast-release kinetics,[77] and several approaches, such as amorphisation[60] or silica coating,[29,39,75,78] among others, have been studied for improving their stability to phosphate.

The stabilities of UiO-66-L1, UiO-66-L1-PEG550, and UiO-66-L1-PEG2000 were determined in phosphate buffered saline (PBS) at pH 7.4 (Supplemental Information, Section S5) via measurement of the release of bdc linkers by UV-Vis spectroscopy (Figure 4A). L1 was found to have a UV-Vis absorbance profile and extinction coefficient similar to those of bdc and so does not significantly affect the measurements. UiO-66-L1 exhibited an exponential degradation profile reaching a plateau around 85% bdc release after 6 hr of exposure. On the other hand, PEGylated samples exhibited sigmoidal degradation profiles. We observed that the PEG-modified NMOFs degraded at much slower rates during the first 2 hr, after which they reached plateaus similar to those of the uncoated samples at the end of the experiment (Figures S26–S30).

PXRD analysis (Figure 4B) also showed that crystallinity is retained for longer when the samples have been PEGylated, particularly in the first few hours. We expect that the surface corona of covalently attached PEG chains hinders phosphate attack of the Zr_6 clusters of the UiO-66 samples, given that the phosphate groups must first diffuse through the PEG coating to reach the zirconium positions, displace the

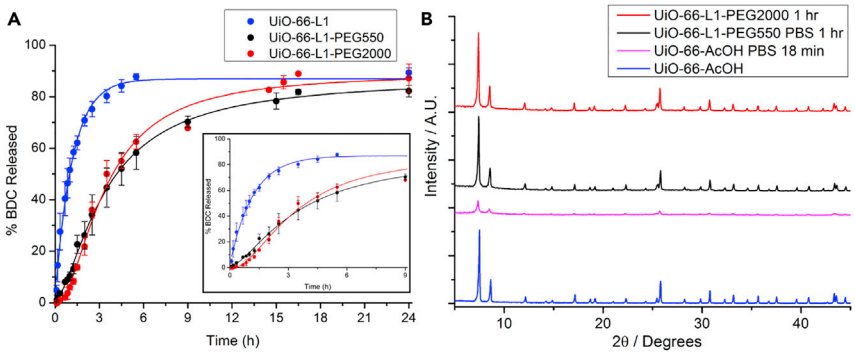

Figure 4. Enhanced Stability of PEGylated UiO-66

(A) Degradation profiles of UiO-66-L1, UiO-66-L1-PEG550, and UiO-66-L1-PEG2000 in PBS (pH 7.4). Error bars denote standard deviations from triplicate experiments.

(B) PXRD profiles of the MOFs after immersion in PBS for differing times show the improved stability of the PEGylated MOFs.

modulators and linkers, and coordinate to the zirconium ions similarly to the uncoated NMOF. This enhanced stability means that the burst effect, due to carrier degradation,[79] could be avoided at the first stages of the treatment, improving the treatment efficiency and reducing undesirable side effects while ensuring that the framework can degrade, release cargo, and be cleared over larger periods of exposure.

Synthesis, Functionalization, and Characterization of Calcein-Containing NMOFs

In order to determine the effect of the PEGylation upon drug-release kinetics and cell internalization routes, we chose calcein as a model drug because of its structural similarities to doxorubicin.[2,60] Calcein is hydrophilic and does not permeate the cell membrane; rather, it requires a drug-delivery vehicle to facilitate its entry into cells. In addition, like doxorubicin, it is a fluorescent molecule, and because of its self-quenching character it can be detected only when it is released from the delivery vector, allowing the measurement of cytoplasmic fluorescence by confocal microscopy or flow cytometry.[80] The versatility of the click modulation technique is further demonstrated by its compatibility with cargo loading (Supplemental Information, Section S6). Simply stirring azide-modified UiO-66-L1 in a concentrated methanolic calcein solution resulted in higher incorporation of calcein (16.0% w/w as determined by UV-Vis spectroscopy) than previously reported in the literature for UiO-66, most likely as a result of the increased porosity of UiO-66-L1.[60] We named the calcein-loaded sample cal@UiO-66-L1. The functionalized modulator L1 remained attached to the MOF framework after calcein uptake, as determined by ^{1}H NMR spectra of the digested samples, and the azide functionality was used once again to incorporate PEG chains of different lengths according to the CuAAC protocol. Crystallinity was preserved after calcein loading (Figure S32) and PEGylation, and their size, analyzed by SEM, was found not to change (Figure S33). Calcein content was analyzed by UV-Vis spectroscopy and found to be 13.3% w/w for cal@UiO-66-L1-PEG550 and 10.3% w/w for cal@UiO-66-L1-PEG2000 (Figure S34). This confirms that click modulation is compatible with cargo loading, and the decreasing loading values are commensurate with the increasing mass of the particles after PEGylation.

Confirmation of calcein loading by TGA analysis was complicated by the absence of the first calcein thermal decomposition step in the loaded MOF samples

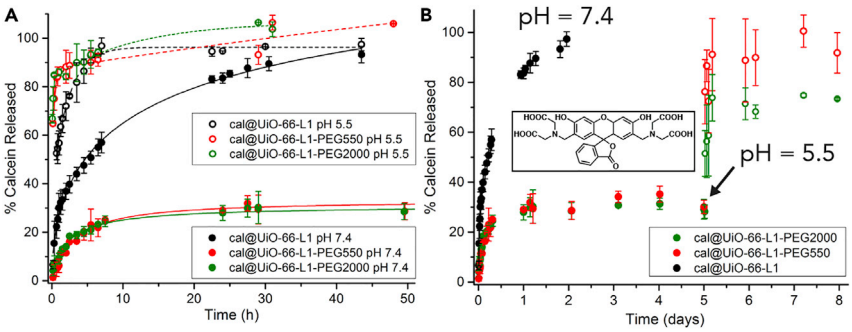

Figure 5. pH-Responsive Release of Calcein from PEGylated UiO-66

(A) Calcein-release profiles from UiO-66-L1, UiO-66-L1-PEG550, and UiO-66-L1-PEG2000 in PBS (pH 7.4 and 5.5).

(B) pH-responsive release of calcein from the PEGylated MOFs. Inset: chemical structure of calcein. Error bars denote standard deviations from triplicate experiments.

(Figure S35), indicating that calcein is attached to the external surface and at defect sites. Calcein decomposition occurred over a temperature range similar to that observed previously for PEG groups, making exact quantification troublesome but confirming the presence of the surface PEG functionality in cal@UiO-66-L1-PEG550 and cal@UiO-66-L1-PEG2000 (Figure S36). N_2 adsorption isotherms (77 K) confirmed that cal@UiO-66-L1 exhibited a decrease in surface area (S_{BET} = 1,002 $m^2\ g^{-1}$) but maintained the pore-size distribution characteristic of UiO-66, again suggesting that calcein is not significantly blocking the pores but attaching to the particle surface and localizing at defects (Figure S37). The porosity of both PEGylated calcein-loaded samples (S_{BET} = 826 $m^2\ g^{-1}$ for cal@UiO-66-L1-PEG550 and S_{BET} = 683 $m^2\ g^{-1}$ for cal@UiO-66-L1-PEG2000) decreased similarly to that of the empty PEGylated UiO-66-L1 samples, confirming PEG surface attachment can occur without displacing molecular cargo.

pH-Dependent Calcein-Release Profiles

The effect of surface modification on calcein release was monitored in PBS at pH 7.4 and 5.5 according to a UV-Vis spectrophotometric analysis protocol similar to the degradation experiments (Supplemental Information, Section S7). Monitoring release at different pH values is very important given that extracellular pH is ~7.4, intracellular pH is ~6.8, and the pH of cancer cells is close to 5.5,[81] providing a potential mechanism for targeted drug delivery. The release of calcein from both coated and uncoated samples was affected by the pH (Figure 5A); however, the release at pH 7.4 was drastically decreased for the PEGylated samples. Both cal@UiO-66-L1-PEG550 and cal@UiO-66-L1-PEG2000 initially released calcein slowly at pH 7.4 and did not release more than ~30% of their total cargo after 5 days. In contrast, they rapidly released ~80% of cargo within an hour at pH 5.5 and released nearly the full amount in pH 5.5 after 2 days (Figures S38–S50).

If this behavior can be retained in vivo, PEGylated UiO-66 samples could be expected to store the majority of cargo in extracellular conditions and thus avoid the non-selective distribution of therapeutics while being able to release it once it has reached its target. The stimuli-responsive release of calcein from the PEGylated MOFs was therefore assessed by a similar experiment, where the pH of the PBS solution was adjusted from 7.4 to 5.5 after 5 days (Figure 5B). An immediate, rapid release of calcein was observed, whereby slightly less calcein was released from

UiO-66-L1-PEG2000 than from the analog with the shorter chain. Nonetheless, this result is highly promising for drug-delivery applications should the particles be efficiently internalized by cells.

To gain further insight into the mechanism of release, we subjected samples of the MOFs to simulated release conditions at pH 7.4: cal@UiO-66-L1 after 1 day and cal@UiO-66-L1-PEG2000 after 2 days (Supplemental Information, Section S8). The amount of calcein released from both individual experiments determined by UV-Vis spectroscopy (67.5% from cal@UiO-66-L1 and 42.7% from cal@UiO-66-L1-PEG2000) is in concordance with the release profiles. Both samples showed a decrease in crystallinity by PXRD after calcein release, although the characteristic UiO-66 reflection peaks could be determined (Figure S51), meaning that the core of the materials remained crystalline. TGA showed the disappearance of the PEG moiety from cal@UiO-66-L1-PEG2000 and an increase on the metal residue for both samples (Figure S52), suggesting some degradation. Both samples remained porous (Figure S53); the surface area of cal@UiO-66-L1 (S_{BET} = 1,155 m^2 g^{-1}) increased from the release of significant amounts of calcein mass, and the surface area of cal@UiO-66-L1-PEG2000 (S_{BET} = 554 m^2 g^{-1}) decreased slightly, possibly because of pore blocking or the incorporation of additional mass, such as phosphates.

We hypothesize that, at pH 7.4, the phosphates present in PBS attack the zirconium positions[24] and displace the surface ligands and the calcein. When UiO-66 is not PEGylated, the MOF is much more accessible (both internally and externally) and therefore so are the zirconium clusters, enabling a faster exchange between phosphates and ligands, modulators, and calcein. On the other hand, for surface-modified cal@UiO-66-L1-PEG2000, the phosphates must diffuse through the PEG coating before reaching the MOF. We hypothesize that a corona of coordinating phosphates is then formed, obstructing the MOF and hindering further phosphate attack to release remaining calcein molecules. Indeed, FT-IR spectra of cal@UiO-66-L1-PEG2000 after 1 day in PBS at pH 7.4 showed more significant signals for phosphates than for cal@UiO-66-L1 under the same conditions (Figure S54), suggesting that the PEG coating induces a corona build-up and that unmodified UiO-66 simply undergoes surface exchange (Supplemental Information, Section S8). When the pH is more acidic, the carboxylate units of bdc ligands, surface functionality, and calcein are easier to protonate, and therefore MOF degradation and calcein release are much more pronounced.[76]

Endocytosis Studies

Confocal fluorescence microscopy has been used to confirm successful internalization of the MOF nanoparticles by HeLa cells and subsequent calcein release (Supplemental Information, Section S9). Figure 6 shows the confocal microscopy images of HeLa cells incubated with, from top to bottom, nothing (control), free calcein, cal@UiO-66-L1, cal@UiO-66-L1-PEG550, and cal@UiO-66-L1-PEG2000. We used Hoechst 33342 (H33342) and CellMask to stain the nucleus and membrane of the cells, respectively. We used CellMask as a viability control to probe the cell membrane integrity and show that the MOFs were inside the cells. The effectiveness of calcein as a probe is demonstrated by the fact that free calcein was not taken up by cells, in concert with previous reports,[60,80,82] so any green fluorescence within cells comes from released calcein from internalized MOF materials. UiO-66-L1, UiO-66-L1-PEG550, and UiO-66-L1-PEG2000 all transported calcein into HeLa cells, as seen by the green fluorescence, whereas the control cells and those incubated with free calcein showed no signal.

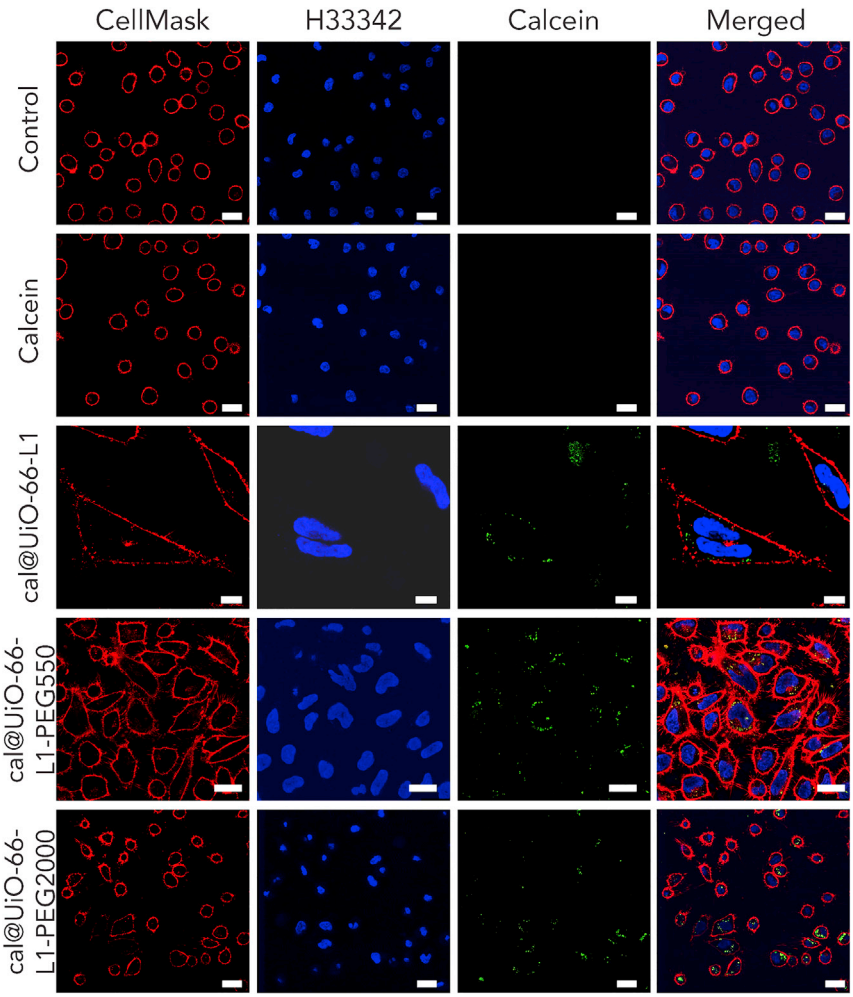

Figure 6. Confocal Microscopy Images of HeLa Cells Incubated with Different Materials

From top to bottom: control, free calcein, cal@UiO-66-L1, cal@UiO-66-L1-PEG550, and cal@UiO-66-L1-PEG2000. Cells were subsequently stained with Hoechst 33342 (5 μg/mL) and CellMask orange (1×). Scale bars represent 25 μm in all images except for cal@UiO-66-L1, in which it represents 10 μm.

The transport of calcein into NMOFs allows the study of endocytosis pathways by fluorescence-activated cell sorting (FACS). There are three main classes of endocytosis pathways: (1) clathrin-mediated, (2) caveolae-mediated, and (3) clathrin- and caveolae-independent endocytosis such as macropinocytosis.[38,83,84] Clathrin-mediated endocytosis involves recognition of the cargo by cell-surface receptors, which internalize it into protein (clathrin)-coated vesicles 60–200 nm in size, called early endosomes.[85] These early endosomes then mature into late endosomes and finally fuse with lysosomes, causing degradation of the drug-delivery system along with its loaded cargo, thus nullifying its therapeutic effect.[85] On the other hand, caveolae-mediated endocytosis is associated with the formation of lipid-raft-enriched flask-shaped invaginations (50–100 nm) coated with a protein called caveolin.[86] Particles internalized via caveolae-mediated endocytosis can later be delivered to different locations in a cell, including a pH-neutral compartment called the caveosome, and then transported to a final intracellular location, potentially avoiding lysosomal degradation.[87,88]

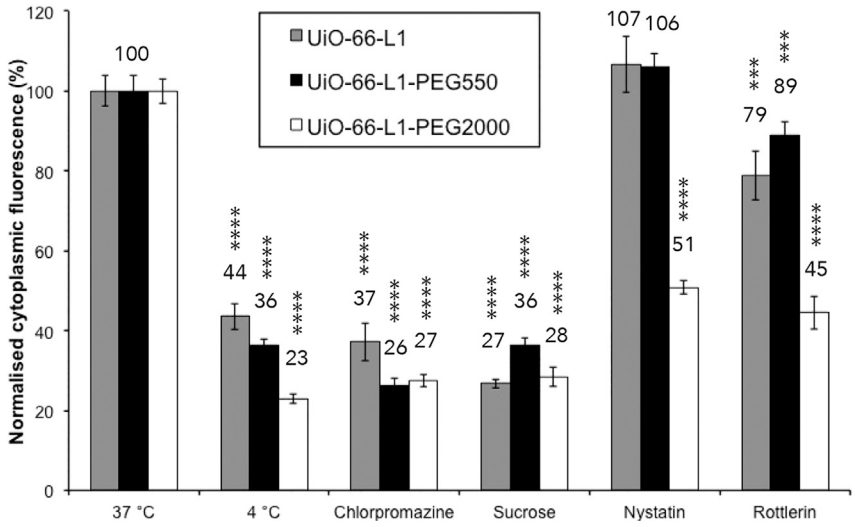

Figure 7. Effects of Pharmacological Endocytosis Inhibitors on the Uptake of cal@UiO-66-L1, cal@UiO-66-L1-PEG550, and cal@UiO-66-L1-PEG2000 into HeLa Cells, as Measured by FACS

The statistical significance was determined by ordinary one-way ANOVA and is indicated on the graph: ***$p < 0.001$ and ****$p < 0.0001$.

To study the internalization routes of the PEGylated and unPEGylated NMOFs, we used different pharmacologic inhibitors according to our previous work (Supplemental Information, Section S9).[38] First, we used sucrose[89] and chlorpromazine[90] to independently inhibit the clathrin-mediated pathway. Second, we used nystatin to inhibit the caveolae-mediated pathway.[91] Finally, we employed rottlerin[92,93] to prevent macropinocytosis. Tracers known to selectively follow each pathway were used as positive controls for the inhibitors: transferrin and ceramide for clathrin- and caveolae-mediated pathways, respectively, and dextran for macropinocytosis. Cells were incubated with each inhibitor for 30 min and then for 90 min together with the NMOF (Supplemental Information, Section S9). Because nanoparticle size is known to affect cell internalization routes,[38] for example, the recent report of enhanced uptake of 90 nm nanoparticles of a Zr-porphyrin MOF into HeLa cells,[94] we performed all experiments on one base batch of UiO-66-L1, surface modified and loaded as necessary, to ensure that particle size was relatively homogeneous.

Figure 7 shows the normalized internal fluorescence, obtained through FACS, of HeLa cells after the uptake of cal@UiO-66-L1, cal@UiO-66-L1-PEG550, and cal@UiO-66-L1-PEG2000 in the presence and absence of the pharmacologic endocytosis inhibitors. The uptake of all three particles at 4°C was significantly reduced, which confirms that they are internalized via an energy-dependent endocytosis process. The uptake of cal@UiO-66-L1 after exposure to sucrose and chlorpromazine was reduced to ~27% ± 1% and 37% ± 5%, respectively, whereas exposure to nystatin had no effect (~107% ± 7%), revealing that the unfunctionalized MOF is not internalized through the caveolae-mediated route. Rottlerin decreased its uptake to ~79% ± 6%. For cal@UiO-66-L1-PEG550, the uptake after exposure to sucrose and chlorpromazine decreased to ~36% ± 2% and 26% ± 2%, respectively, whereas there was no reduction in uptake upon exposure to nystatin (~106% ± 3%). Rottlerin slightly decreased the uptake to ~89% ± 4%. These values are similar to those for cal@UiO-66-L1, suggesting that the PEG550 coating did not affect the route of endocytosis.

Finally, for cal@UiO-66-L1-PEG2000, exposing the cells to sucrose and chlorpromazine decreased the uptake to ~28% ± 2% and 27% ± 2%, respectively. Interestingly, significant changes were found, whereby nystatin and rottlerin reduced the uptake to ~51% ± 2% and 45% ± 4%, respectively, showing that the PEGylated MOF is partially internalized through caveolae-mediated endocytosis. This indicates that the UiO-66 internalization pathway is significantly affected by the functionality attached to its surface, and the longer PEG chains (M_n ~ 2,000) allow the NMOFs to partially avoid lysosomal degradation. The amphiphilic nature of cal@UiO-66-L1-PEG2000, in contrast to the hydrophilic surface of the uncoated sample, is thought to be more compatible with the caveolae-mediated route. In addition, part of the cellular trafficking of all three MOFs occurs through macropinocytosis because the uptake is affected by the presence of rottlerin. However, this is a non-selective process allowing the internalization of large quantities of material independently of its constitution.[95] Macropinocytosis could be a consequence of aggregation of nanoparticles if the effects observed by DLS also occur in this more dilute environment, although it has not been observed as a significant pathway for the other NMOF samples, which exhibit greater aggregation than UiO-66-L1-PEG2000.

We used laser confocal microscopy with LysoTracker-Deep red to qualitatively determine the degree of co-localization between the calcein-loaded NMOF particles (green) and the lysosomes (Figure S56). After 2 hr of incubation, a high level of co-localization was found for all three MOFs, given that FACS confirmed that clathrin-mediated uptake took place in all NMOFs. However, in the case of cal@UiO-66-L1-PEG2000, a higher degree of localized light-green particles outside the lysosomes was also observed, suggesting altered uptake mechanisms.

Therapeutic Efficacy of Drug-Loaded NMOFs

To investigate the effect of this alternative uptake mechanism and particle stability on the therapeutic efficacy of the PEGylated NMOFs, we selected dichloroacetic acid (DCA) for delivery because it is an anticancer drug that is cytotoxic only once it is internalized by cells.[96] DCA turns on the apoptosis systems of cancer cells, which is otherwise suppressed, thus allowing them to die.[97,98] However, its hydrophilicity means it is rapidly cleared with a half-life from the first dose of less than 1 hr, and it can induce neurotoxicity by crossing the blood-brain barrier,[99] so DCA is well suited for use in a nanocarrier system.

DCA was added (Supplemental Information, Section S10) to hydrothermal syntheses in place of acetic acid to yield DCA@UiO-66-L1. The presence of both DCA and L1 was confirmed by ^{1}H NMR spectroscopy (Figure S57), and the 150 nm particles observed by SEM were found to be crystalline by PXRD (Figure S58). The material was PEGylated under the CuAAC conditions used previously to yield DCA@UiO-66-L1-PEG2000. TGA confirmed the presence of the PEG chain and allowed an estimation of DCA loading; these values were confirmed by inductively coupled plasma mass spectrometry for measuring the chlorine content, giving DCA loadings of 13.7% w/w for DCA@UiO-66-L1 and 12.1% w/w for DCA@UiO-66-L1-PEG2000 (Figure S59). The cytotoxicities of the two materials were determined by MTS assay (Figure 8) against HeLa cells, where it was found that the PEGylated material induced significant cell death at NMOF concentrations of 0.75 mg/mL and above, whereas the uncoated material did not. In comparison, DCA alone has been found to have an IC_{50} of 23.0 ± 4.0 mM against methylcholanthrene fibrosarcoma cells, a considerably higher dose.[98] We expect that the enhanced stability and cellular internalization of the PEGylated MOF contributes significantly to the improved therapeutic effect.

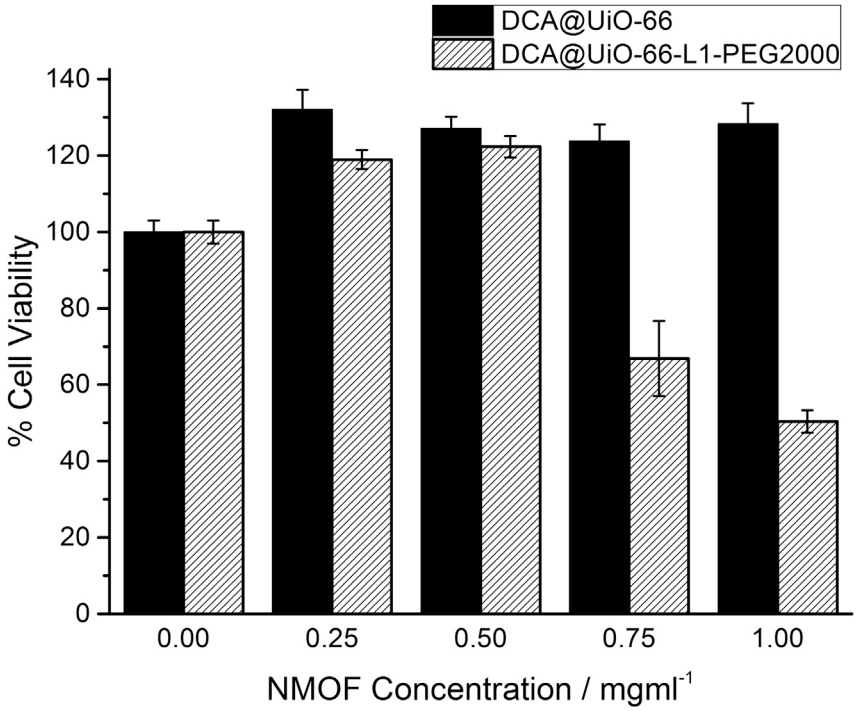

Figure 8. Metabolic Activity of HeLa Cells after 72 hr of Exposure to DCA@UiO-66-L1 and DCA@UiO-66-L1-PEG2000, as Measured by MTS Assay

Conclusions

We have presented a reproducible and innovative protocol—click modulation—to selectively introduce surface functionality to the Zr MOF UiO-66. A range of experiments have shown that differing chemical functionality can be incorporated in the MOF via the CuAAC reaction with functionalized modulators and that the two-stage process is compatible with cargo loading. Surface modification has been shown to be of prime importance for drug-delivery applications, specifically for UiO-66 nanoparticles loaded with calcein or DCA and coated with PEG chains of different lengths.

PEGylation has been shown to improve the stability of UiO-66 toward phosphate-induced degradation and dispersion in aqueous media, and calcein release has been proven to be pH dependent. In contrast to bare nanoparticles, PEGylated UiO-66 samples did not release more than ~40% of their calcein cargo after 5 days at pH 7.4, yet they released the full amount after 2 days in pH 5.5. In addition, pH-responsive release was achieved in this pH region, mirroring the change in conditions from blood-stream circulation to cancer cellular internalization to allow stimuli-responsive drug delivery. The surface chemistry also altered the cell-uptake routes of the nanoparticles; coating UiO-66 with PEG2000 enhanced caveolae-mediated endocytosis, allowing the NMOF to partially escape the lysosome, thus avoiding degradation of the drug and improving the possibility of reaching other cellular organelles. This effect was dependent on the length of the PEG chain; UiO-66 modified with PEG550 did not exhibit similarly enhanced caveolae-mediated uptake. PEGylation is compatible with loading of the anticancer drug DCA, and compared with DCA@UiO-66-L1, DCA@UiO-66-L1-PEG2000 exhibits significant cytotoxicity at concentrations above 0.75 mg/mL, possibly as a consequence of the differing cell-uptake routes, and enhances the therapeutic effect of DCA.

It is clear that functionalizing MOF nanoparticles with polymer chains can dramatically improve their suitability for biological applications. Our own results show improved stability, drug release, and cell-uptake properties with biocompatible PEG chains, and recent work has shown that polyaniline-modified UiO-66 is effective and safe for anticancer photothermal therapy.[100] We expect the versatility of the click modulation protocol to allow a variety of MOFs to be selectively surface functionalized with a variety of chemical units and have immediate application not only in biomedical settings but also in selective adsorption and separation processes and catalysis. Indeed, during the course of our study, a similar technique was applied to the functionalization of covalent organic frameworks.[101]

EXPERIMENTAL PROCEDURES

Full experimental procedures are provided in the Supplemental Information.

SUPPLEMENTAL INFORMATION

Supplemental Information includes Supplemental Experimental Procedures, 60 figures, and 2 tables and can be found with this article online at http://dx.doi.org/10.1016/j.chempr.2017.02.005.

AUTHOR CONTRIBUTIONS

Conceptualization, R.S.F.; Methodology, R.S.F. and D.F.-J.; Investigation, I.A.L., S.H., S.S., and C.O.-T.; Writing – Original Draft, I.A.L. and R.S.F.; Writing – Review & Editing, I.A.L., S.H., S.S., C.O.-T., D.F.-J., and R.S.F.; Supervision, R.S.F. and D.F.-J.; Project Administration, R.S.F. and D.F.-J.; Funding Acquisition, R.S.F.

ACKNOWLEDGMENTS

R.S.F. and D.F.-J. thank the Royal Society for the receipt of University Research Fellowships. R.S.F. and I.A.L. thank the University of Glasgow for funding. This project received funding in part from the European Research Council (ERC) under the European Union's Horizon 2020 Programme for Research and Innovation (grant agreement no. 677289, SCoTMOF, ERC-2015-STG).

Received: September 30, 2016
Revised: November 15, 2016
Accepted: February 14, 2017
Published: April 13, 2017

REFERENCES AND NOTES

1. Castaing, N., Merlet, D., and Cambar, J. (1990). Cis-platin cytotoxicity in human and rat tubular cell cultures. Toxicol. In Vitro *4*, 396–398.

2. Poljaková, J., Eckschlager, T., Hřebačková, J., Hraběta, J., and Stiborová, M. (2008). The comparison of cytotoxicity of the anticancer drugs doxorubicin and ellipticine to human neuroblastoma cells. Interdiscip. Toxicol. *1*, 186.

3. Sun, C.C., Bodurka, D.C., Weaver, C.B., Rasu, R., Wolf, J.K., Bevers, M.W., Smith, J.A., Wharton, J.T., and Rubenstein, E.B. (2005). Rankings and symptom assessments of side effects from chemotherapy: insights from experienced patients with ovarian cancer. Support. Care Cancer *13*, 219.

4. Rocca, J.D., Liu, D., and Lin, W. (2011). Nanoscale metal–organic frameworks for biomedical imaging and drug delivery. Acc. Chem. Res. *44*, 957.

5. Krukiewicz, K., and Zak, J.K. (2016). Biomaterial-based regional chemotherapy: local anticancer drug delivery to enhance chemotherapy and minimize its side-effects. Mater. Sci. Eng. C Mater. Biol. Appl. *62*, 927.

6. Peer, D., Karp, J.M., Hong, S., Farokhzad, O.C., Margalit, R., and Langer, R. (2007). Nanocarriers as an emerging platform for cancer therapy. Nat. Nano *2*, 751.

7. Dobrovolskaia, M.A., and McNeil, S.E. (2007). Immunological properties of engineered nanomaterials. Nat. Nano *2*, 469.

8. Qu, G., Zhang, C., Yuan, L., He, J., Wang, Z., Wang, L., Liu, S., and Jiang, G. (2012). Quantum dots impair macrophagic morphology and the ability of phagocytosis by inhibiting the Rho-associated kinase signaling. Nanoscale *4*, 2239.

9. Horcajada, P., Chalati, T., Serre, C., Gillet, B., Sebrie, C., Baati, T., Eubank, J.F., Heurtaux, D., Clayette, P., Kreuz, C., et al. (2010). Porous metal-organic-framework nanoscale carriers as a potential platform for drug delivery and imaging. Nat. Mater. *9*, 172.

10. McKinlay, A.C., Morris, R.E., Horcajada, P., Férey, G., Gref, R., Couvreur, P., and Serre, C. (2010). BioMOFs: metal–organic frameworks for biological and medical applications. Angew. Chem. Int. Ed. *49*, 6260.

11. Maruyama, K. (2011). Intracellular targeting delivery of liposomal drugs to solid tumors based on EPR effects. Adv. Drug Deliv. Rev. *63*, 161.

12. Sur, S., Fries, A.C., Kinzler, K.W., Zhou, S., and Vogelstein, B. (2014). Remote loading of preencapsulated drugs into stealth liposomes. Proc. Natl. Acad. Sci. USA *111*, 2283.

13. Morabito, J.V., Chou, L.-Y., Li, Z., Manna, C.M., Petroff, C.A., Kyada, R.J., Palomba, J.M., Byers, J.A., and Tsung, C.-K. (2014). Molecular encapsulation beyond the aperture size limit through dissociative linker exchange in metal–organic framework crystals. J. Am. Chem. Soc. *136*, 12540.

14. Canton, I., and Battaglia, G. (2012). Endocytosis at the nanoscale. Chem. Soc. Rev. *41*, 2718.

15. Chithrani, B.D., Ghazani, A.A., and Chan, W.C.W. (2006). Determining the size and shape dependence of gold nanoparticle uptake into mammalian cells. Nano. Lett. *6*, 662.

16. Yuan, F., Dellian, M., Fukumura, D., Leunig, M., Berk, D.A., Torchilin, V.P., and Jain, R.K. (1995). Vascular permeability in a human tumor xenograft: molecular size dependence and cutoff size. Cancer Res. *55*, 3752.

17. Wu, P.-C., Shieh, D.-B., and Cheng, F.-Y. (2014). Nanomaterial-mediated photothermal cancer treatment: the pivotal role of cellular uptake on photothermal therapeutic efficacy. RSC Adv. *4*, 53297.

18. Yin Win, K., and Feng, S.-S. (2005). Effects of particle size and surface coating on cellular uptake of polymeric nanoparticles for oral delivery of anticancer drugs. Biomaterials *26*, 2713.

19. Arora, S., Rajwade, J.M., and Paknikar, K.M. (2012). Nanotoxicology and in vitro studies: the need of the hour. Toxicol. Appl. Pharmacol. *258*, 151.

20. Tamames-Tabar, C., Cunha, D., Imbuluzqueta, E., Ragon, F., Serre, C., Blanco-Prieto, M.J., and Horcajada, P. (2014). Cytotoxicity of nanoscaled metal-organic frameworks. J. Mater. Chem. B *2*, 262.

21. Lee, J., Farha, O.K., Roberts, J., Scheidt, K.A., Nguyen, S.T., and Hupp, J.T. (2009). Metal-organic framework materials as catalysts. Chem. Soc. Rev. *38*, 1450.

22. Cousin Saint Remi, J., Rémy, T., Van Hunskerken, V., van de Perre, S., Duerinck, T., Maes, M., De Vos, D., Gobechiya, E., Kirschhock, C.E.A., Baron, G.V., and Denayer, J.F.M. (2011). Biobutanol separation with the metal–organic framework ZIF-8. ChemSusChem *4*, 1074.

23. Horcajada, P., Gref, R., Baati, T., Allan, P.K., Maurin, G., Couvreur, P., Férey, G., Morris, R.E., and Serre, C. (2012). Metal–organic frameworks in biomedicine. Chem. Rev. *112*, 1232.

24. Bellido, E., Hidalgo, T., Lozano, M.V., Guillevic, M., Simón-Vázquez, R., Santander-Ortega, M.J., González-Fernández, Á., Serre, C., Alonso, M.J., and Horcajada, P. (2015). Heparin-engineered mesoporous iron metal-organic framework nanoparticles: toward stealth drug nanocarriers. Adv. Healthc. Mater. *4*, 1246.

25. Horcajada, P., Chevreau, H., Heurtaux, D., Benyettou, F., Salles, F., Devic, T., Garcia-Marquez, A., Yu, C., Lavrard, H., Dutson, C.L., et al. (2014). Extended and functionalized porous iron(iii) tri- or dicarboxylates with MIL-100/101 topologies. Chem. Commun. *50*, 6872.

26. Huxford, R.C., Rocca, J.D., and Lin, W. (2010). Metal-organic frameworks as potential drug carriers. Curr. Opin. Chem. Biol. *14*, 262.

27. Cunha, D., Ben Yahia, M., Hall, S., Miller, S.R., Chevreau, H., Elkaïm, E., Maurin, G., Horcajada, P., and Serre, C. (2013). Rationale of drug encapsulation and release from biocompatible porous metal–organic frameworks. Chem. Mater. *25*, 2767.

28. Liu, D., Huxford, R.C., and Lin, W. (2011). Phosphorescent nanoscale coordination polymers as contrast agents for optical imaging. Angew. Chem. Int. Ed. *50*, 3696.

29. Rowe, M.D., Thamm, D.H., Kraft, S.L., and Boyes, S.G. (2009). Polymer-modified gadolinium metal-organic framework nanoparticles used as multifunctional nanomedicines for the targeted imaging and treatment of cancer. Biomacromolecules *10*, 983.

30. Zhu, X., Gu, J., Wang, Y., Li, B., Li, Y., Zhao, W., and Shi, J. (2014). Inherent anchorages in UiO-66 nanoparticles for efficient capture of alendronate and its mediated release. Chem. Commun. *50*, 8779.

31. Wang, W., Wang, L., Li, Z., and Xie, Z. (2016). BODIPY-containing nanoscale metal-organic frameworks for photodynamic therapy. Chem. Commun. *52*, 5402.

32. Zhao, H.-X., Zou, Q., Sun, S.-K., Yu, C., Zhang, X., Li, R.-J., and Fu, Y.-Y. (2016). Theranostic metal-organic framework core-shell composites for magnetic resonance imaging and drug delivery. Chem. Sci. *7*, 5294.

33. Miller, S.E., Teplensky, M.H., Moghadam, P.Z., and Fairen-Jimenez, D. (2016). Metal-organic frameworks as biosensors for luminescence-based detection and imaging. Interface Focus *6*, 20160027.

34. Yaghi, O.M., O'Keeffe, M., Ockwig, N.W., Chae, H.K., Eddaoudi, M., and Kim, J. (2003). Reticular synthesis and the design of new materials. Nature *423*, 705.

35. Kitagawa, S., Kitaura, R., and Noro, S.-I. (2004). Functional porous coordination polymers. Angew. Chem. Int. Ed. *43*, 2334.

36. Iversen, T.-G., Skotland, T., and Sandvig, K. (2011). Endocytosis and intracellular transport of nanoparticles: present knowledge and need for future studies. Nano Today *6*, 176.

37. Oh, N., and Park, J.H. (2014). Endocytosis and exocytosis of nanoparticles in mammalian cells. Int. J. Nanomedicine *9*, 51.

38. Orellana-Tavra, C., Mercado, S.A., and Fairen-Jimenez, D. (2016). Endocytosis mechanism of nano metal-organic frameworks for drug delivery. Adv. Healthc. Mater. *5*, 2261.

39. Wang, Z., and Cohen, S.M. (2009). Postsynthetic modification of metal-organic frameworks. Chem. Soc. Rev. *38*, 1315.

40. Kim, M., Cahill, J.F., Fei, H., Prather, K.A., and Cohen, S.M. (2012). Postsynthetic ligand and cation exchange in robust metal–organic frameworks. J. Am. Chem. Soc. *134*, 18082.

41. Marshall, R.J., Richards, T., Hobday, C.L., Murphie, C.F., Wilson, C., Moggach, S.A., Bennett, T.D., and Forgan, R.S. (2016). Postsynthetic bromination of UiO-66 analogues: altering linker flexibility and mechanical compliance. Dalton Trans. *45*, 4132.

42. Ragon, F., Campo, B., Yang, Q., Martineau, C., Wiersum, A.D., Lago, A., Guillerm, V., Hemsley, C., Eubank, J.F., Vishnuvarthan, M., et al. (2015). Acid-functionalized UiO-66(Zr) MOFs and their evolution after intra-framework cross-linking: structural features and sorption properties. J. Mater. Chem. A. *3*, 3294.

43. Wang, S., Morris, W., Liu, Y., McGuirk, C.M., Zhou, Y., Hupp, J.T., Farha, O.K., and Mirkin, C.A. (2015). Surface-specific functionalization of nanoscale metal–organic frameworks. Angew. Chem. Int. Ed. *54*, 14738.

44. Gross, A.F., Sherman, E., Mahoney, S.L., and Vajo, J.J. (2013). Reversible ligand exchange in a metal–organic framework (MOF): toward MOF-based dynamic combinatorial chemical systems. J. Phys. Chem. A. *117*, 3771.

45. Kondo, M., Furukawa, S., Hirai, K., and Kitagawa, S. (2010). Coordinatively immobilized monolayers on porous coordination polymer crystals. Angew. Chem. Int. Ed. *49*, 5327.

46. McGuire, C.V., and Forgan, R.S. (2015). The surface chemistry of metal-organic frameworks. Chem. Commun. *51*, 5199.

47. Zacher, D., Schmid, R., Wöll, C., and Fischer, R.A. (2011). Surface chemistry of metal–organic frameworks at the liquid–solid interface. Angew. Chem. Int. Ed. *50*, 176.

48. Wuttke, S., Braig, S., Prei, Zimpel, A., Sicklinger, J., Bellomo, C., Radler, J.O., Vollmar, A.M., and Bein, T. (2015). MOF nanoparticles coated by lipid bilayers and their uptake by cancer cells. Chem. Commun. *51*, 15752.

49. Férey, G., Serre, C., Mellot-Draznieks, C., Millange, F., Surblé, S., Dutour, J., and Margiolaki, I. (2004). A hybrid solid with giant pores prepared by a combination of targeted chemistry, simulation, and powder diffraction. Angew. Chem. Int. Ed. *43*, 6296.

50. Taylor-Pashow, K.M.L., Rocca, J.D., Xie, Z., Tran, S., and Lin, W. (2009). Post-synthetic modifications of iron-carboxylate nanoscale metal-organic frameworks for imaging and drug delivery. J. Am. Chem. Soc. *131*, 14261.

51. Guo, H., Zhu, Y., Wang, S., Su, S., Zhou, L., and Zhang, H. (2012). Combining coordination modulation with acid–base adjustment for the control over size of metal–organic frameworks. Chem. Mater. *24*, 444.

52. Tsuruoka, T., Furukawa, S., Takashima, Y., Yoshida, K., Isoda, S., and Kitagawa, S. (2009). Nanoporous nanorods fabricated by

coordination modulation and oriented attachment growth. Angew. Chem. Int. Ed. *48*, 4739.

53. Vermoortele, F., Bueken, B., Le Bars, G., Van de Voorde, B., Vandichel, M., Houthoofd, K., Vimont, A., Daturi, M., Waroquier, M., Van Speybroeck, V., et al. (2013). Synthesis modulation as a tool to increase the catalytic activity of metal–organic frameworks: the unique case of UiO-66(Zr). J. Am. Chem. Soc. *135*, 11465.

54. Umemura, A., Diring, S., Furukawa, S., Uehara, H., Tsuruoka, T., and Kitagawa, S. (2011). Morphology design of porous coordination polymer crystals by coordination modulation. J. Am. Chem. Soc. *133*, 15506.

55. Pham, M.-H., Vuong, G.-T., Vu, A.-T., and Do, T.-O. (2011). Novel route to size-controlled Fe–MIL-88B–NH_2 metal–organic framework nanocrystals. Langmuir *27*, 15261.

56. Hermes, S., Witte, T., Hikov, T., Zacher, D., Bahnmüller, S., Langstein, G., Huber, K., and Fischer, R.A. (2007). Trapping metal-organic framework nanocrystals: an in-situ time-resolved light scattering study on the crystal growth of MOF-5 in solution. J. Am. Chem. Soc. *129*, 5324.

57. Park, J., Wang, Z.U., Sun, L.-B., Chen, Y.-P., and Zhou, H.-C. (2012). Introduction of functionalized mesopores to metal–organic frameworks via metal–ligand–fragment coassembly. J. Am. Chem. Soc. *134*, 20110.

58. Zimpel, A., Preiß, T., Röder, R., Engelke, H., Ingrisch, M., Peller, M., Rädler, J.O., Wagner, E., Bein, T., Lächelt, U., and Wuttke, S. (2016). Imparting functionality to MOF nanoparticles by external surface selective covalent attachment of polymers. Chem. Mater. *28*, 3318.

59. Cavka, J.H., Jakobsen, S., Olsbye, U., Guillou, N., Lamberti, C., Bordiga, S., and Lillerud, K.P. (2008). A new zirconium inorganic building brick forming metal organic frameworks with exceptional stability. J. Am. Chem. Soc. *130*, 13850.

60. Orellana-Tavra, C., Baxter, E.F., Tian, T., Bennett, T.D., Slater, N.K.H., Cheetham, A.K., and Fairen-Jimenez, D. (2015). Amorphous metal-organic frameworks for drug delivery. Chem. Commun. *51*, 13878.

61. Liang, W., and D'Alessandro, D.M. (2013). Microwave-assisted solvothermal synthesis of zirconium oxide based metal-organic frameworks. Chem. Commun. *49*, 3706.

62. Katz, M.J., Brown, Z.J., Colon, Y.J., Siu, P.W., Scheidt, K.A., Snurr, R.Q., Hupp, J.T., and Farha, O.K. (2013). A facile synthesis of UiO-66, UiO-67 and their derivatives. Chem. Commun. *49*, 9449.

63. Schaate, A., Roy, P., Godt, A., Lippke, J., Waltz, F., Wiebcke, M., and Behrens, P. (2011). Modulated synthesis of Zr-based metal–organic frameworks: from nano to single crystals. Chem. Eur. J. *17*, 6643.

64. Wu, H., Chua, Y.S., Krungleviciute, V., Tyagi, M., Chen, P., Yildirim, T., and Zhou, W. (2013). Unusual and highly tunable missing-linker defects in zirconium metal–organic framework UiO-66 and their important effects on gas adsorption. J. Am. Chem. Soc. *135*, 10525.

65. Trickett, C.A., Gagnon, K.J., Lee, S., Gándara, F., Bürgi, H.-B., and Yaghi, O.M. (2015). Definitive molecular level characterization of defects in UiO-66 crystals. Angew. Chem. Int. Ed. *54*, 11162.

66. Goto, Y., Sato, H., Shinkai, S., and Sada, K. (2008). "Clickable" metal-organic framework. J. Am. Chem. Soc. *130*, 14354.

67. Shao, C., Wang, X., Zhang, Q., Luo, S., Zhao, J., and Hu, Y. (2011). Acid-base jointly promoted copper(I)-catalyzed azide-alkyne cycloaddition. J. Org. Chem. *76*, 6832.

68. Barrett, E.P., Joyner, L.G., and Halenda, P.P. (1951). The determination of pore volume and area distributions in porous substances. I. Computations from nitrogen isotherms. J. Am. Chem. Soc. *73*, 373.

69. Zahna, G., Schulze, H.A., Lippke, J., König, S., Sazamac, U., Fröba, M., and Behrens, P. (2015). A water-born Zr-based porous coordination polymer: modulated synthesis of Zr-fumarate MOF. Micropor. Mesopor. Mater *203*, 186.

70. Hirschle, P., Preiß, T., Auras, F., Pick, A., Völkner, J., Valdepérez, D., Witte, G., Parak, W.J., Rädler, J.O., and Wuttke, S. (2016). Exploration of MOF nanoparticle sizes using various physical characterization methods – is what you measure what you get? CrystEngComm *18*, 4359.

71. Perry, J.L., Reuter, K.G., Kai, M.P., Herlihy, K.P., Jones, S.W., Luft, J.C., Napier, M., Bear, J.E., and DeSimone, J.M. (2012). PEGylated PRINT nanoparticles: the impact of PEG density on protein binding, macrophage association, biodistribution, and pharmacokinetics. Nano Lett. *12*, 5304.

72. Gref, R., Domb, A., Quellec, P., Blunk, T., Müller, R.H., Verbavatz, J.M., and Langer, R. (2012). The controlled intravenous delivery of drugs using PEG-coated sterically stabilized nanospheres. Adv. Drug Deliv. Rev. *64*, 316.

73. Sebby, K.B., and Mansfield, E. (2015). Determination of the surface density of polyethylene glycol on gold nanoparticles by use of microscale thermogravimetric analysis. Anal. Bioanal. Chem. *407*, 2913.

74. Rouquerol, F., Rouquerol, J., and Sing, K. (1999). Adsorption by Powders and Porous Solids (Academic Press), p. p 219.

75. deKrafft, K.E., Boyle, W.S., Burk, L.M., Zhou, O.Z., and Lin, W. (2012). Zr- and Hf-based nanoscale metal–organic frameworks as contrast agents for computed tomography. J. Mater. Chem. *22*, 18139.

76. Sun, C.-Y., Qin, C., Wang, X.-L., Yang, G.-S., Shao, K.-Z., Lan, Y.-Q., Su, Z.-M., Huang, P., Wang, C.-G., and Wang, E.-B. (2012). Zeolitic imidazolate framework-8 as efficient pH-sensitive drug delivery vehicle. Dalton Trans. *41*, 6906.

77. Bellido, E., Guillevic, M., Hidalgo, T., Santander-Ortega, M.J., Serre, C., and Horcajada, P. (2014). Understanding the colloidal stability of the mesoporous MIL-100(Fe) nanoparticles in physiological media. Langmuir *30*, 5911.

78. Li, Z., and Zeng, H.C. (2014). Armored MOFs: enforcing soft microporous MOF nanocrystals with hard mesoporous silica. J. Am. Chem. Soc. *136*, 5631.

79. Huang, X., and Brazel, C.S. (2001). On the importance and mechanisms of burst release in matrix-controlled drug delivery systems. J. Control Release *73*, 121.

80. Javadi, M., Pitt, W.G., Tracy, C.M., Barrow, J.R., Willardson, B.M., Hartley, J.M., and Tsosie, N.H. (2013). Ultrasonic gene and drug delivery using eLiposomes. J. Control Release *167*, 92.

81. Deutsch, C., Taylor, J.S., and Wilson, D.F. (1982). Regulation of intracellular pH by human peripheral blood lymphocytes as measured by ^{19}F NMR. Proc. Natl. Acad. Sci. USA *79*, 7944.

82. Orellana-Tavra, C., Marshall, R.J., Baxter, E.F., Abánades Lázaro, I., Tao, A., Cheetham, A.K., Forgan, R.S., and Fairen-Jimenez, D. (2016). Drug delivery and controlled release from biocompatible metal–organic frameworks using mechanical amorphization. J. Mater. Chem. B *4*, 7697.

83. Mellman, I. (1996). Endocytosis and molecular sorting. Annu. Rev. Cell Dev. Biol. *12*, 575.

84. Rejman, J., Oberle, V., Zuhorn, I.S., and Hoekstra, D. (2004). Size-dependent internalization of particles via the pathways of clathrin- and caveolae-mediated endocytosis. Biochem. J. *377*, 159.

85. McMahon, H.T., and Boucrot, E. (2011). Molecular mechanism and physiological functions of clathrin-mediated endocytosis. Nat. Rev. Mol. Cell Biol. *12*, 517.

86. Mayor, S., and Pagano, R.E. (2007). Pathways of clathrin-independent endocytosis. Nat. Rev. Mol. Cell Biol. *8*, 603.

87. Gonzalez-Gaitan, M., and Stenmark, H. (2003). Endocytosis and signaling: a relationship under development. Cell *115*, 513.

88. Shin, J., and Abraham, S.N. (2001). Co-option of endocytic functions of cellular caveolae by pathogens. Immunology *102*, 2.

89. Tuthill, T.J., Groppelli, E., Hogle, J.M., and Rowlands, D.J. (2010). Picornaviruses. Curr. Top. Microbiol. Immunol. *343*, 43.

90. Vercauteren, D., Vandenbroucke, R.E., Jones, A.T., Rejman, J., Demeester, J., De Smedt, S.C., Sanders, N.N., and Braeckmans, K. (2010). The use of inhibitors to study endocytic pathways of gene carriers: optimization and pitfalls. Mol. Ther. *18*, 561.

91. Chen, Y., Wang, S., Lu, X., Zhang, H., Fu, Y., and Luo, Y. (2011). Cholesterol sequestration by nystatin enhances the uptake and activity of endostatin in endothelium via regulating distinct endocytic pathways. Blood *117*, 6392.

92. Hufnagel, H., Hakim, P., Lima, A., and Hollfelder, F. (2009). Fluid phase endocytosis contributes to transfection of DNA by PEI-25. Mol. Ther. *17*, 1411.

93. Sarkar, K., Kruhlak, M.J., Erlandsen, S.L., and Shaw, S. (2005). Selective inhibition by

rottlerin of macropinocytosis in monocyte-derived dendritic cells. Immunology *116*, 513.

94. Park, J., Jiang, Q., Feng, D., Mao, L., and Zhou, H.–C. (2016). Size-controlled synthesis of porphyrinic metal-organic framework and functionalization for targeted photodynamic therapy. J. Am. Chem. Soc. *138*, 3518.

95. Lim, J.P., and Gleeson, P.A. (2011). Macropinocytosis: an endocytic pathway for internalising large gulps. Immunol. Cell Biol. *89*, 836.

96. Michelakis, E.D., Webster, L., and Mackey, J.R. (2008). Dichloroacetate (DCA) as a potential metabolic-targeting therapy for cancer. Br. J. Cancer *99*, 989.

97. Bonnet, S., Archer, S.L., Allalunis-Turner, J., Haromy, A., Beaulieu, C., Thompson, R., Lee, C.T., Lopaschuk, G.D., Puttagunta, L., Bonnet, S., et al. (2007). A mitochondria-K^+ channel axis is suppressed in cancer and its normalization promotes apoptosis and inhibits cancer growth. Cancer Cell *11*, 37.

98. Badr, M.M., Qinna, N.A., Qadan, F., and Matalka, K.Z. (2014). Dichloroacetate modulates cytokines toward T helper 1 function via induction of the interleukin-12–interferon-γ pathway. Onco Targets Ther. *7*, 193.

99. Stacpoole, P.W., Nagaraja, N.V., and Hutson, A.D. (2003). Efficacy of dichloroacetate as a lactate-lowering drug. J. Clin. Pharmacol. *43*, 683.

100. Wang, W., Wang, L., Li, Y., Liu, S., Xie, Z., and Jing, X. (2016). Nanoscale polymer metal-organic framework hybrids for effective photothermal therapy of colon cancers. Adv. Mater. *28*, 9320.

101. Calik, M., Sick, T., Dogru, M., Döblinger, M., Datz, S., Budde, H., Hartschuh, A., Auras, F., and Bein, T. (2016). From highly crystalline to outer surface-functionalized covalent organic frameworks—a modulation approach. J. Am. Chem. Soc. *138*, 1234.

Chem, Volume *2*

Supplemental Information

Selective Surface PEGylation of UiO-66 Nanoparticles for Enhanced Stability, Cell Uptake, and pH-Responsive Drug Delivery

Isabel Abánades Lázaro, Salame Haddad, Sabrina Sacca, Claudia Orellana-Tavra, David Fairen-Jimenez, and Ross S. Forgan

Table of Contents

All experimental data associated with this manuscript are available for download at:

http://dx.doi.org/10.5525/gla.researchdata.389

S1. General Experimental Remarks

Powder X-ray Diffraction (PXRD): PXRD measurements were carried out at 298 K using a PANalytical X'Pert PRO diffractometer (λ (CuKα) = 1.4505 Å) on a mounted bracket sample stage. Data were collected over the range 5–45 °. (University of Glasgow)

Thermogravimetric Analysis (TGA): Measurements were carried out using a TA Instruments Q500 Thermogravimetric Analyser. Measurements were collected from room temperature to 800 °C with a heating rate of 10 °C / min under an air atmosphere. (University of Glasgow)

Nuclear Magnetic Resonance Spectroscopy (NMR): NMR spectra were recorded on either a Bruker AVIII 400 MHz spectrometer or a Bruker AVI 500 MHz spectrometer and referenced to residual solvent peaks. (University of Glasgow)

Gas Uptake: N_2 adsorption isotherms were carried out at 77 K on a Quantachrome Autosorb iQ gas sorption analyser. Samples were degassed under vacuum at 120 °C for 20 hours using the internal turbo pump. BET surface areas were calculated from the isotherms using the Micropore BET Assistant in the Quantachrome ASiQwin operating software. (University of Glasgow)

Pore-Size Distribution: Pore size distributions were calculated using the N_2 at 77 K on carbon (slit pore, QSDFT, equilibrium model) calculation model within the Quantachrome ASiQwin operating software. (University of Glasgow)

UV-Vis Spectroscopy: UV-vis spectra were recorded using a Shimadzu UV-1800; analysis was carried out using the software UVProve. (University of Glasgow)

ESIMS: Electrospray Ionisation Mass Spectrometry was carried out on solution samples injected into a Bruker MicroTOFq spectrometer. (University of Glasgow).

Scanning Electron Microscopy (SEM): The powder samples were coated with Pd for 150 seconds using Polaron SC7640 sputter coater and imaged using a Carl Zeiss Sigma Variable Pressure Analytical SEM with Oxford Microanalysis. Particle size distribution was analysed manually using ImageJ software. (University of Glasgow)

IR: Infra-red spectra of solids were collected using a Shimadzu Fourier Transform Infrared

Spectrometer, FTIR-8400S, fitted with a Diamond ATR unit. (University of Glasgow)

Flow Cytometry: Measurements were carried out using Cytek DxP8 analyser cytometer; BLU mode (laser)-FLU1 (fluorenscence detector). The analysis was done using FlowJo and Prism softwares. (University of Cambridge)

Confocal Microscopy: Measurements were carried out using Leica TCS SP5 confocal microscope. The microscope was equipped with 405 diode, argon and HeNe lasers. Leica LAS AF software was used to analyse the images. (University of Cambridge)

Dynamic Light Scattering: Colloidal analysis was performed by Dynamic Light Scattering (DLS) with a Zetasizer Nano ZS potential analyser equipped with Non-Invasive Backscatter optics (NIBS) and a 50 mW laser at 633 nm. (University of Glasgow)

S2. Materials and Synthesis

All reagents unless otherwise stated were obtained from commercial sources and were used without further purification. The modulators L1[S1] and[S2] L2 were synthesised by literature procedures, and the synthesis of UiO-66 – $[Zr_6O_4(OH)_4(C_8H_4O_4)_x]_n$ – was adapted from a literature procedure.[S3] The propargyl modified monomethyl poly(ethylene glycol) samples were synthesised according to a literature procedure.[S4]

p-Azidomethyl benzoic acid (L1)

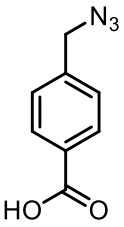

The commercially available 4-(bromomethyl)benzoic acid (5 g, 23.27 mmol, 1.0 eq) was dissolved in *N*,*N*-dimethylformamide (DMF, 150 mL) in a round 250 mL bottom flask. Sodium azide (3.8 g, 58.18 mmol, 2.5 eq) was added dropwise. The reaction mixture was heated at 50 °C for 24 hours. The solvent was evaporated under vacuum. Following the literature procedure, *p*-azidomethyl benzoic acid (3.91 g, 22.1 mmol, 95%) was obtained pure as a white solid.

^{1}H NMR (500 MHz, $CDCl_3$) δ 4.48 (s, 2 H), 7.46 (d, *J* = 8.4 Hz, 2H), 8.16 (d, *J* = 8.3 Hz, 2H); **^{13}CNMR** (126 MHz, $CDCl_3$) δ 53.41, 128.7, 130.62, 130.91, 141.04, 167.51.

The azide band (2130 cm^{-1}) was identified by IR, and compared with the staring material.

ESI-MS: calculated for $C_8H_6N_3O_2$ *m/z* = 176.0466; found *m/z* = 176.0455.

p-Propargyloxy benzoic acid (L2)

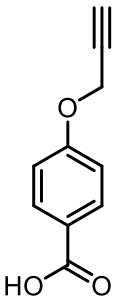

To a solution of methyl 4-hydroxybenzoate (5 g, 33 mmol, 1.0 eq) in acetonitrile (40 mL), K_2CO_3 (6.64 g, 49.5 mmol, 1.5 eq) was added. The mixture was heated to 50 °C for 30 min followed by dropwise addition of propargyl bromide (80% in toluene, 4.9 g, 3.53 mL, 33 mmol, 1 eq). The mixture was allowed to react at the same temperature during 16 hours. Solvent was evaporated and the remaining liquid was quenched with water and extracted with chloroform (4 x 15 mL). The organic layers were combined and washed with water (2 x 10 mL) and brine (2 x 10 mL). Pure methyl *p*-propargyloxybenzoate was obtained as a white solid (8.11 g, 32 mmol, 97%).

^{1}H NMR (500 MHz, $CDCl_3$) δ: 2.54 (t, *J* = 2.5 Hz, 1H), 3.88 (s, 3H), 4.74 (d, *J* = 2.5 Hz, 2H), 6.99 (d, *J* = 8.5 Hz, 2H), 8.00 (d, *J* = 9.0 Hz, 2H); **^{13}C NMR** (126 MHz, $CDCl_3$) δ: 51.86, 55.78, 76.05, 77.79, 114.51, 123.42, 131.50, 161.11, and 166.64.

Methyl *p*-propargyloxybenzoate (8 g, 32 mmol) was dissolved in a mixture of THF (45 mL) and MeOH (22.5 mL), an aqueous solution of NaOH 40% weight (25 mL) was added and the reaction mixture allowed to reflux for two hours. After cooling down, the organic solvents

were distilled under vacuum yielding a clear solution, which was acidified with 6 M aqueous HCl. A white precipitate separated, was filtered and washed with abundant water, yielding after drying under vacuum pure *p*-propargyloxybenzoic acid (6.43 g, 27 mmol, 87.6%).
^{1}H NMR (500 MHz, $CDCl_3$) δ: 3.57 (t, *J* = 2.4 Hz, 1H), 4.86 (d, *J* = 2.4 Hz, 2H), 7.04 (d, *J* = 9.0 Hz, 2H), 7.88 (d, *J* = 9.0 Hz, 2H), 12.41 (s, 1H); **^{13}C NMR** (126 MHz, $CDCl_3$) δ: 39.91, 56.05, 79.02, 79.14, 115.04, 124.11, 131.67, and 161.13.
ESI-MS: calculated for $C_{10}H_7O_3$ *m/z* = 175.0401; found *m/z* = 175.0399.

UiO-66 Synthesis

UiO-66 was synthesised by adaptation of a literature procedure to include different modulators as follows. For all samples, after cooling the reaction mixture, particles were collected by centrifugation (4500 rpm, 15 minutes), and washed (sonication centrifugation cycles) with fresh DMF (x1) and MeOH (x3). The NMOFs were dried for at least 24 hours under vacuum before analysis.

UiO-66 (Unmodulated)

1,4-Benzenedicarboxylic acid (bdc) (448 mg, 2.7 mmol) was dissolved in 30 mL of DMF. In a separate vial, the metal precursor, zirconium chloride (629 mg, 2.7 mmol) was dissolved in 30 mL of DMF. Both solutions were sonicated until complete dissolution and mixed together in a 100 mL jar. The solution was heated to 120 ºC for 24 hours yielding UiO-66 nanoparticles.

UiO-66-AcOH (Modulated with acetic acid)

UiO-66 particles were modulated using the same procedure. Acetic acid (4.2 mL, 7% volume) was added after mixing both precursors solutions. The sample is named UiO-66-AcOH.

UiO-66-L1 and UiO-66-L2 (Modulated with L1 or L2)

1,4-Benzenedicarboxylic acid (448 mg, 2.7 mmol) plus one, three or five equivalents of modulator (L1 or L2), compared to metal precursor, were dissolved in 30 mL of DMF. In a separate vial, the metal precursor, zirconium chloride (629 mg, 2.7 mmol) was dissolved in 30 mL of DMF. Both solutions were sonicated until complete dissolution and mixed together. Subsequently, acetic acid (4.2 mL, 7% volume) was added. The solution was heated to 120 ºC for 24 hours yielding UiO-66 nanoparticles.

1-Azidodecane

1-Bromodecane (4 g, 0.018 mol, 1 eq) was dissolved in DMF (50 mL). Then, sodium azide (2.39 g, 0.036 mol, 2 eq) was added dropwise, and the mixture was allowed to react at 50 ºC overnight. After the solvent was evaporated, the remaining mixture was poured into water (100 mL) and extracted with DCM (3 x 25 mL). The organic phase was further washed with water (2 x 15 mL). The product was obtained pure as a slightly yellow oil (3.2 g, 94%), whose spectroscopic data matched that found in the literature.[S5]

^{1}H NMR (400 MHz, DMSO) δ 0.86 (t, *J* = 6.9 Hz, 3H), 1.36 – 1.19 (m, 14H), 1.58 – 1.45 (m, 2H), 3.31 (t, *J* = 6.9 Hz, 2H); **^{13}C NMR** (101 MHz, DMSO) δ 14.38, 22.55, 26.60, 28.70, 28.99, 29.13, 29.37, 29.38, 31.64, 51.10.

PEG550-propargyl

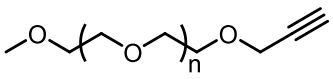

In a typical PEG550-propargyl synthesis (*n* = 11), 1 eq (2 g, 3.64 mmol) of PEG550 methyl ether is dissolved in 50 mL anhydrous THF under nitrogen. After that, 1.5 eq (236 mg, 5.46 mmol) of 60% NaH in mineral oil, and 1.5 eq (0.6 mL, 3.40 mmol) of propargyl bromide, are added. The solution is stirred overnight at room temperature. The resulting mixture is then filtrated and evaporated under vacuum. A clear, brown oil is obtained (1.225 g, 2.125 mmol, 59%).[4]

^{1}H NMR: (500 MHz, DMSO) δ 3.25 (s, 3H), 3.47 – 3.40 (m, 4H), 3.54 – 3.48 (m, 44H), 4.15 (d, *J* = 2.4 Hz, 2H); **^{13}C NMR:** (101 MHz, DMSO) δ 57.95, 58.51, 68.98, 70.25 (high intensity, polymeric chain), 71.75, 77.51, 80.79.

ESIMS: calculated for $C_4H_5O(C_2H_4O)_nC_2H_5O$, *M*+Na+ (n = 6) *m/z* = 401.2151; found *m/z* = 401.2160, *(found from n=6 to n=17).*

PEG2000-propargyl

In a typical PEG2000-propargyl synthesis (*n* = 44), 1 eq (2 g, 1 mmol) of PEG2000 methyl ether is dissolved in 100 mL anhydrous tetrahydrofuran (THF) under nitrogen. After that, 1.5 eq (65 mg, 1.5 mmol) of 60% NaH in mineral oil, and 1.5 eq (0.6 mL, 3.40 mmol) of propargyl bromide, are added. The solution is stirred overnight at room temperature. The resulting mixture is then filtered and evaporated under vacuum. A white, hard powder is obtained (993 mg, 0.51 mmol, 51%).

^{1}H NMR (500 MHz, DMSO) δ 3.25 (s, 3H), 3.46 – 3.41 (m, 4H), 3.52 (s, 88H), 4.15 (d, *J* = 2.4 Hz, 2H); **^{13}C NMR:** (101 MHz, DMSO) δ 57.95, 58.51, 68.98, 69.97, 70.05, 70.25 (high intensity, polymeric chain), 70.65, 71.75, 77.52, 80.79.

No ionisation was observed in ESIMS, IR showed a stretch at $\bar{\nu}$= 2883 cm^{-1}, which is representative of the alkyne functionality.

L1-dodecyne

1-Dodecyne (1.98 mmol, 327 mg, 1.2 equivalents) was dissolved in DCM (50 mL), DiPEA (4 mol%, 138 µl), AcOH (4 mol %, 45 µl) and CuI (2 mol %, 7.5 mg) were added, and the mixture stirred 15 minutes under nitrogen. Then, *p*-azidomethylbenzoic acid (L1) (1.65 mmol, 291 mg, 1 equivalent) was added to the reaction mixture, which was allowed to react overnight at room temperature under nitrogen atmosphere. Then, the reaction solvent was washed with water (3 x 15 mL) with an aqueous EDTA solution (2 x 15 mL) and with water (2 x 15 mL). Pure product was obtained as a white powder after evaporation of the organic solvent.

^{1}H NMR (400 MHz, DMSO) δ 0.85 (t, *J* = 6.8 Hz, 3H), 1.34 – 1.12 (m, 13H), 1.65 – 1.46 (m, 2H), 2.60 (t, *J* = 7.5 Hz, 2H), 5.64 (s, 2H), 7.35 (d, *J* = 8.2 Hz, 2H), 8.11 – 7.79 (m, 3H), 13.02 (s, 1H); **^{13}C NMR** (101 MHz, DMSO) δ 14.40, 22.55, 25.43, 28.99, 29.15, 29.20, 29.32, 29.35, 29.42, 31.74, 31.78, 52.65, 122.75, 128.26, 130.12, 130.18, 130.85, 141.57, 147.75.

L2-decane

1-Azidodecane (2.5 mmol, 461 mg, 1.2 equivalents) was dissolved in DCM (50 mL), DiPEA (4 mol %, 146 µl), AcOH (4 mol %, 48 µl) and CuI (2 mol, 8.0 mg) were added, and the mixture stirred 15 minutes under nitrogen. Then, *p*-propargyloxybenzoic acid (L2) (2.1 mmol, 500 mg, 1 equivalent) was added to the reaction mixture, which was allowed to react overnight at room temperature under nitrogen atmosphere. Then, the reaction solvent was washed with water (3 x 15 mL) with an aqueous EDTA solution (2 x 15 mL) and with water (2 x 15 mL). Pure product was obtained as a white–yellowish powder after evaporation of the organic solvent. **^{1}H NMR** (400 MHz, DMSO) δ 12.63 (s, 1H), 8.25 (s, 1H), 7.89 (d, *J* = 8.7 Hz, 2H), 7.12 (d, *J* = 8.7 Hz, 2H), 5.22 (s, 2H), 4.36 (t, *J* = 7.1 Hz, 2H), 1.92 – 1.65 (m, 2H), 1.23 (s, 12H), 0.85 (t, *J* = 6.9 Hz, 3H); **^{13}C NMR** (101 MHz, DMSO) δ 204.59, 194.88, 162.04, 161.77, 131.71, 114.93, 49.85, 31.78, 31.73, 29.35, 29.32, 29.30, 29.10, 28.97, 28.82, 28.79, 28.69, 26.26, 22.57, 14.41.

S3. Characterization of NMOFs

Analysis of the UiO-66 samples by PXRD confirmed their crystallinity (Figure S1). Unmodulated samples showed a broad PXRD pattern, indicating a very small particle size, while UiO-66-AcOH showed a better defined PXRD pattern. Inclusion of L1 or L2 did not affect crystallinity and produced phase pure samples.

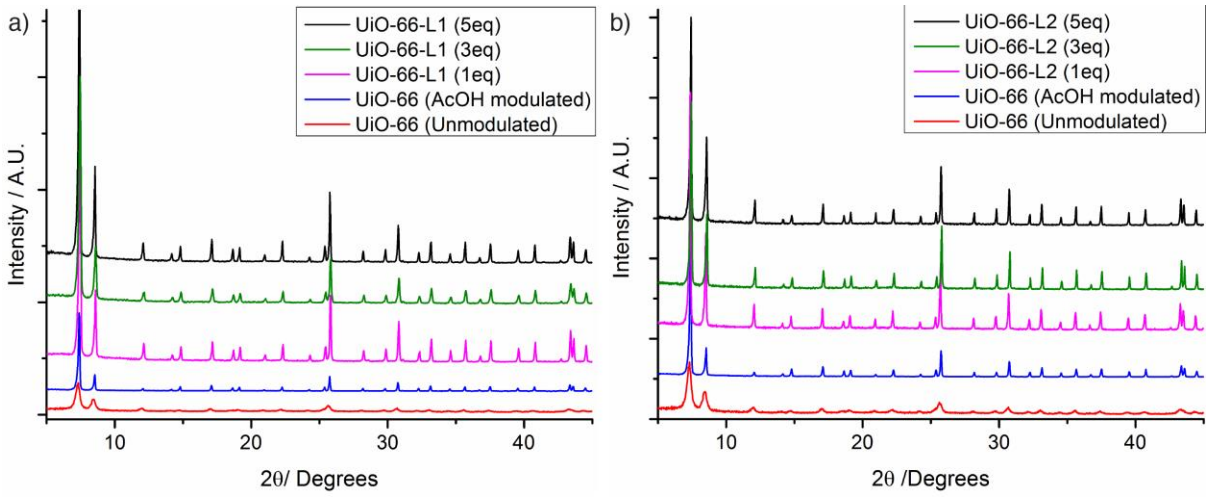

Figure S1. Stacked PXRD patterns of UiO-66 modulated with a) L1 and b) L2.

The modulator (L1 or L2) content in the UiO-66 samples was calculated using ^{1}H NMR spectroscopy of samples digested in D_2SO_4 / DMSO-d_6. By comparing intensity of one of the aromatic signals of the modulator (d, 2H) to the resonance of the aromatic protons of the bdc linker (s, 4H), it is possible to determine modulator content using the formula:

$$L\ mol\%\ compared\ to\ linker = \frac{\text{Intensity (L aromatic signal)}}{\text{Intensity (L aromatic signal)} + (\text{bdc aromatic signal}/2)} * 100$$

Typical ^{1}H NMR spectra are shown in Figure S2, which corresponds to UiO-66-L1 (5 eq), and Figure S3, which corresponds to UiO-66-L2 (3 eq). The integral ratios confirm that L1 is present in 13.3% molar ratio when compared to the linker, bdc, and L2 is present in 6.8% molar ratio. In this way, the increasing content of both L1 in UiO-66-L1 and L2 in UiO-66-L2 could be determined (Table S1).

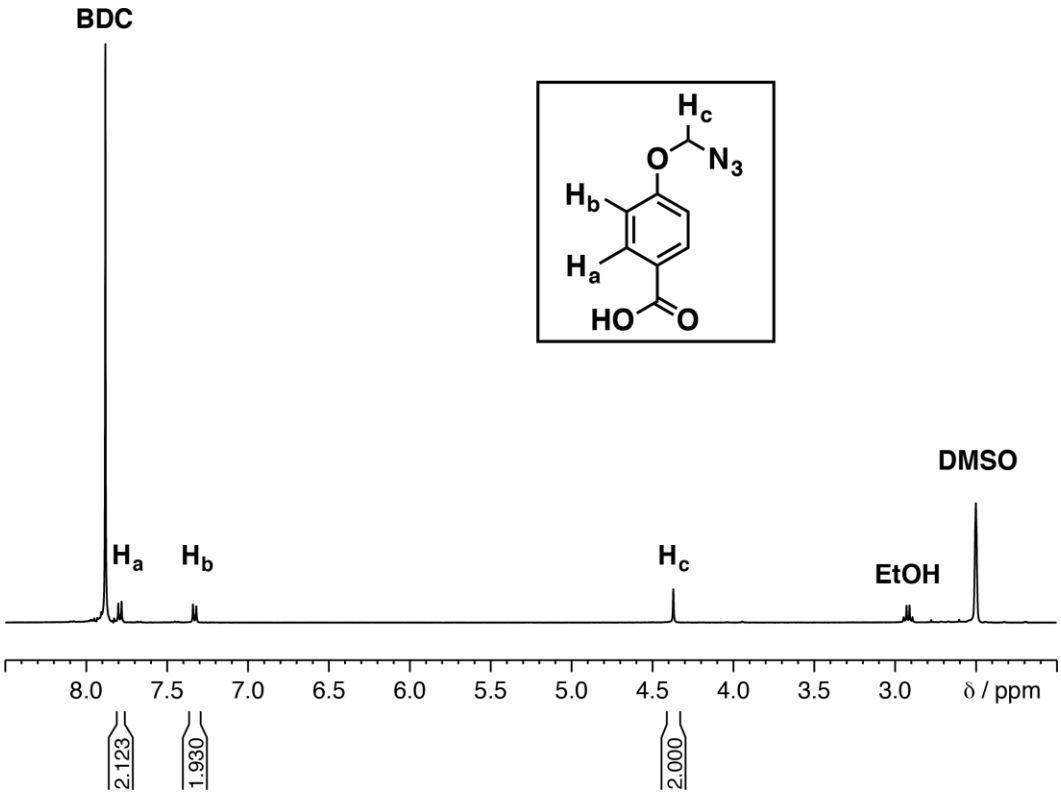

Figure S2. ^{1}H NMR spectrum (D_2SO_4 / DMSO-d_6, 293 K) of UiO-66-L1 (5 eq), showing the presence of the modulator L1.

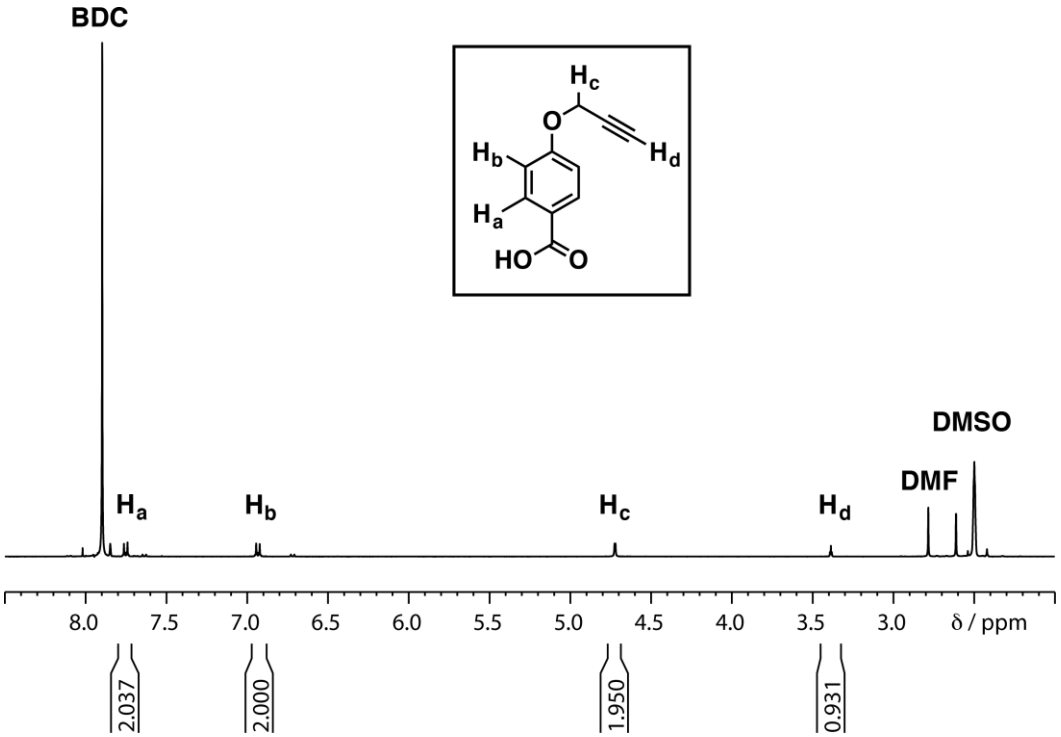

Figure S3. ^{1}H NMR spectrum (D_2SO_4 / DMSO-d_6, 293 K) of UiO-66-L2 (3 eq), showing the presence of the modulator L2.

Table S1. Modulator content in UiO-66 samples determined by ^{1}H NMR spectra.

Modulator	L1 (1 eq)	L1 (3 eq)	L1 (5 eq)	L2 (1 eq)	L2 (3 eq)	L2 (5 eq)
Mol % versus bdc	5.6%	8.3%	13.3%	1.2%	6.8%	17.1%

FTIR spectra of the samples also showed an increase in signals associated with the functional groups of the modulators (azide band for L1, alkyne signals for L2) as more equivalents were added to the synthetic mixture (Figure S4).

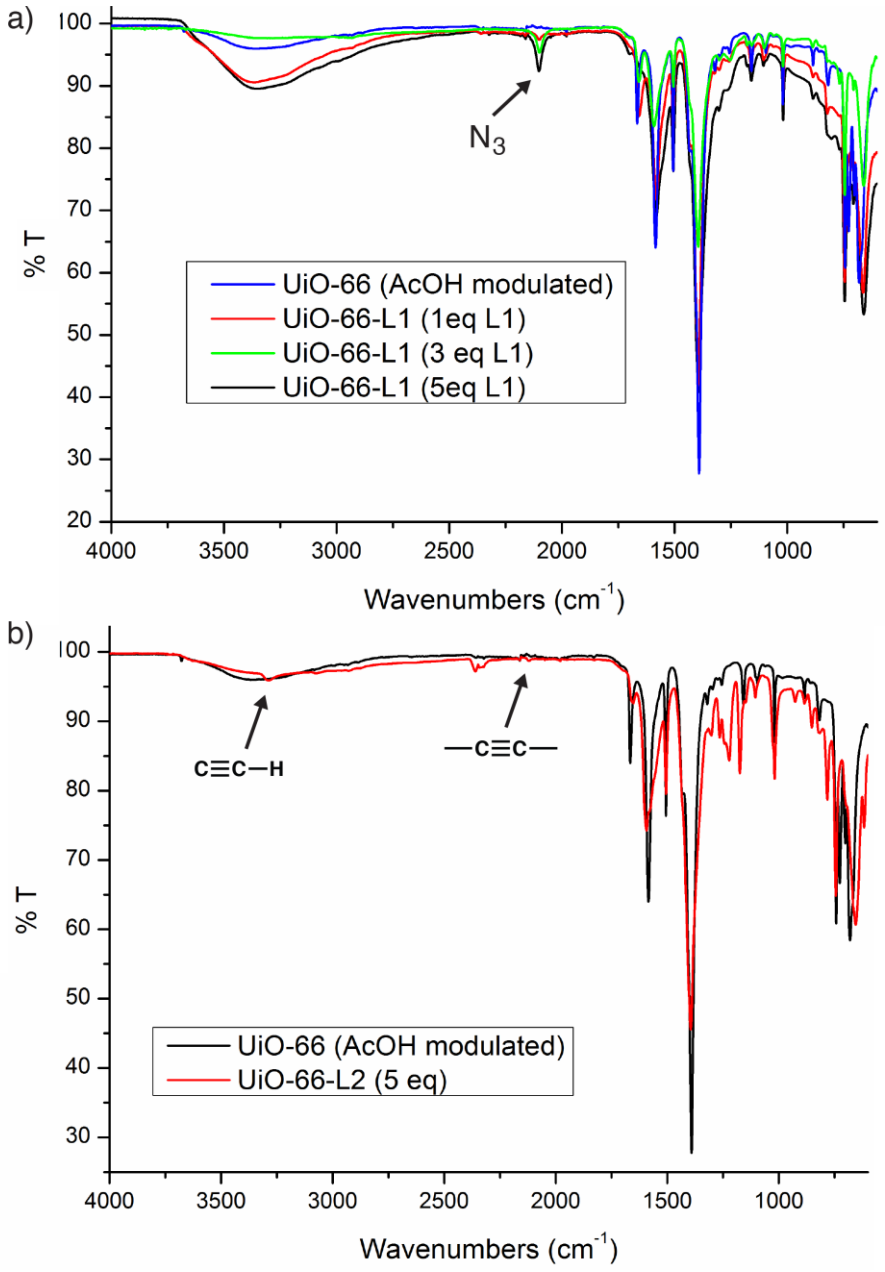

Figure S4. FTIR spectra of modulated UiO-66 samples showing the presence of functional groups of a) L1 and b) L2 in the synthesised MOF.

The effect of modulator incorporation on particle size was examined by SEM imaging. The samples were prepared as low concentration dispersions of nanoparticles in MeOH, which were allowed to dry in the oven at 60 ºC for 5 minutes. For UiO-66-AcOH (Figure S5), particles were roughly spherical aggregates of very small crystals, with a diameter of around 200 nm.

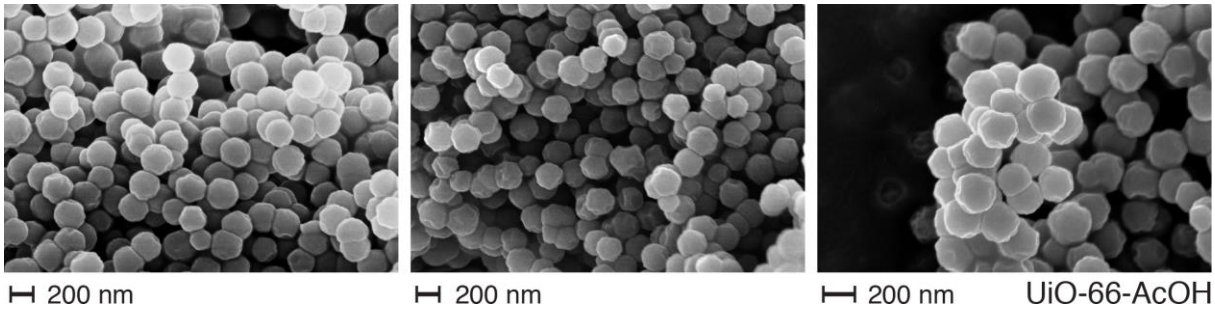

Figure S5. SEM images of UiO-66-AcOH.

For UiO-66-L1 samples, the morphology is noticeably different, being roughly octahedral crystallites of 100-200 nm in size regardless of the number of equivalents of L1 included in the synthetic mixture (Figure S6).

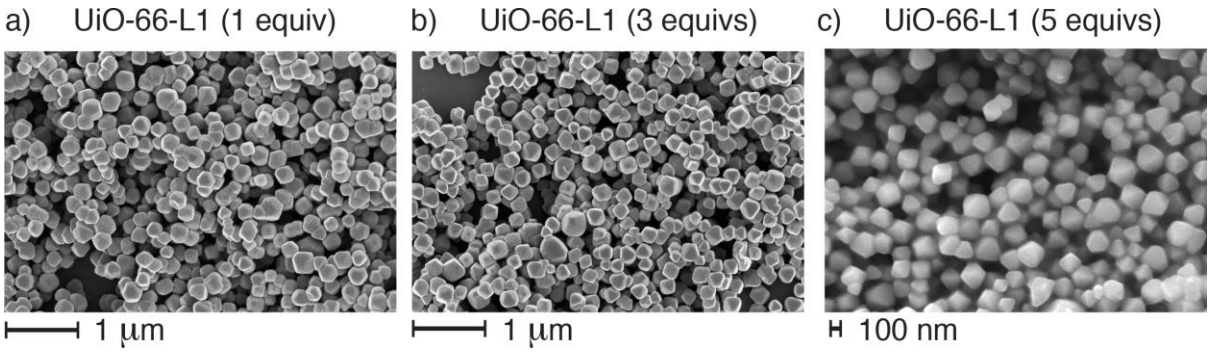

Figure S6. SEM images of a) UiO-66-L1 (1 equiv), b) UiO-66-L1 (3 equiv), and c) UiO-66-L1 (5 equiv).

In contrast, samples of UiO-66-L2 became larger and more polydisperse as more equivalents of L2 were included in the synthetic mixture (Figure S7), reaching sizes of ~600 nm for UiO-66-L2 (5 equiv). UiO-66-L1 (1 equiv) has a reasonable particle size range of around 200-300 nm, but as ^{1}H NMR spectroscopic analysis showed very little incorporation of L2, UiO-66-L2 (5 equiv) was used for proof-of-concept surface modification along with UiO-66-L1 (5 equiv).

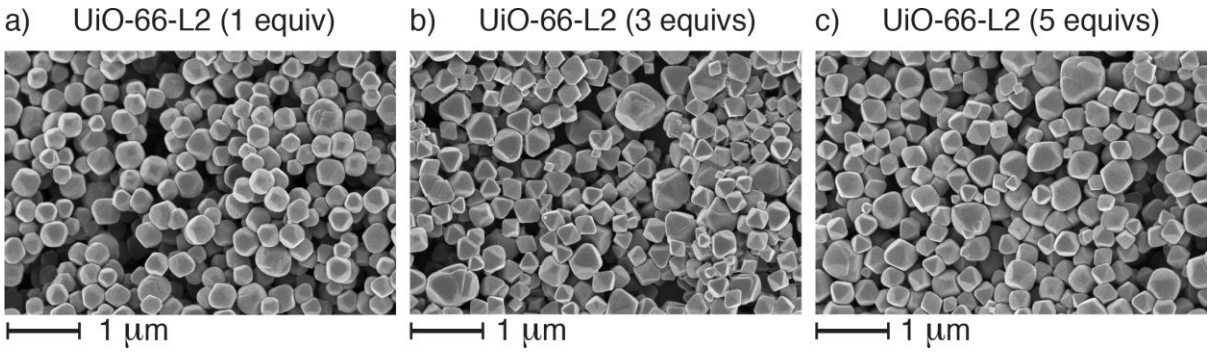

Figure S7. SEM images of a) UiO-66-L2 (1 equiv), b) UiO-66-L2 (3 equiv), and c) UiO-66-L2 (5 equiv).

The quantities of organic components (either bdc or the modulator) present in UiO-66-L1 and UiO-66-L2 (all subsequent samples synthesised with 5 equivalents of modulator) were calculated by TGA measurements (Figure S8) and used for further degradation studies.

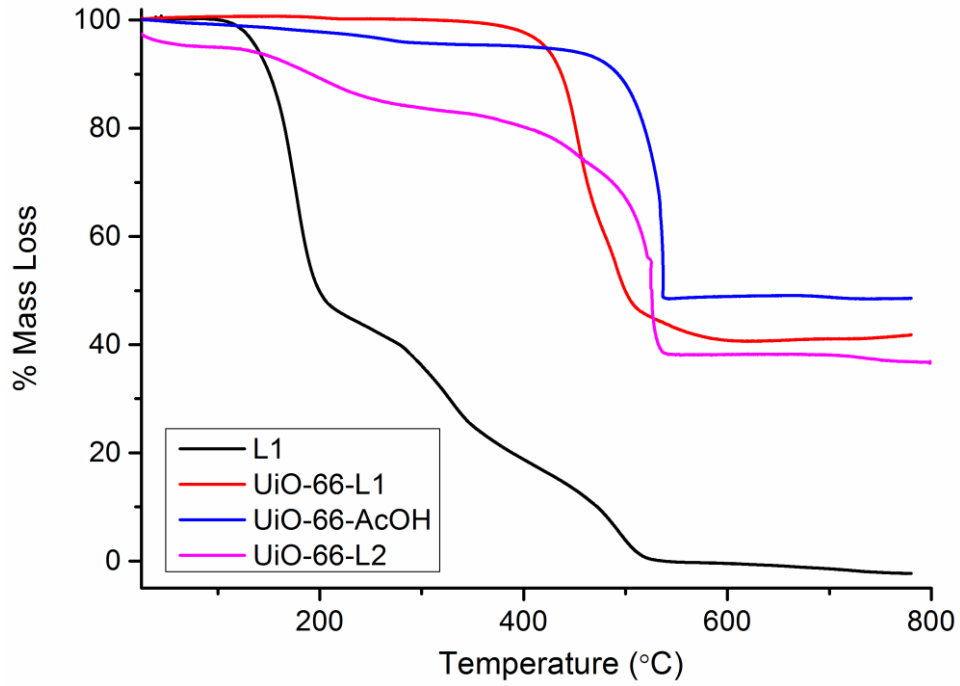

Figure S8. TGA traces (recorded in air) of UiO-66-L1 and UiO-66-L2, compared to L1 and UiO-66-AcOH.

It has been previously reported that when UiO-66 ($Zr_6O_4(OH)_4L_6$ theoretical structure) is thermally degraded in air, the first mass loss step at 200-300 ºC corresponds to the zirconium clusters losing two molecules of water, adopting the $Zr_6O_6L_6$ molecular formula, then, the ligand decomposition takes place near 500 ºC, leaving the residue ZrO_2. Therefore,

by comparing experimental mass loss of the last decomposition step with the weight percent of the linker in the $[Zr_6O_4(OH)_4L_x]_n$ structure for different values of x, the number of ligands in the structure can be estimated (Table S2).[S6]

Table S2. Theoretical compositions of different defective UiO-66 samples.

$$Linker\ wt\% = \frac{\mathrm{xL}}{\mathrm{Zr6O4(OH)4Lx}} * 100$$

Number of linkers in $Zr_6O_4(OH)_4L_x$	Linker wt%
X=6	59.2 wt%
X=5	54.5 wt%
X=4	49.1 wt%
X=3	42.0 wt%

In Figure S7 we can observe that the last decomposition step of UiO-66-AcOH corresponds to 46.8 wt% of the sample, which matches a material with 2.5 ligands missing, leading the approximate composition $[Zr_6O_4(OH)_4L_{3.5}]_n$, with either acetates, chlorides or solvents at defect sites.

When L1 is introduced to the synthetic procedure, the material $[Zr_6O_4(OH)_4L_x(L1)_y]_n$ shows a similar decomposition profile to UiO-66-AcOH, indicating that L1 degrades together with the linker (bdc) but at a lower temperature, suggesting L1 is incorporated at the surfaces or the particles and at defects. As L1 has a similar molecular weight to the bdc linker, we have estimated the total organic content (bdc and L1) present in the sample using the former theoretical calculations. In UiO-66-L1 the last decomposition step corresponds to 59.1% of the total weight of sample, suggesting a full complement of six linkers/modulators in the structure. Therefore, the UiO-66-L1 composition is expected to be close to $[Zr_6O_4(OH)_4L_{6-x}L1_x]_n$. UiO-66-L2 shows a more complex degradation profile, in which degradation of the last ligand step corresponds to 46.2 wt%. As its bioapplications, due to particle size, were not further studied (see later), no in depth analysis of its thermal degradation was performed.

The porosities of the samples were measured by N_2 adsorption isotherms at 77 K, and the adsorption isotherms (Figure S9a) yielded the following information:

UiO-66-AcOH: S_{BET}=1232 m^2g^{-1}; pore volume= 0.652 ccg^{-1}.
UiO-66-L1: S_{BET}=1565 m^2g^{-1}; pore volume= 0.762 ccg^{-1}.
UiO-66-L2: S_{BET}=1420 m^2g^{-1}; pore volume = 0.702 ccg^{-1}.

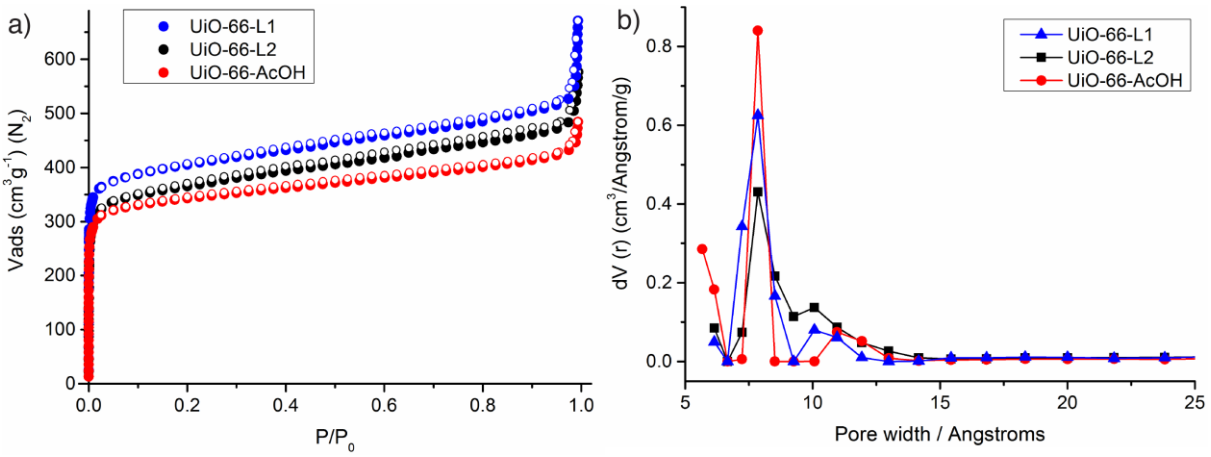

Figure S9. a) Adsorption and desorption isotherms (N_2, 77 K) of UiO-66-L1 and Ui-66-L2 modulated samples compared to UiO-66-AcOH. Filled symbols represent adsorption, empty symbols represent desorption. b) Pore size distribution (slit pore, N_2 at 77 K on carbon, QSDFT equilibrium model) of UiO-66-L1 and UiO-66-L2 modulated samples compared to UiO-66-AcOH.

The surface areas for the samples modulated by 5 equivalents of L1 and L2 are enhanced, while the pore size distribution of these modulated samples (Figure S9b) is similar to the reported for UiO-66 (8 Å and 11 Å).[S7] These results, together with the pore volume determination and the surface area of the nanoparticles, unequivocally confirm that the modulators are attached to the surface and defects sites and not stored in the pores of the NMOFs. In fact, when adding 5 equivalents of modulator to the synthetic process, the porosity of the particles increases, which could be attributed to defects induced in the structure, as attaching L1 or L2, with only one coordination site could lead to not fully connected zirconium positions.

S4. Characterisation of Surface-Modified NMOFs

General Procedure

In a typical CuAAC reaction performed on the modified MOF, 200 mg of the MOF in question, in this example UiO-66-L1, was placed in a 100 mL two neck round bottom flask. The MOF nanoparticles were dispersed in DCM (40 mL) by sonication (10 minutes). The solvent was bubbled with N_2, DiPEA (304 µL, 0.053 mmol, 4 mol %) was added, then acetic acid (92 µL, 0.053 mmol, 4 mol %) was added, CuI (5 mg, 0.0264 mmol, 2 mol %) was added,[S8] and the mixture was stirred for 5 min under N_2 atmosphere. 1-Azidodecane (200 mg, 1.1 mmol), or the alternative surface reagent, was added dropwise. The mixture was allowed to react for 24 hours at room temperature under nitrogen. The precipitate was collected by centrifugation and washed with DCM (x2) and methanol (x3).

Alkyl-Modified UiO-66

Proof-of-concept surface modification was carried out by reacting UiO-66-L1 with 1-dodecyne, and UiO-66-L2 with azidodecane. Sample integrity throughout the process was confirmed by PXRD (Figure S10).

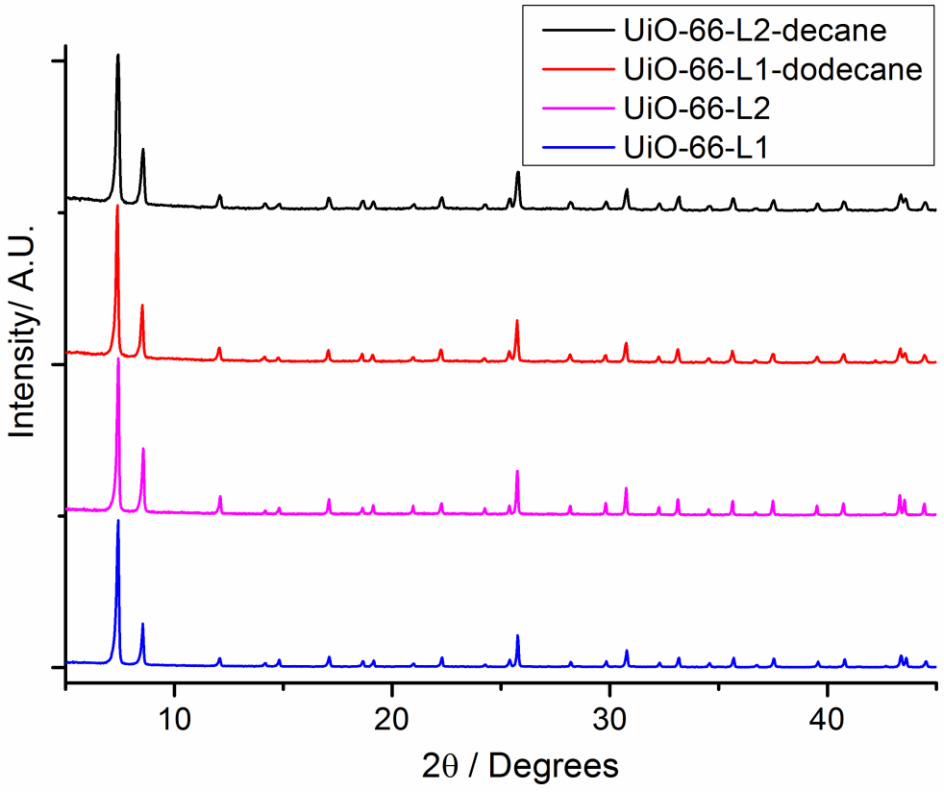

Figure S10. Stacked PXRD patterns of surface-modified UiO-66 nanoparticles

For high-resolution electrospray ionisation mass spectrometry (HRESI-MS) analysis, the surface modified NMOF samples were digested in an acidic aqueous solution, which was subsequently extracted with DCM. The organic phase was washed several times with an aqueous solution of Na_2EDTA in order to remove the metals present in solution. The organic phase was then evaporated and dissolved in a 1:1 mixture of MeOH and MeCN. Peaks were found for the products of the CuAAC reaction between modulators and surface functionality as follows:

UiO-66-L1-dodecane. Calcd $C_{20}H_{30}N_3O_2$ $[M+H]^+$: *m/z* = 344.2333; found: *m/z* = 344.2319.
UiO-66-L2-decane. Calcd $C_{20}H_{28}N_3O_3$ $[M-H]^-$: *m/z* = 358.2136; found: *m/z* = 358.2131.

Samples were prepared for ^1H NMR spectroscopy by digestion in D_2SO_4 / DMSO-d_6, although the low modulator content made analysis difficult. The conversion of the functional groups of the modulators was monitored by FTIR spectroscopy, including comparison of the spectra of the surface modified NMOFs with pristine samples where the modulator had been reacted with the respective surface component in solution (Figure S11). The low overall content of modulator in the samples means the signals are quite weak. For UiO-66-L1-dodecane, the N_3 signal (~2100 cm^{-1}) of L1 decreases considerably upon reaction, while the C-H region (2700-3000 cm^{-1}) shows signals for the surface alkyl unit. In the IR spectrum of UiO-66-L2-decane, the signal around 3250 cm^{-1} for the acetylene functionality of L2 is lost, and again new signals appear in the C-H region (2700-3000 cm^{-1}). Unfortunately, the signals expected for the triazole unit are masked by peaks from UiO-66 itself.

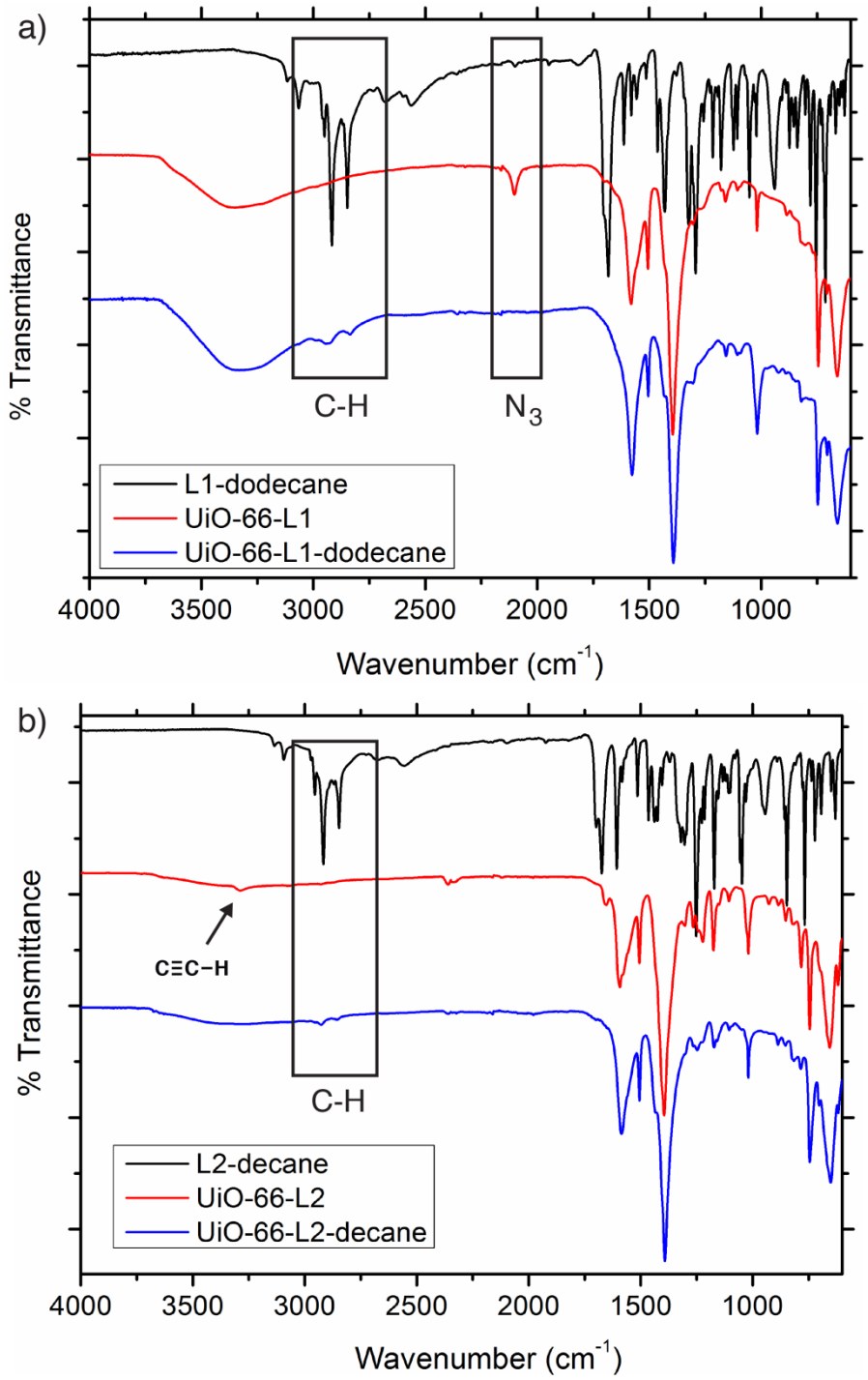

Figure S11. FTIR spectra comparing a) UiO-66-L1 before and after reaction with 1-dodecyne, as well as the product of the CuAAC reaction between L1 and 1-dodecyne, and b) UiO-66-L2 before and after reaction with azidodecane, as well as the product of the CuAAC reaction between L2 and azidodecane.

The porosity of the samples was determined by N_2 adsorption isotherms measured at 77 K (see Figure 2, main text) which confirmed that the samples remained porous and showed

slight decreases in gravimetric surface areas associated with incorporation of additional mass at the particle surfaces:

UiO-66-L1-dodecane: S_{BET} = 1168 m^2g^{-1}; pore volume = 0.623 ccg^{-1}.
UiO-66-L2-decane: S_{BET} = 1262 m^2g^{-1}; pore volume = 0.587 ccg^{-1}.

Thermogravimetric analysis was used to investigate the incorporation of surface functionality. For UiO-66-L1-dodecane, additional mass loss events are obvious in the TGA traces recorded in air (Figure S12a) and under nitrogen (Figure S12b). These mass loss events occur at temperatures higher than the decomposition of the isolated product of the CuAAC reaction between L1 and dodecane, indicating covalent attachment to the NMOF, and a surface functionality component of around 10% *w/w*.

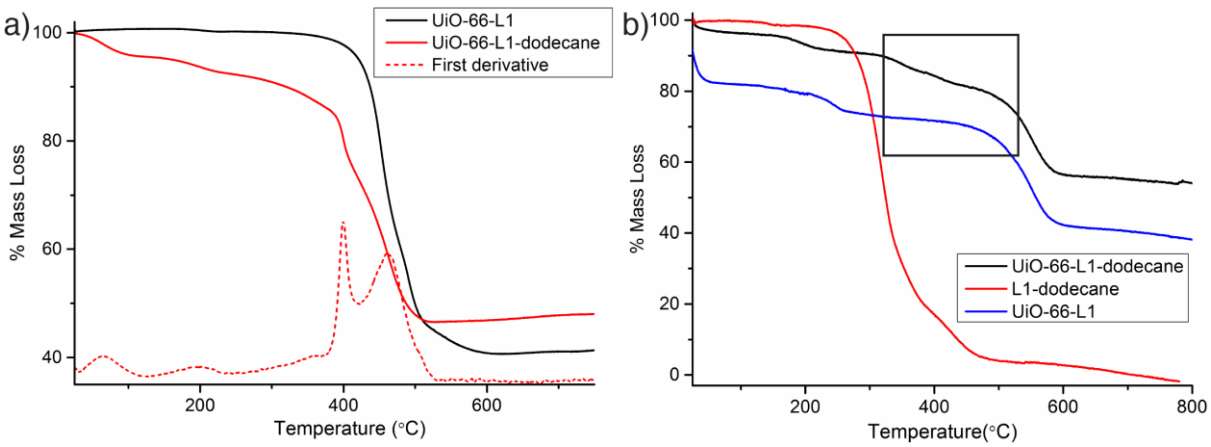

Figure S12. a) Comparison of TGA traces in air of UiO-66-L1 before and after reaction with 1-dodecyne. b) Comparison of TGA traces in nitrogen of the MOFs as well as the isolated "clicked" material L1-dodecane.

Similar TGA analysis was carried out on UiO-66-L2 and its functionalised analogue UiO-66-L2-decane. In both the TGA traces recorded in air (Figure S13a) and under nitrogen (Figure 13b), there is a high temperature mass loss event corresponding to covalently attached surface functionality, with a weight content of around 10% *w/w*.

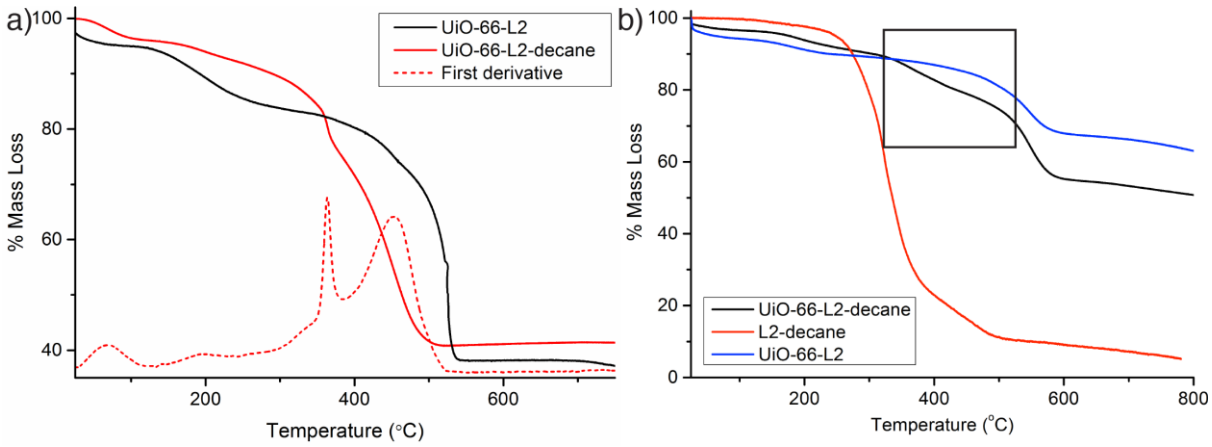

Figure S13. a) Comparison of TGA traces in air of UiO-66-L2 before and after reaction with 1-azidodecane. b) Comparison of TGA traces in nitrogen of the MOFs as well as the isolated "clicked" material L2-decane.

SEM imaging was used to examine the morphology and size of the NMOFs after surface modification. In both cases, it can be seen that particle size and morphology is retained after the click modulation protocol (Figure S14).

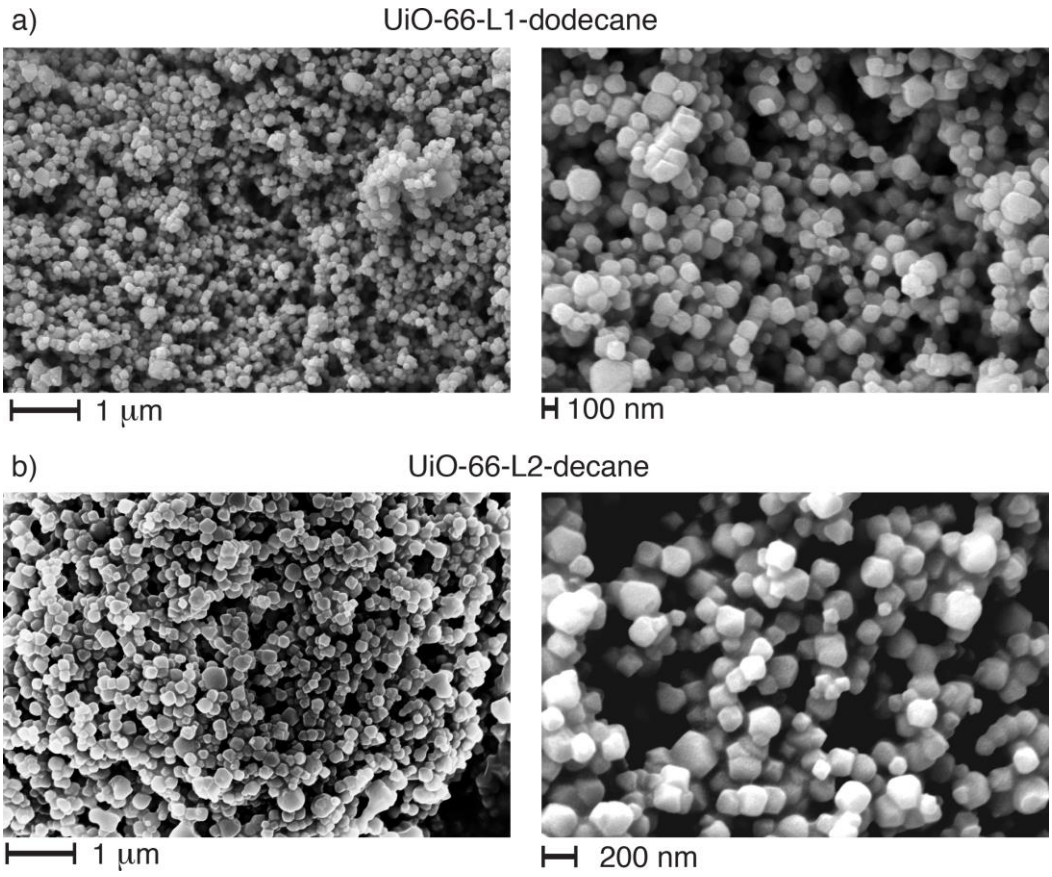

Figure S14. SEM images of a) UiO-66-L1-dodecane and b) UiO-66-L2-decane.

PEG-modified UiO-66

UiO-66-L1 was chosen for modification with propargyl-functionalised poly(ethylene glycol) chains of two different sizes, PEG550 (M_n = 550) and PEG2000 (M_n = 2000). Thermogravimetric analysis, shown in Figure 3 in the main text, confirms the incorporation of the PEG units and strongly indicates that covalent attachment is required for their incorporation, as no mass loss events corresponding to PEG units are seen in control samples where the MOFs are simply soaked in PEG solutions without a catalyst for the CuAAC conjugation protocol. The level of PEG incorporation was estimated to be 21.7% *w/w* and 23.1% *w/w*, for UiO-66-L1-PEG550 and UiO-66-L1-PEG2000, respectively.

Samples for HRESI-MS were prepared by the acid digestion protocol described for the alkyl modified materials. Whilst a series of peaks corresponding to covalently modified PEG550 (the molecules of different chain lengths are present in the starting material) are clearly visible in the mass spectrum of UiO-66-L1-PEG550 (Figure S15), it was not possible to ionise the larger PEG2000 chains by ESIMS or MALDI-TOF. This was common to the precursors and to the digested MOFs.

n **(UiO-66-L1-PEG550)**	***m/z*** **(+Na⁺)**	
	calculated	measured
6	578.2690	578.2657
7	622.2952	622.2929
8	666.3214	666.3180
9	710.3476	710.3446
10	754.3738	754.3701
11	798.4000	798.3966
12	842.4263	842.4230
13	886.4525	886.4530
14	930.4787	930.4758

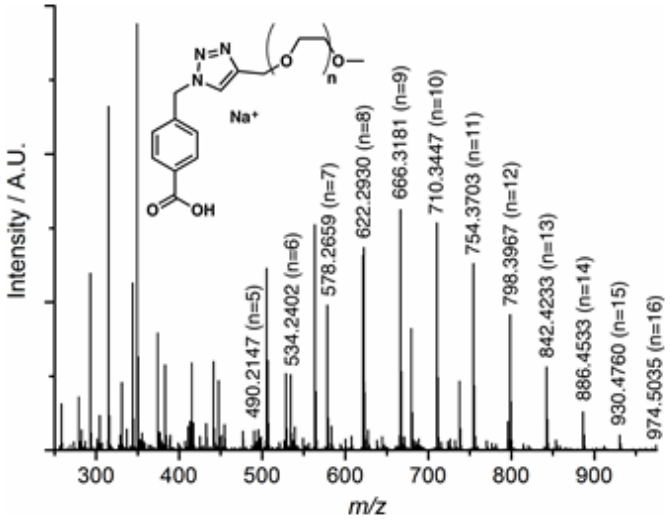

Figure S15. ESIMS of digested UiO-66-L1-PEG550 and a table of observed peaks for covalently modified PEG chains of different lengths.

FTIR spectra were collected to monitor the functional group conversion and incorporation of the PEG units to UiO-66-L1. For both UiO-66-L1-PEG550 (Figure S16a) and UiO-66-L1-PEG2000 (Figure S16b), there is a noticeable decrease in intensity of the azide signal around 2300 cm^{-1}, indicating conversion of the surface L1 units, and signals for the C-H

functionality of the PEG chains are observed. There are no signals in the surface modified MOFs for the alkyne units of the PEG precursors, again indicating that PEG incorporation occurs through covalent attachment rather than adsorption.

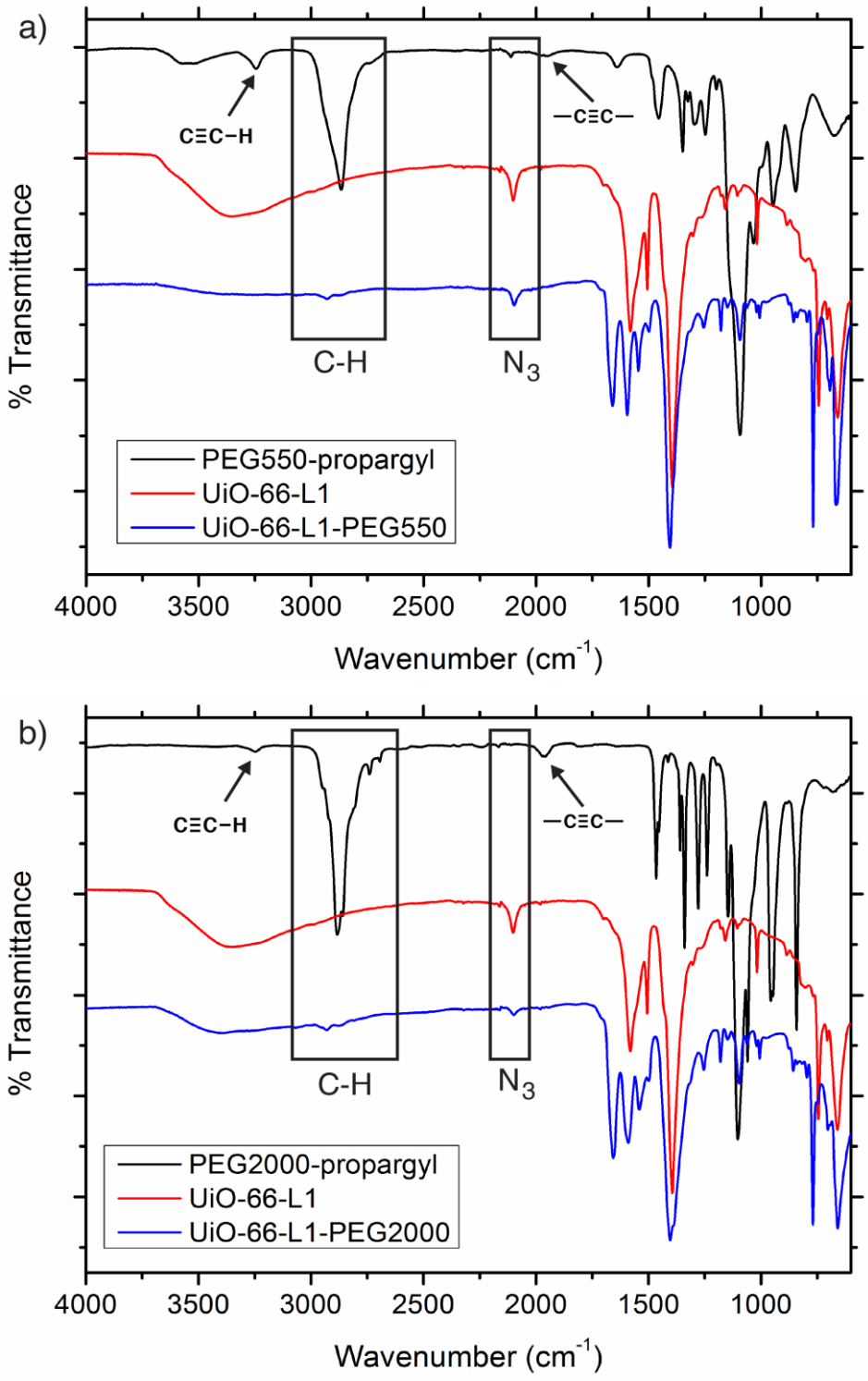

Figure S16. FTIR spectra comparing a) UiO-66-L1-PEG550 with the two starting materials used in its synthesis, and b) UiO-66-L2-PEG2000 with the two starting materials used in its preparation.

PXRD analysis showed that the PEGylated NMOFs retained their crystallinity (Figure S17).

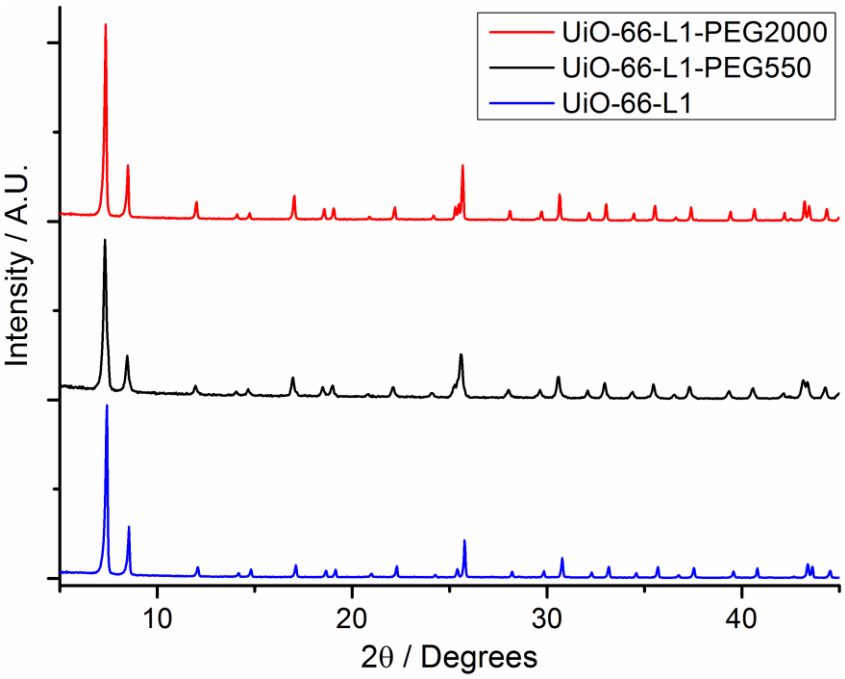

Figure S17. Stacked PXRD patterns of UiO-66-L1 and its PEGylated derivatives.

SEM was used to ensure particles were not degraded during the surface modification protocol (Figure S18). For both UiO-66-L1-PEG550 and UiO-66-L1-PEG2000, the particles remained intact, and as the chain length increased, the morphology of the NMOFs tended towards spherical, rather than the well-defined octahedral of UiO-66-L1. The long polymer chains are clearly being installed at the surface, leading to an overall rounding of the particles.

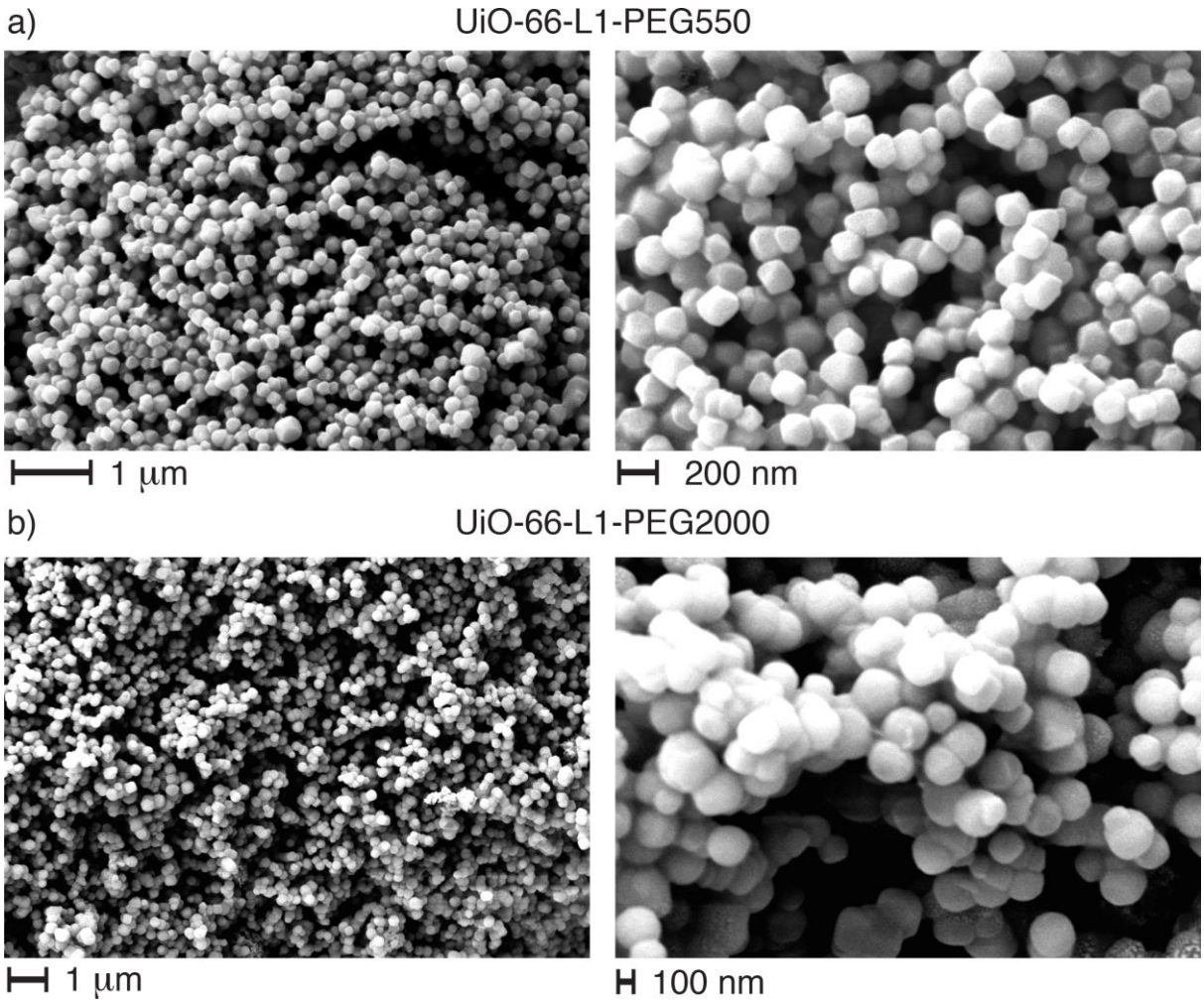

Figure S18. SEM images of a) UiO-66-L1-PEG550 and b) UiO-66-L1-PEG2000.

The particle size distributions before and after PEGylation were analysed manually using the ImageJ software package (Figure S19). The average size of UiO-66-L1 particles was found to be 146.6 ± 29.3 nm, which increased upon PEGylation to 160.2 ± 26.9 nm for UiO-66-L1-PEG550 and to 172.9 ± 36.8 nm for UiO-66-L1-PEG2000. This size increase is consistent with the increasing size of the surface polymer chains being installed on the nanoparticles' surfaces, but the magnitude of the size change may be affected by the accompanying change in morphology from octahedral to roughly spherical particles upon surface modification. A comparison of the particle size histograms for all three samples is given in Figure S20.

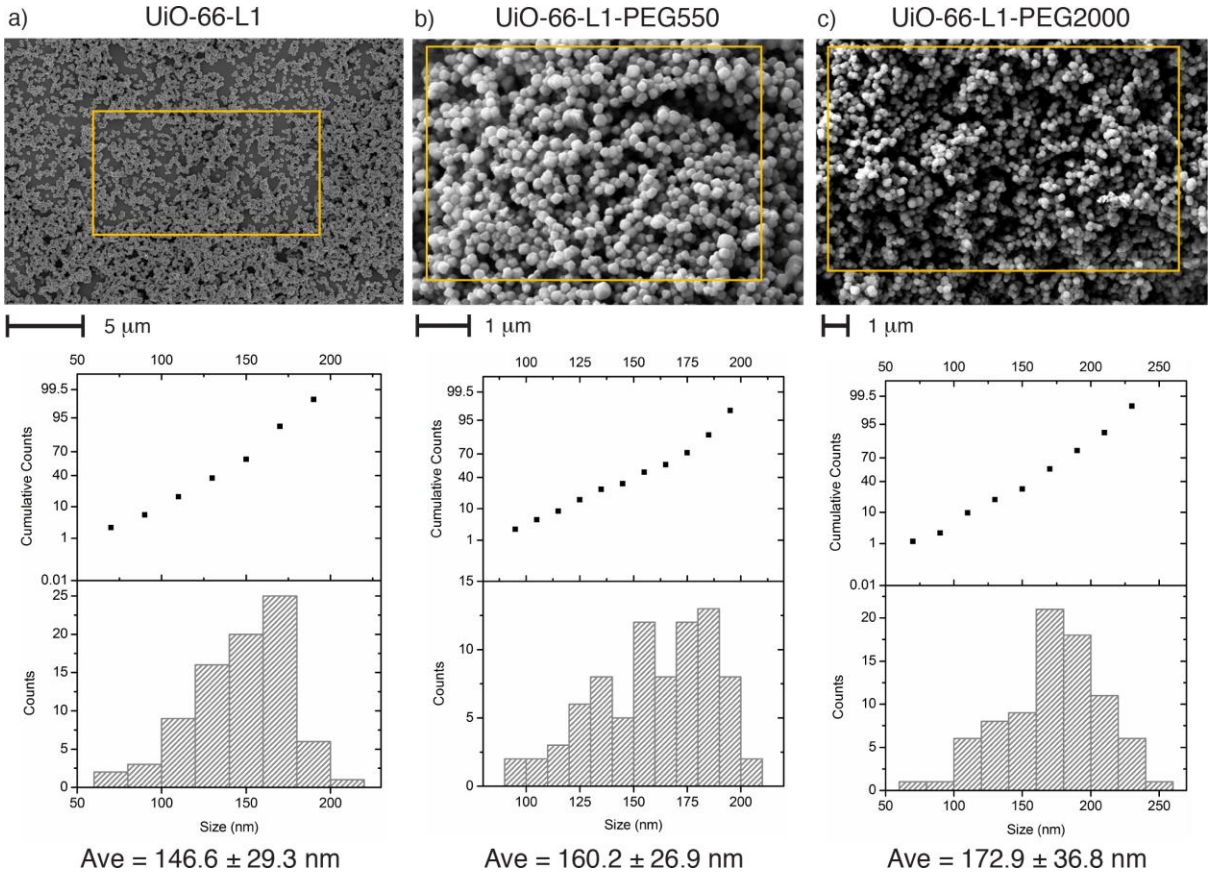

Figure S19. Particle size analysis from SEM micrographs for a) UiO-66-L1, b) UiO-66-L1-PEG550, and c) UiO-66-L1-PEG2000.

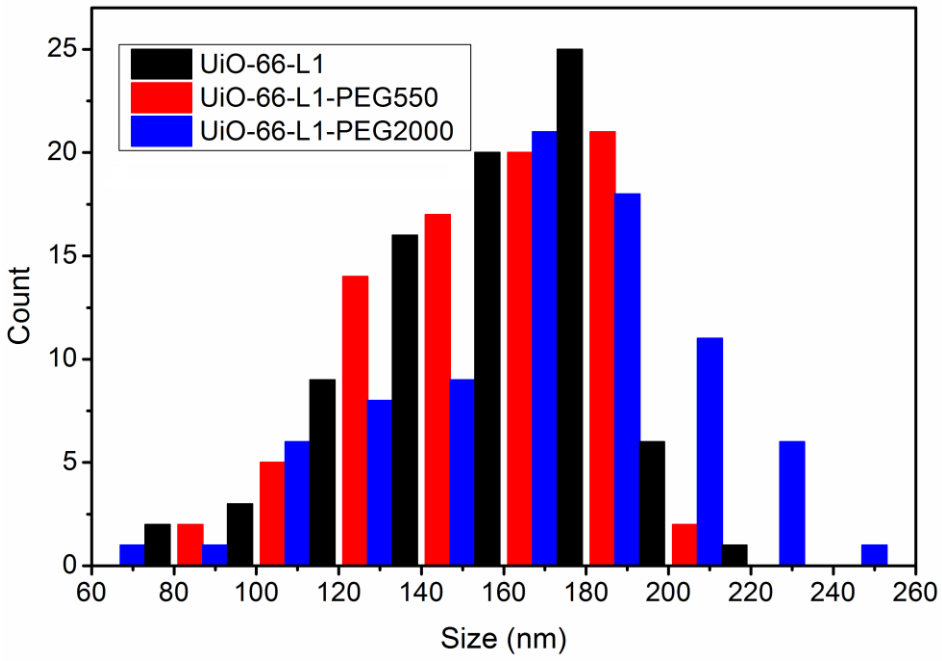

Figure S20. Comparison of particle size histograms for the three samples analysed with ImageJ.

Dynamic light scattering (DLS) was used to monitor particle size and aggregation in solution, before and after surface modification. In a scintillation vial, dispersions with a concentration of 250 μg of MOF per mL of dispersant were prepared by sonication over 5 min prior to the measurement of each sample. Three recordings, consisting of 14 runs each, were performed consecutively on the same sample for each measurement. The waiting time between recordings was 5 seconds. No stirring was provided during the course of the experiment.

When samples were dispersed in MeOH (Figure S21), the effect of surface PEGylation is clear. Both UiO-66-AcOH and UiO-66-L1 aggregate in solution, which may be a result of their hydrophilic surfaces, although UiO-66-L1 displays smaller aggregates than UiO-66-AcOH. The PEGylated samples show much smaller size in solution, with average diameters around 150 nm correlating well with SEM data, suggesting well dispersed particles with no aggregation as a consequence of their PEG surfaces.

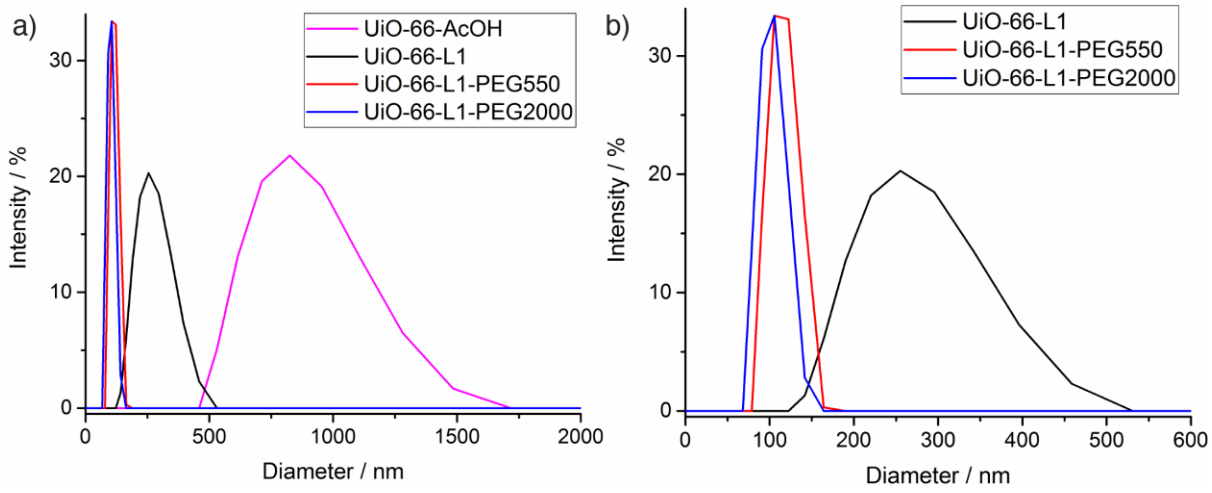

Figure S21. a) Dynamic light scattering (DLS) measurements of UiO-66 samples in methanol. b) Zoom in on DLS data for smaller particle sizes.

DLS measurements were also carried out in water (Figure S22), but it was found to be difficult to generate stable dispersions of UiO-66-L1. Aggregation and precipitation was observed, but aggregates around 2000-3000 nm were typically in initial measurements. The PEGylated samples showed much less aggregation, in particular UiO-66-L1-PEG2000, which has a much larger surface corona of water-compatible PEG chains and so stabilises small aggregates around 500 nm in size.

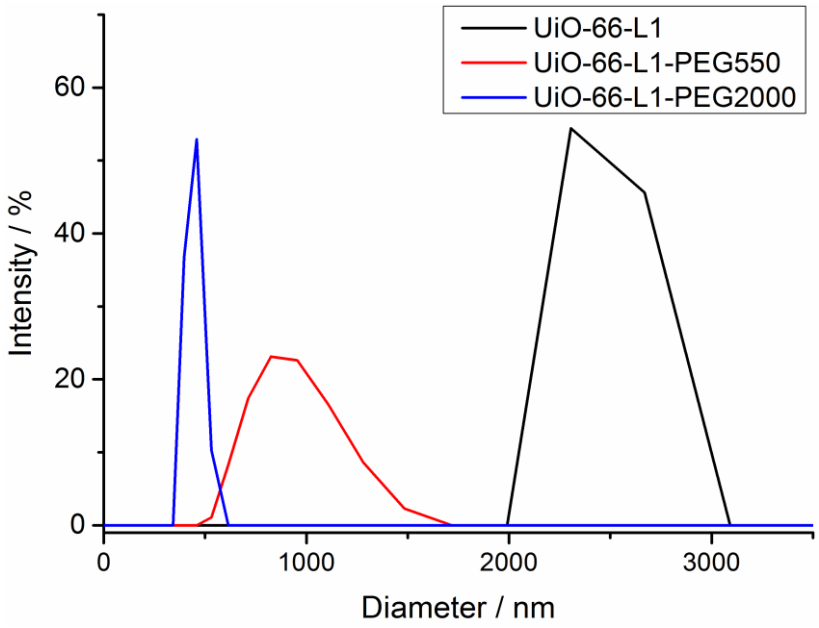

Figure S22. Dynamic light scattering measurements of UiO-66 samples in water.

During repeated DLS experiments run over 10 minutes, it was observed that UiO-66-L1-PEG2000 gradually aggregated (Figure S23), from particles around 250 nm to around 500 nm in diameter. Aggregates of UiO-66-L1-PEG550 across a broad size range around 1000 nm had, in contrast, stabilised rapidly prior to measurement, again indicating the significant effect of larger PEG chains on hydrodynamic behaviour of the UiO-66 nanoparticles.

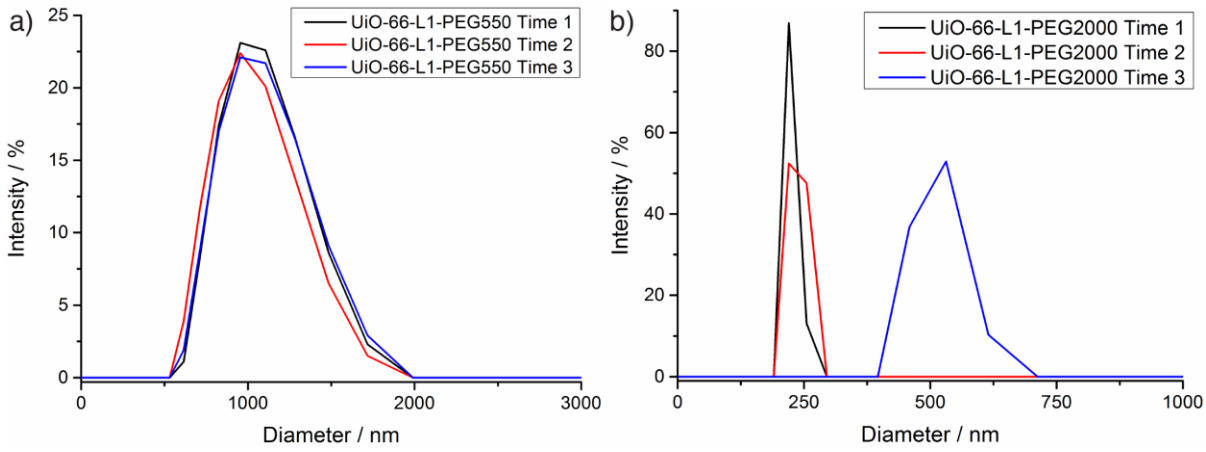

Figure S23. Time dependent aggregation observed during DLS measurements for a) UiO-66-L1-PEG550, and b) UiO-66-L1-PEG2000.

As the PEGylated UiO-66 samples were intended for use as drug delivery vectors, their cytotoxicities towards HeLa cells, as well as those of the modulators L1 and L2, were

investigated using the 3-(4,5-dimethylthiazol-2-yl)-5-(3-carboxymethoxyphenyl)-2-(4-sulfophenyl)-2H-tetrazolium (MTS) (Promega, UK) reduction assay. UiO-66 itself has previously been found to be non-toxic using this methodology.[S9]

HeLa cells were maintained at 37 ºC with 5% CO_2 in high rich glucose (4500 mg/L) Dulbecco's modified Eagle's Medium (DMEM) with phenol red supplemented with 10% (*v/v*) Fetal Bovine Serum (FBS), 2 mM L-glutamine, 100 units/mL penicillin and 100 µg/mL streptomycin. This was named complete DMEM (cDMEM). The cells were passaged three times a week (at 75-80% of confluence) at a density of 2.8 x 10^4 cell/cm^2.

The day before the experiment, cells were seeded into a 96 well plate at a density of 10 x 10^3 cells per well. Prior to the treatments, cells were washed twice with PBS. The MOFs and modulators were dissolved/suspended in cDMEM at different concentrations. They were then added to the cells and incubated for 72 h at 37 ºC with 5% CO_2. To measure the toxicity, the cells were washed three times with phosphate buffered saline (PBS), the media was replaced with 100 µL of fresh culture media containing 20 µL of MTS/phenazine methosulfate (in a proportion 20:1) solution, and the plate was incubated for 1 h at 37 ºC with 5% CO_2. The plates were read at 490 nm by UV/Vis spectrophotometry.

No decrease in cell viability was observed up to 1 mg/mL concentration of either of the modulators (Figure S24), confirming that they are non-toxic. Similar results were obtained for the PEGylated UiO-66 samples (Figure S25).

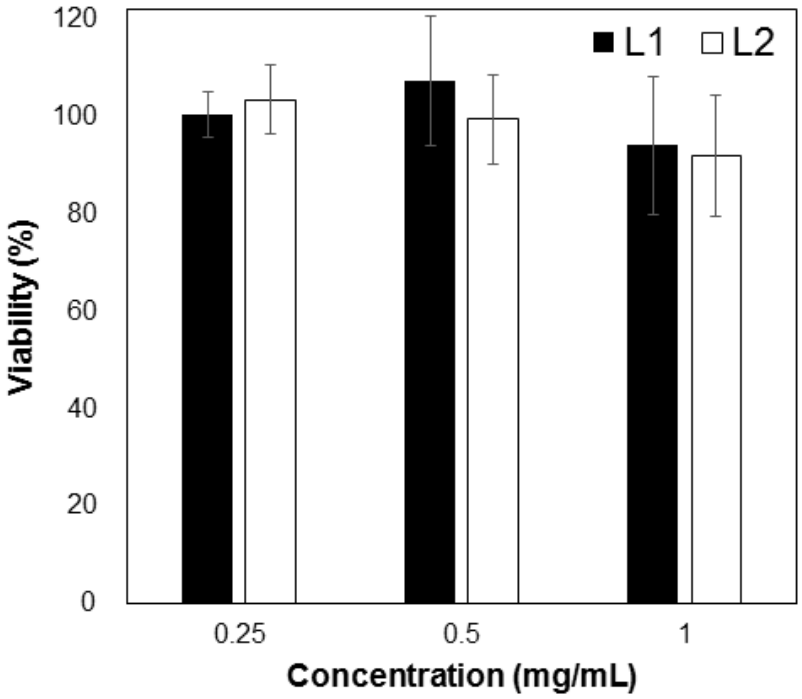

Figure S24. Metabolic activity of HeLa cells after 72 h of exposure to L1 and L2, measured by MTS assay.

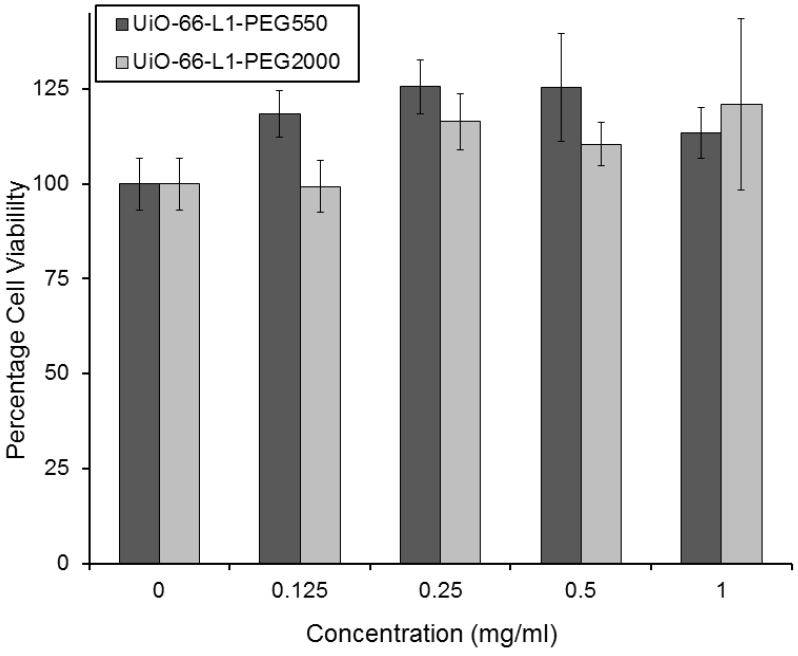

Figure S25. Metabolic activity of HeLa cells after 72 h of exposure to UiO-66-L1-PEG550 and UiO-66-L1-PEG2000, measured by MTS assay.

S5. Stability of Surface-Modified NMOFs

To obtain the degradation profile of the different UiO-66 nanoparticles, around 10 mg of sample were dispersed in a dialysis bag with 10 mL of phosphate buffered saline (PBS) at pH 7.4, and dialysed against 100 mL of PBS under magnetic stirring at room temperature. The release of the bdc linker, indicative of degradation, was measured by UV-Vis spectroscopy. The quantity of bdc (% *w/w*) present in the different UiO-66 samples was calculated based on the TGA measurements detailed in Section S3, being 46.8% *w/w* for UiO-66-AcOH and 59.1% *w/w* for UiO-66-L1. The initial linker weight for UiO-66-L1 was corrected with the weight of PEG in the new sample, previously determined by TGA analysis in Section S4.

$$Linker\ wt\% = 59.08 * (1 - \frac{\text{PEG wt\%}}{100})$$

A calibration curve of bdc in PBS pH 7.4 was performed (λ_{max} = 241 nm) and shown in Figure S26a. Solutions of bdc and L1 of the same concentration were measured revealing a maximum absorbance peak at 234 nm for L1 with a very similar extinction coefficient to bdc. When the absorbance of a solution of both bdc and L1 (1:1) was measured, a maximum peak absorbing at 238 nm was determined with a very similar extinction coefficient to bdc on its own (Figure S26b).

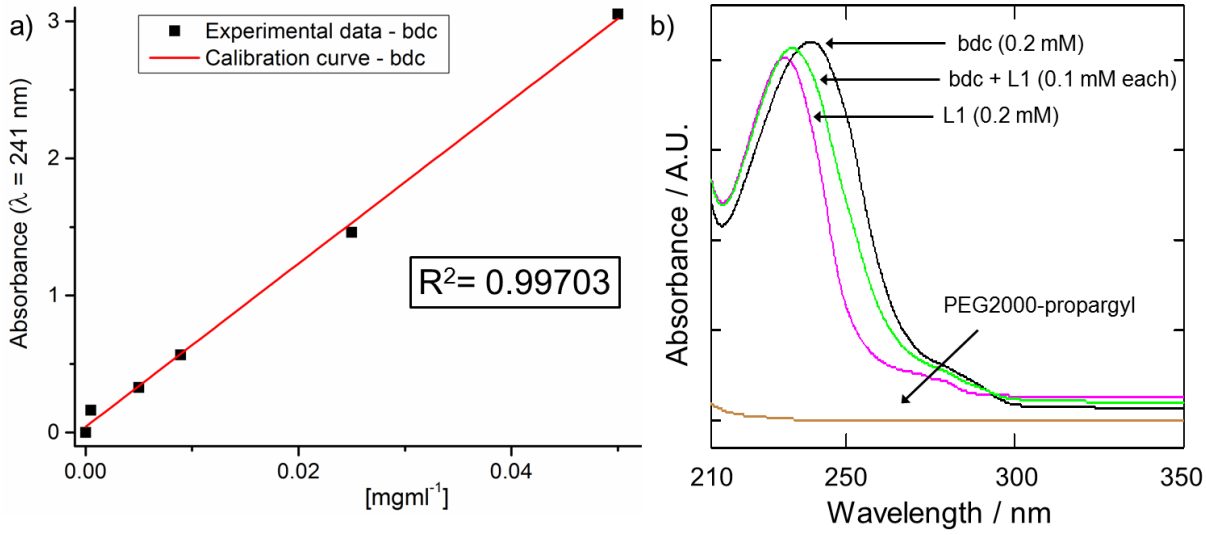

Figure S26. a) Calibration curve of bdc absorbance at λ = 241 nm in PBS at pH 7.4. b) UV-Vis spectra of PEG2000-propargyl (brown), L1 (pink), bdc (black), and a mixture of L1 and bdc (green).

Due to the overlapping absorbance of L1 and bdc, the fact that the presence of L1 does not affect the bdc absorbance, and as the quantity of L1 present in sample (determined by ^{1}H NMR) is very small compared to bdc, the bdc calibration curve in Figure S26 was used.

Each measurement was taken *in situ* (from 210 nm to 330 nm, Figure S27) and the liquid was introduced back to the dialysis media before prior measurement. Each experiment was performed separately 3 times to determine the error and each calculation was performed with the exact mass of NMOF added.

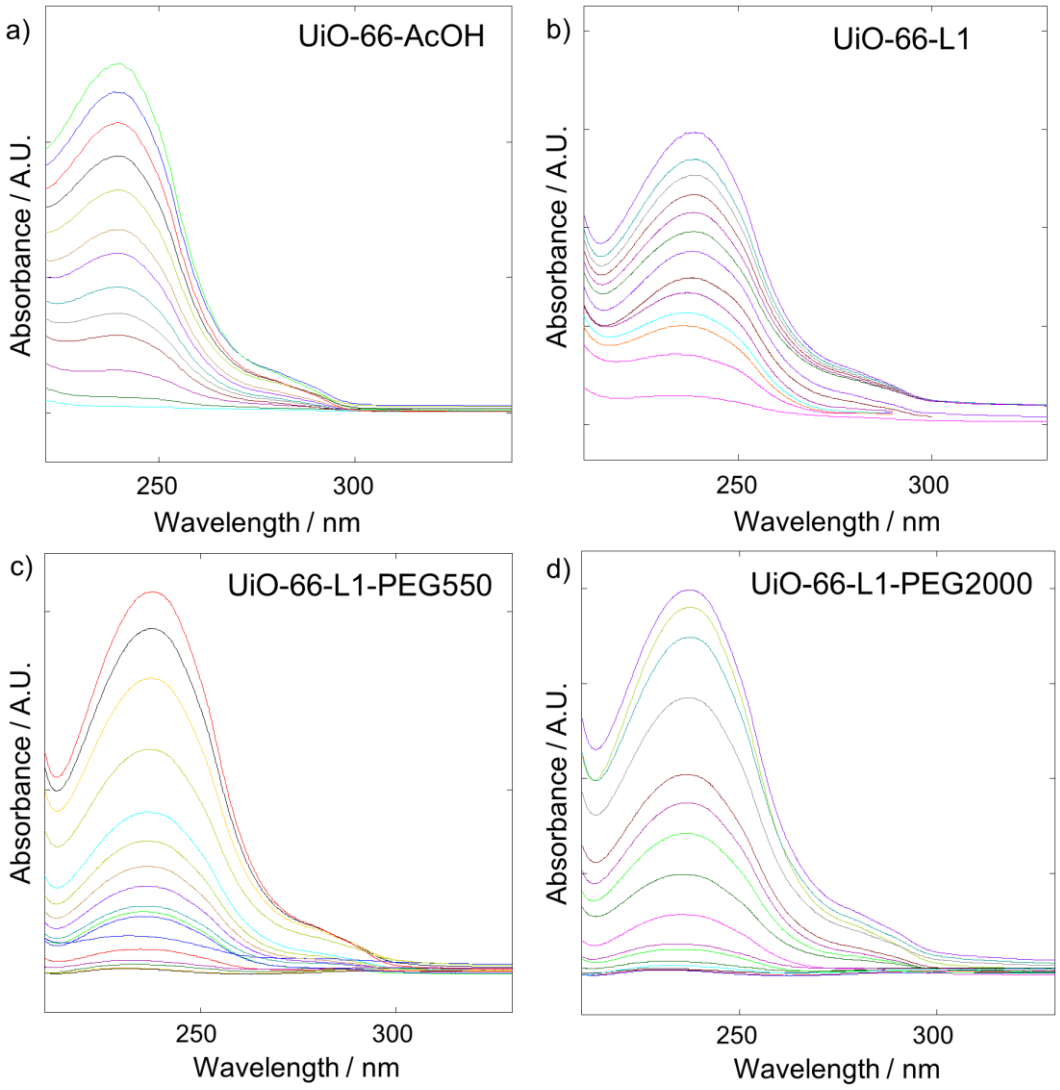

Figure S27. UV-Vis spectra (210-330 nm) of the degradation profiles of the different samples in PBS.

In a typical calculation of the percentage of bdc released, based on the maximum absorbance of the dialysis media, the following calculations were performed:

$$mg\ of\ sample * wt\%\ bdc\ in\ sample = mg\ of\ bdc \rightarrow \frac{mg}{ml} bdc \rightarrow Maximum\ absorbance$$

$$\frac{\text{Experimental absorbance}}{Maximun\ absorbance} * 100 = \%\ bdc\ Released$$

The degradation profiles were collected in triplicate and are plotted in Figure S28, showing significant differences for PEGylated samples compared to uncoated samples. There is a clear enhancement in stability for the PEGylated samples, which also degrade with a different kinetic profile.

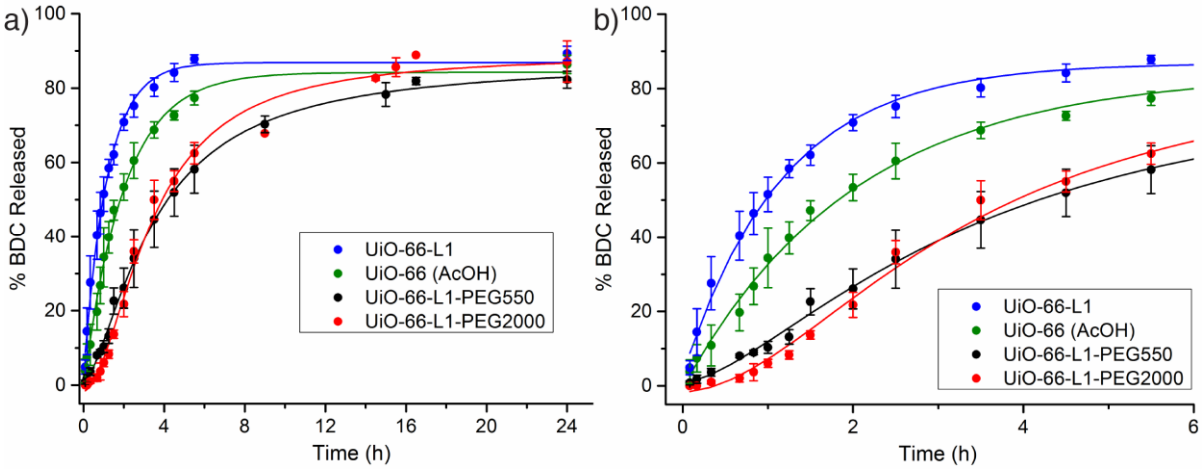

Figure S28. a) Degradation profiles of coated and uncoated UiO-66 nanoparticles in PBS pH 7.4, with b) an inset of the early time period. Error bars denote standard deviations from triplicate experiments.

The kinetic profiles for the degradation of the samples were subsequently determined by curve fitting utilising Microcal Origin software. The uncoated samples, UiO-66-AcOH and UiO-66-L1, exhibit (Figure S29) exponential degradation profiles: $y= y_0 +A_1e^{x/t1}$. In contrast, the PEGylated samples exhibit (Figure S30) sigmoidal degradation profiles: y= start + (end-start)$(x^n/(k^n+x^n))$, clearly indicating a different initial degradation mechanism.

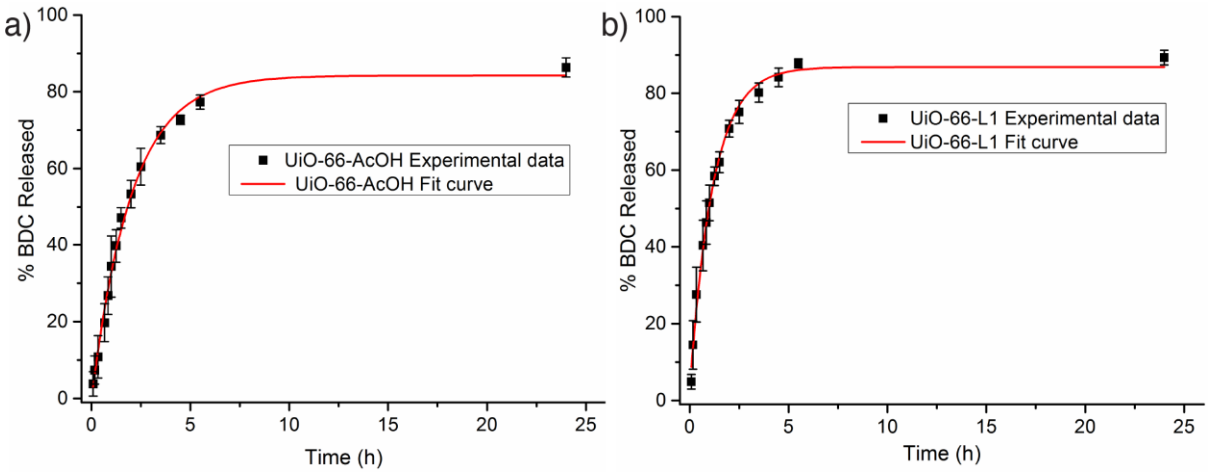

NMOF	Degradation equation	R^2
UiO-66-AcOH	% bdc released = 84.235 -84.749 $e^{t/2.011}$	R^2= 0.99415
UiO-66-L1	% bdc released = 86.863 -83.831 $e^{t/1.897}$	R^2= 0.99351

Figure S29. Degradation profiles of UiO-66-AcOH and UiO-66-L1 with curve fittings. Error bars denote standard deviations from triplicate experiments.

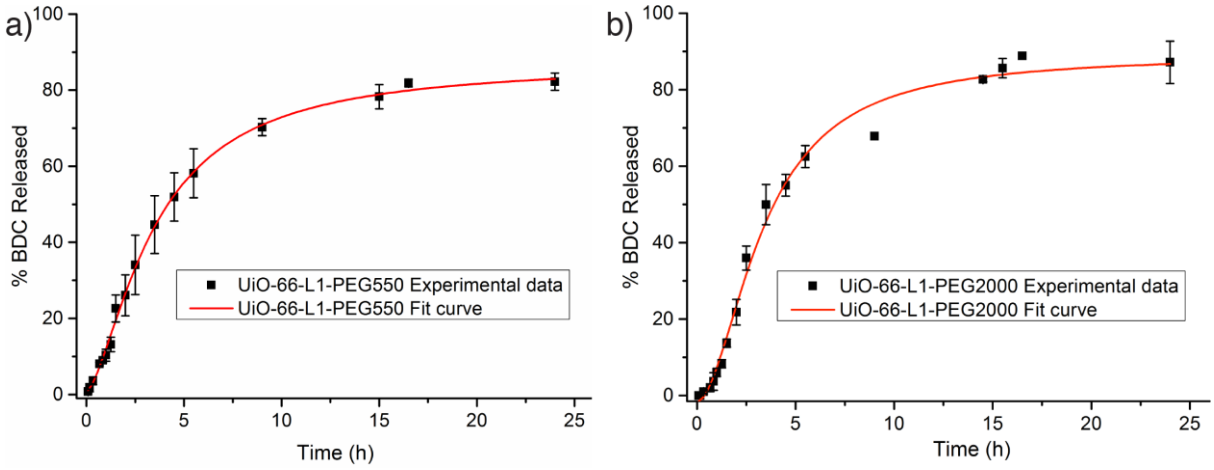

NMOF	Degradation equation	R^2
UiO-66-L1-PEG550	% bdc released = 0.72412 + 86.50317 ($t^{0.07977}$/(1.1607+$t^{0.07977}$))	R^2= 0.9977
UiO-66-L1-PEG2000	% bdc released = -1.6399+ 89.0698 ($t^{1.83984}$/(9.2853+$t^{1.8398}$))	R^2= 0.99078

Figure S30. Degradation profiles of UiO-66-L1-PEG550 and UiO-66-L1-PEG2000 with curve fittings. Error bars denote standard deviations from triplicate experiments.

The effect of exposure of the UiO-66 nanoparticles to PBS buffer on their crystallinity was investigated by powder X-ray diffraction. In the general procedure, 20 mg of the UiO-66 nanoparticles were dispersed in PBS buffer (pH 7.4, 20 mL) by sonication (5 minutes), and stirred for different contact times. Then, the nanoparticles were collected by centrifugation and washed with fresh water. After being dried for 24 h under vacuum, their crystallinity was analysed by PXRD (Figure S31).

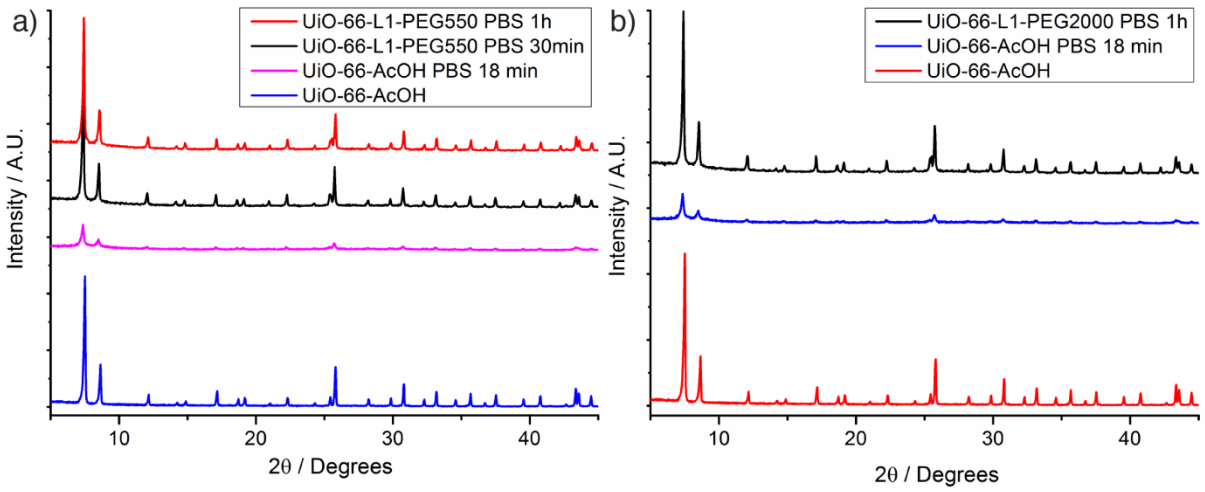

Figure S31. Stacked PXRD patterns of UiO-66 samples after different contact times with PBS buffer for a) UiO-66-L1-PEG550 and b) UiO-66-L1-PEG2000.

The samples clearly exhibit different stabilities under the experimental conditions, with uncoated UiO-66 samples rapidly losing crystallinity, while the PEGylated samples remain highly crystalline after an hour.

S6. Characterization of Calcein Loaded NMOFs

General Procedure for Calcein Loading

200 mg of UiO-66-L1 was dispersed by sonication (15 minutes) in 100 mL of a methanolic solution of calcein (10 mg/mL), and stirred at room temperature for 48 hours. The solid was collected by centrifugation (4500 rpm, 20 min), and submitted to dispersion centrifugation cycles with fresh methanol until the supernatant solution remained colorless (around 5 times). The calcein loaded material, cal@UiO-66-L1, was obtained as a bright orange powder.

General Procedure for Surface Modifying Calcein Loaded Samples

The same CuAAC procedure detailed in Section S4 was used to prepare the calcein loaded materials, cal@UiO-66-L1-PEG550 and cal@UiO-66-L1-PEG2000. The reaction media did not acquire an intense orange color, as no considerable amounts of calcein were released during the process.

Powder X-ray diffraction data (PXRD) confirmed that the samples remained crystalline after calcein loading and subsequent surface PEGylation (Figure S32).

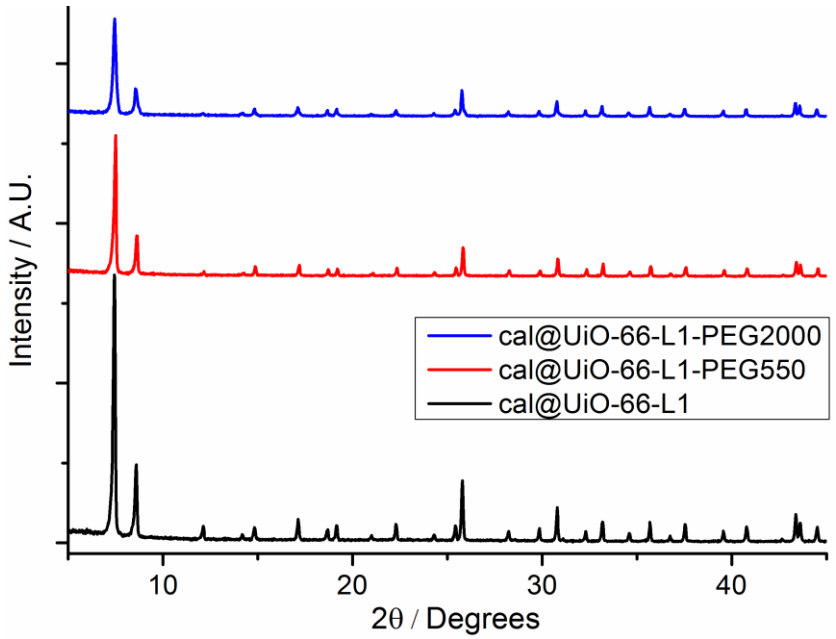

Figure S32. Stacked PXRD patterns of calcein-loaded UiO-66 samples.

The retention of sample integrity was further suggested by SEM imaging of calcein loaded samples, which showed little change in overall size but some rounding (Figure S33).

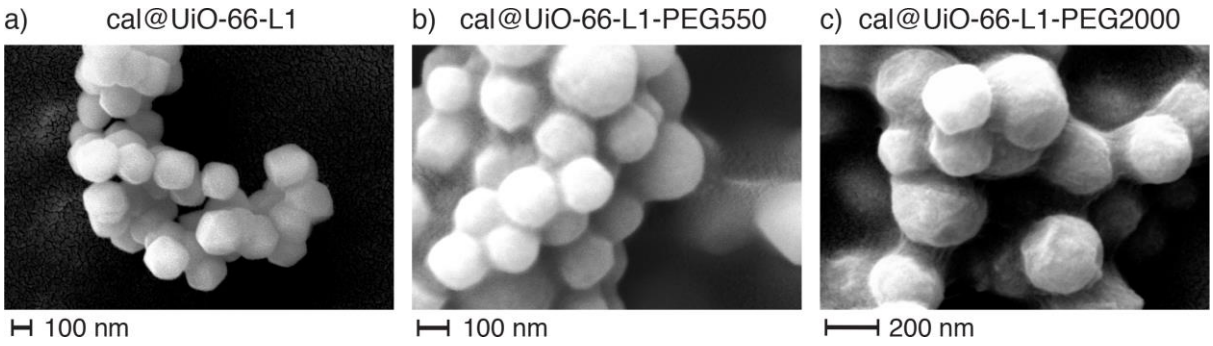

Figure S33. SEM images of a) cal@UiO-66-L1, b) cal@UiO-66-L1-PEG550, and c) cal@UiO-66-L1-PEG2000.

The calcein content of the MOFs was determined by UV-Vis spectroscopy of acid digested samples. 1 mg of sample was dispersed, heated in PBS buffer pH 5.5 (10 mL) and stirred for 48 hours. The sample was centrifuged before the analysis of the calcein absorbance in the PBS solution against a previously prepared calibration curve (Figure S34), and the remaining solid NMOF was confirmed visually to have lost the characteristic orange color form the calcein.

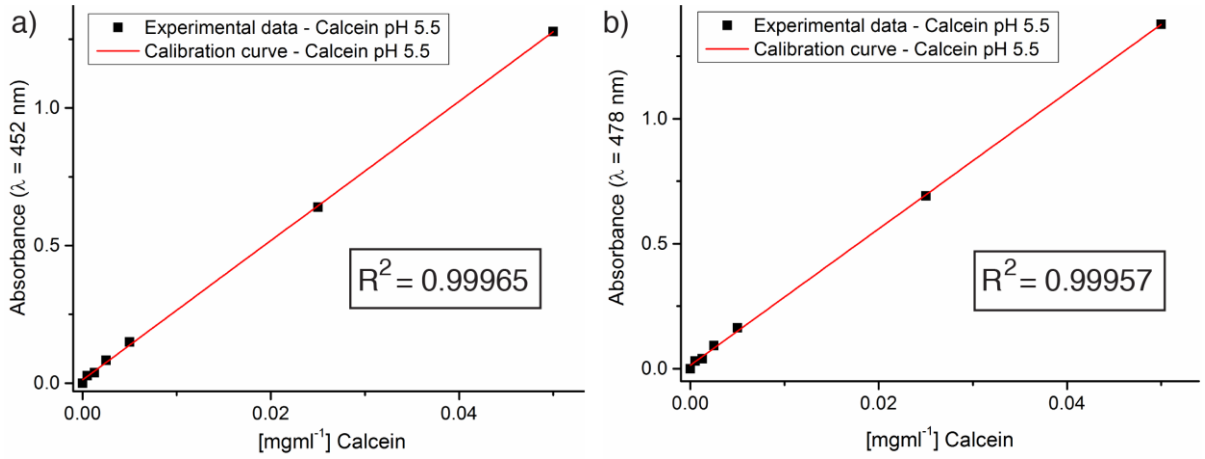

Figure S34. UV/Vis spectrophotometric calibration curves for calcein absorbance in PBS pH 5.5.

Based on the solution absorbance, the calcein concentration was determined. In order to obtain the weight percent of calcein in the samples, the following calculation was performed:

$$[mg/ml]\ of\ Calcein * 10\ ml = mg\ of\ Calcein$$

$$\frac{mg\ of\ Calcein}{\text{mg of NMOF}} * 100 = Calcein\ wt\%$$

The analysis of the UV/Vis spectrophotometric data gave the following loading values:

cal@UiO-66-L1: 16.1% *w/w*.
cal@UiO-66-L1-PEG550: 13.1% *w/w*.
cal@UiO-66-L1-PEG2000: 10.3% *w/w*.

Investigation of calcein content was carried out by thermogravimetric analysis (Figure S35).

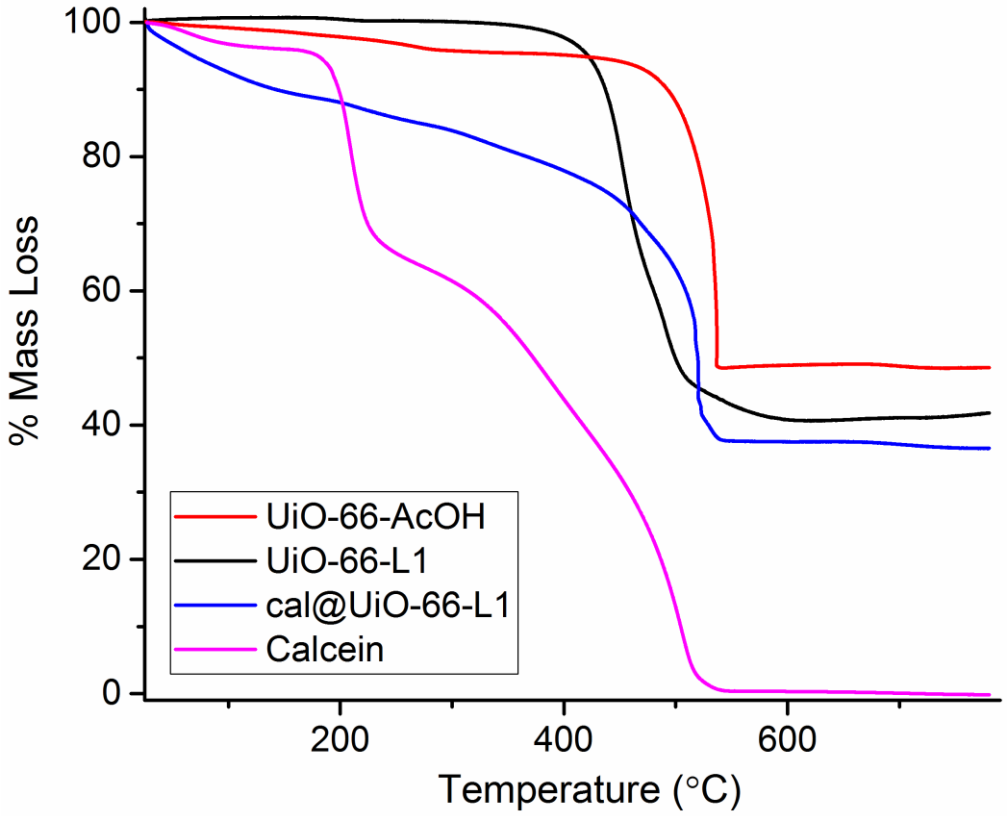

Figure S35. TGA profiles of cal@UiO-66-L1 in air and its comparison with UiO-66-AcOH, UiO-66-L1 and calcein.

For cal@UiO-66-L1, the absence of a significant calcein decomposition step at 200 ºC, together with its bigger size compared to the pore cavity, suggests that calcein is attached to the zirconium clusters present in the surface and defect sites through its carboxylic acid groups. The multi-step degradation profile makes quantitative calcein content analysis by TGA difficult, however, it is clearly present.

Similar TGA analysis was carried out on the samples which had been surface modified with PEG chains (Figure S36).

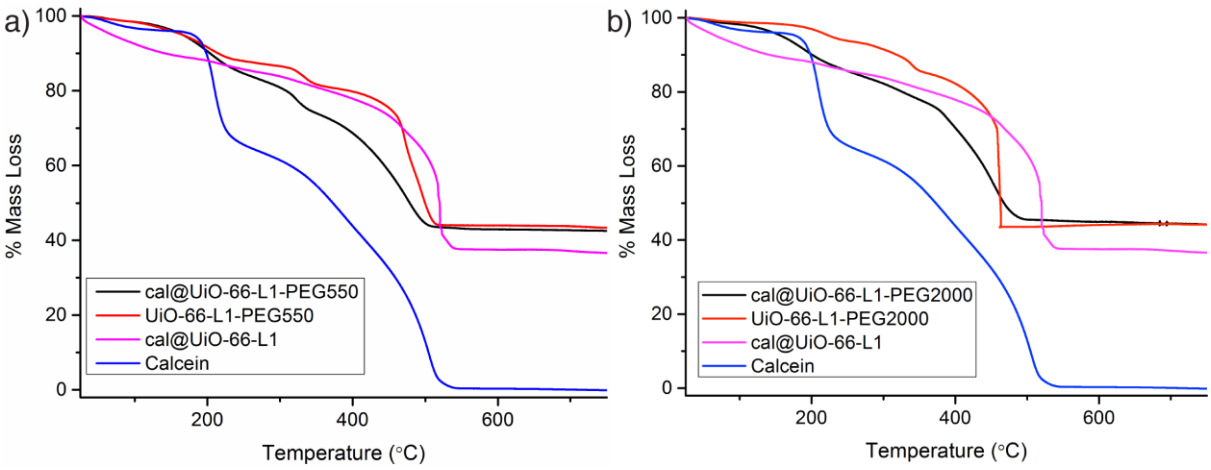

Figure S36. a) TGA traces of cal@UiO-66-L1-PEG550 in air and its comparison with cal@UiO-66-L1, UiO-66-L1-PEG550, and calcein. b) TGA traces of cal@UiO-66-L1-PEG2000 in air and its comparison with cal@UiO-66-L1, UiO-66-L1-PEG2000 and calcein.

The appearance of a new degradation step at the reported degradation temperature of PEG[S10] confirms that the PEGylation has been successful. As the thermal degradation of calcein and PEG occur across the same temperature ranges, it is not possible to determine exact contents of either functionality by TGA.

Adsorption isotherms (N_2, 77 K) were used to investigate the mode of calcein incorporation (Figure S37).

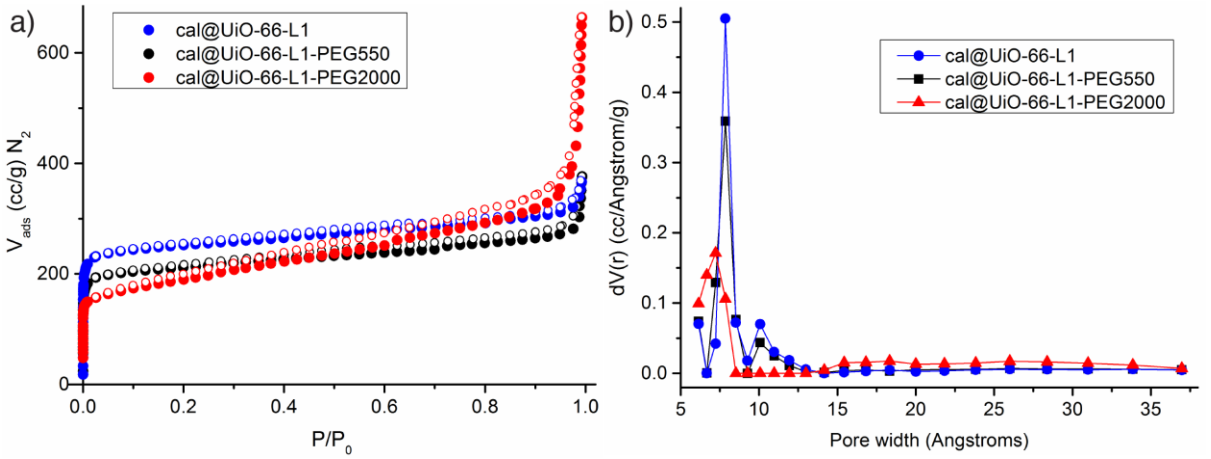

Figure S37. a) Adsorption and desorption isotherms (N_2, 77 K) of calcein loaded UiO-66 samples. Filled symbols represent adsorption, empty symbols represent desorption. b) Pore size distribution (slit pore, N_2 at 77 K on carbon, QSDFT equilibrium model) of the calcein loaded UiO-66 samples.

It is clear that the samples remain porous on calcein loading, suggesting that the majority of the calcein is attached to the surfaces of the MOFs rather than being stored in the pores and blocking them. The isotherms yielded the following data:

cal@UiO-66-L1 S_{BET} = 1002 m^2g^{-1}; pore volume = 0.469 ccg^{-1}.
cal@UiO-66-L1-PEG550 S_{BET} = 826 m^2g^{-1}; pore volume = 0.421 ccg^{-1}.
cal@UiO-66-L1-PEG2000 S_{BET} = 683 m^2g^{-1}; pore volume = 0.575 ccg^{-1}.

S7. Calcein Release from NMOFs

In a typical calcein release experiment, between 5 and 10 mg of NMOF were dispersed in a dialysis bag with 10 mL of PBS (required pH), and dialysed against 100 mL of PBS (same pH) under magnetic stirring at room temperature. A full spectrum (210-550 nm) was performed for each measurement, which was taken in situ, and the liquid was added back to the dialysis media prior to me next measurement. Both bdc and calcein absorbance characteristic peaks were analysed. For each experiment, calculations were performed with the exact mass of NMOF added.

The previous calibration curve for calcein in PBS at pH 5.5 (λ_{max} = 452 nm, Figure S33a) was used for further analysis. In addition, a calibration curve for calcein in PBS at pH 7.4 was also performed (λ_{max} = 498 nm Figure S38).

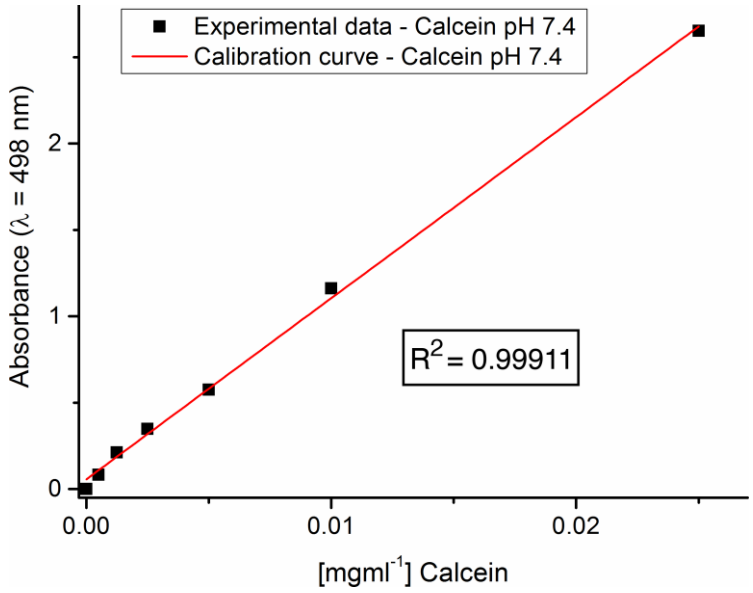

Figure S38. Calibration curve of calcein in PBS pH 7.4

The theoretical maximum calcein absorbance of the dialysis media was determined using the following calculations:

$$mg\ of\ sample * wt\%\ Calcein\ in\ sample = mg\ of\ Calcein \rightarrow \frac{mg}{ml} Calcein$$

$$\rightarrow Maximum\ absorbance$$

$$\frac{\text{Experimental absorbance}}{Maximun\ absorbance} * 100 = \%\ Calcein\ Released$$

The NMOF degradation during the release process was also studied by analysis of the bdc characteristic absorbance peak (λ_{max} = 241 nm). The weight percentage of bdc present in the sample was adjusted with the weight percentage of calcein previously determined by UV-Vis spectroscopy:

$$(wt\%\ BDC\ in\ \mathrm{UiO-66-L1}) * \frac{(100 - \mathrm{wt\%\ Calcein})}{100} = \%\ BDC\ in\ UiO-66-L1-Calcein$$

For PEGylated samples, the weight percentage of bdc was adjusted in the same way, including this time the weight percentage of the PEG units previously determined by TGA:

$$(wt\%\ BDC\ in\ \mathrm{UiO-66-L1}) * \frac{100 - (\mathrm{wt\%PEG} + \mathrm{wt\%\ Calcein})}{100}$$

Then, the former calculations based on the maximum absorbance were performed to obtain the amount of bdc released.

cal@UiO-66-L1

The calcein release from cal@UiO-66-L1 was monitored at pH 5.5 and pH 7.4 by UV/Vis spectroscopy (Figure S39).

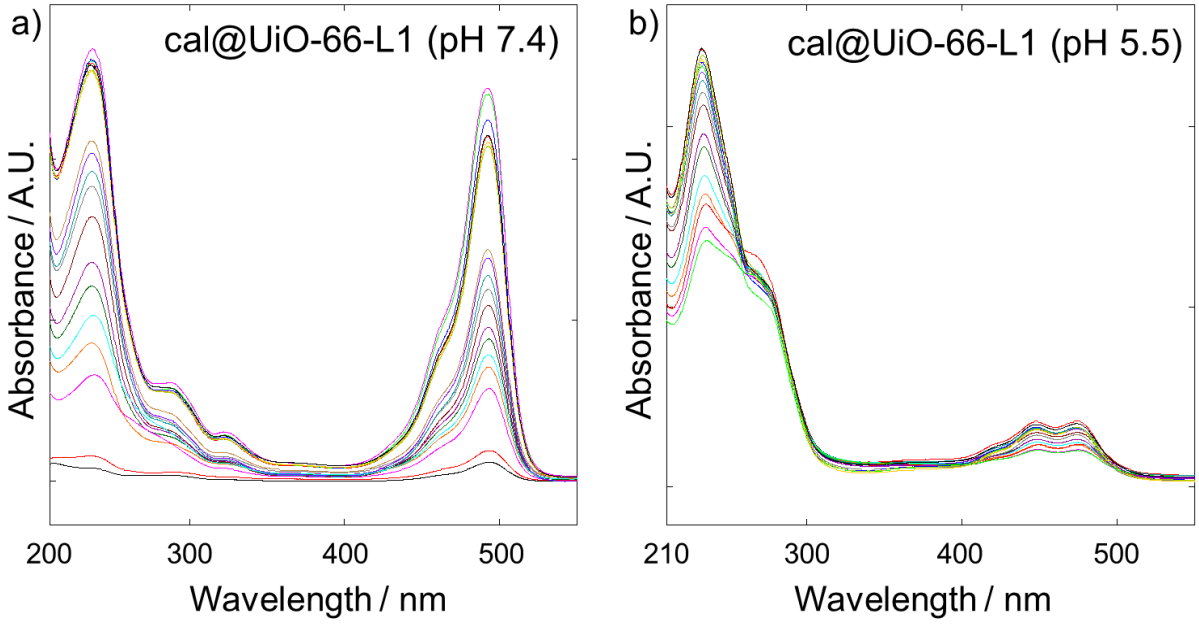

Figure S39. UV-Vis spectra of calcein and bdc release from cal@UiO-66-L1 in PBS at a) pH = 7.4 and b) pH = 5.5.

The release profiles are plotted in Figure S40 with a comparison in Figure S41.

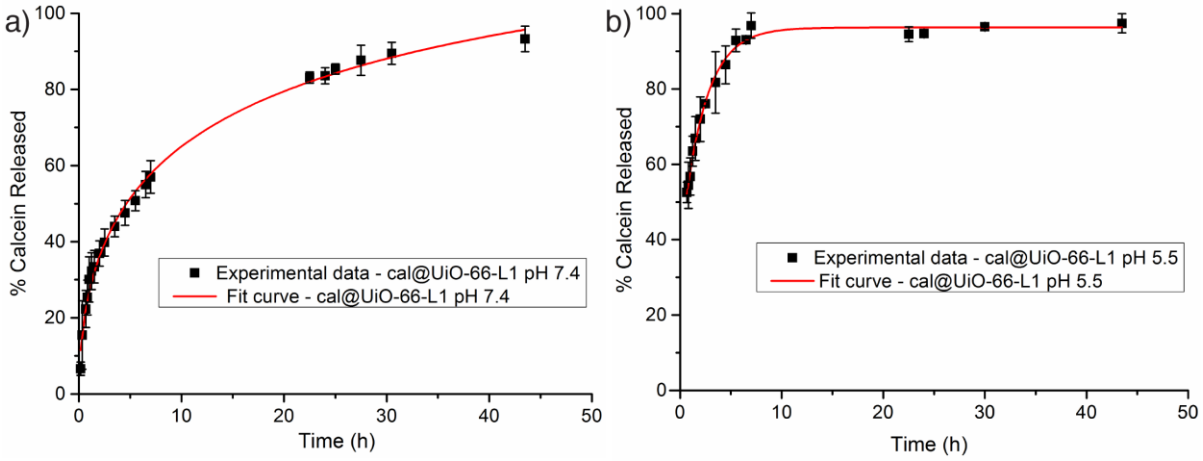

NMOF	Release equation	R^2
cal@UiO-66-L1 pH 7.4	% calcein released = $158.663(t^{0.0505}/1.1286+ t^{0.0505})$	$R^2 = 0.99442$
cal@UiO-66-L1 pH 5.5	% calcein released = $96.325 - 59.4714\ e^{t/2.25915}$	$R^2 = 0.99061$

Figure S40. Calcein release from cal@UiO-66-L1 exhibits a) a sigmoidal profile with the equation $y=V_{max}\ (X^n/K^n+X^n)$ at pH 7.4, and b) an exponential release profile $y= y_0 +A_1e^{x/t1}$ at pH 5.5. Error bars denote standard deviations from triplicate experiments.

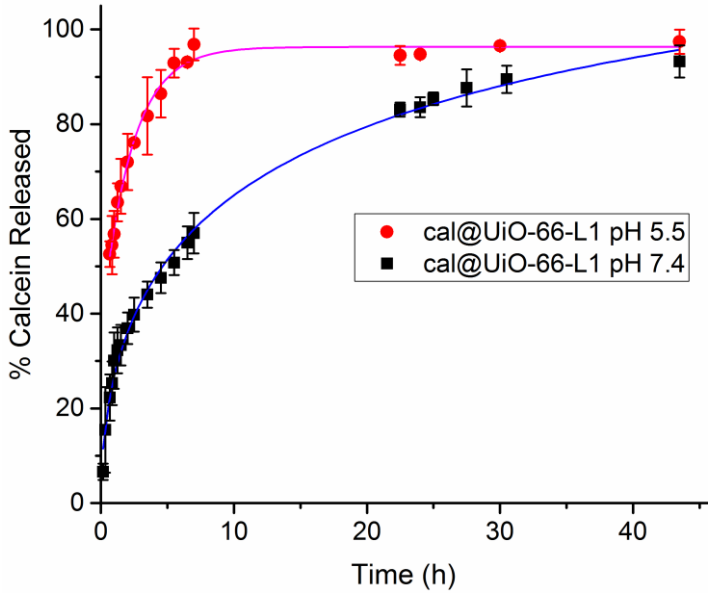

Figure S41. pH Dependence of calcein release from cal@UiO-66-L1. Error bars denote standard deviations from triplicate experiments.

There is a clear difference in the release profiles in the early time stages, with lower pH favouring release as would be expected, but by 24 h the released amounts of calcein are similar.

The rate of release of bdc, and thus information on the degradation of the materials, can also be obtained using this method. From the release profiles (Figure S42), it would appear that the MOF breaks down more rapidly in pH 5.5, which would again be expected.

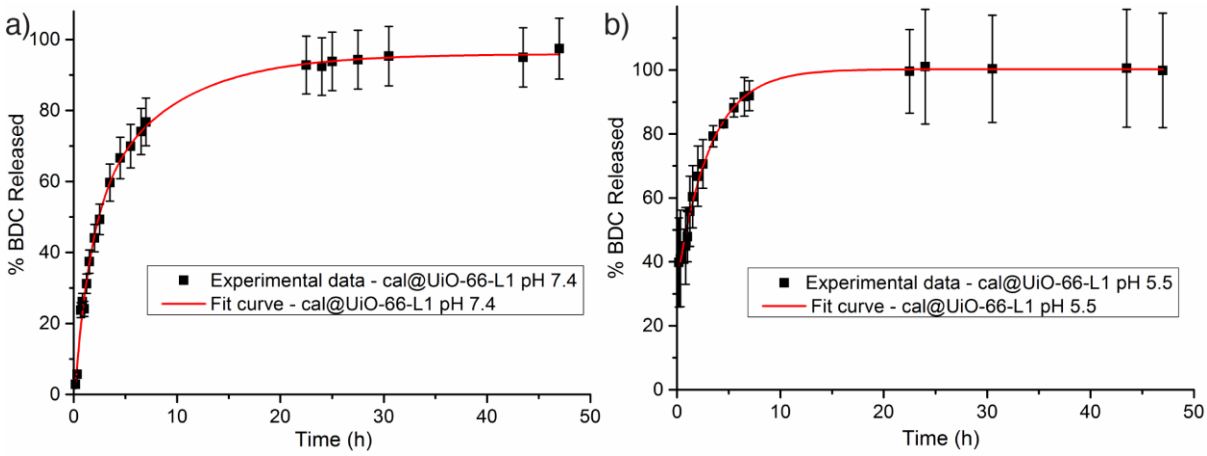

NMOF	Release equation	R^2
cal@UiO-66-L1 pH 7.4	% bdc released = -3.126 + 48.676 e $^{t/7.829}$+ 50.2778 e $^{t/1.5195}$	R^2 = 0.99680
cal@UiO-66-L1 pH 5.5	% bdc released = 100.242 -66.733 e $^{t/3.1814}$	R^2 = 0.99387

Figure S42. Release of bdc linker from cal@UiO-66-L1 exhibits a) an exponential profile with the equation $y= y_0+A_1 (1-e^{-x/t1})+ A_2(1-e^{-x/t2})$ at pH 7.4, and b) an exponential profile $y= y_0 +A_1e^{x/t1}$ at pH 5.5. Error bars denote standard deviations from triplicate experiments.

cal@UiO-66-L1-PEG550 and cal@UiO-66-L1-PEG2000

Similar calcein release experiments were performed for the PEGylated samples, with the UV/Vis spectra for release at pH 7.4 and pH 5.5 plotted for cal@UiO-66-L1-PEG550 in Figure S43 and for cal@UiO-66-L1-PEG550 in Figure S44.

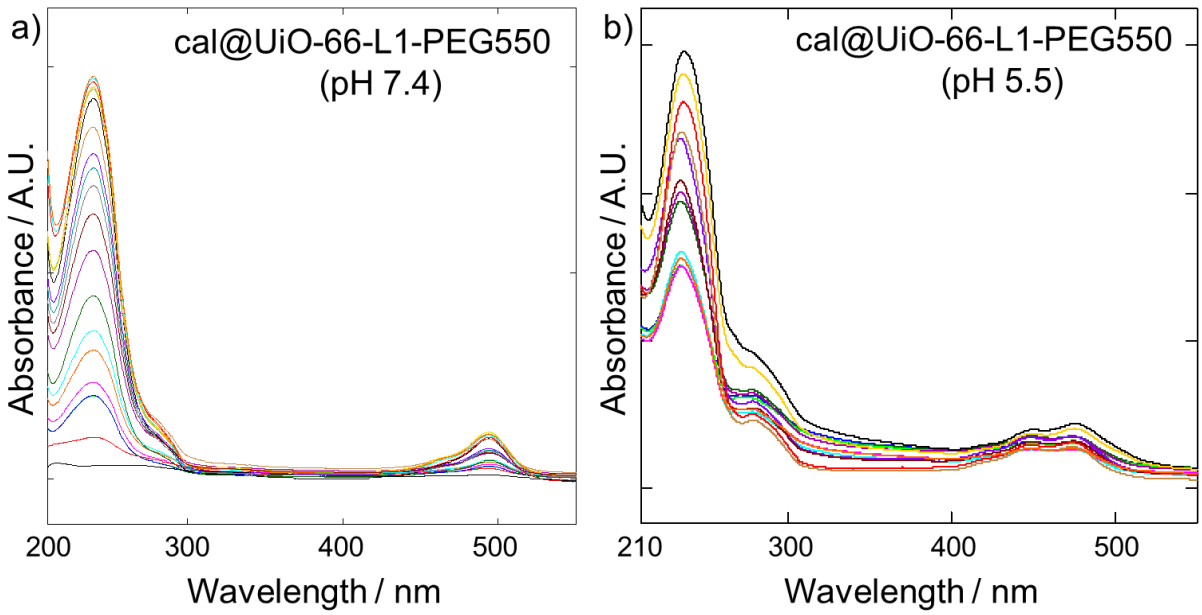

Figure S43. UV-Vis spectra of calcein and bdc release from cal@UiO-66-L1-PEG550 in PBS at a) pH = 7.4 and b) pH = 5.5.

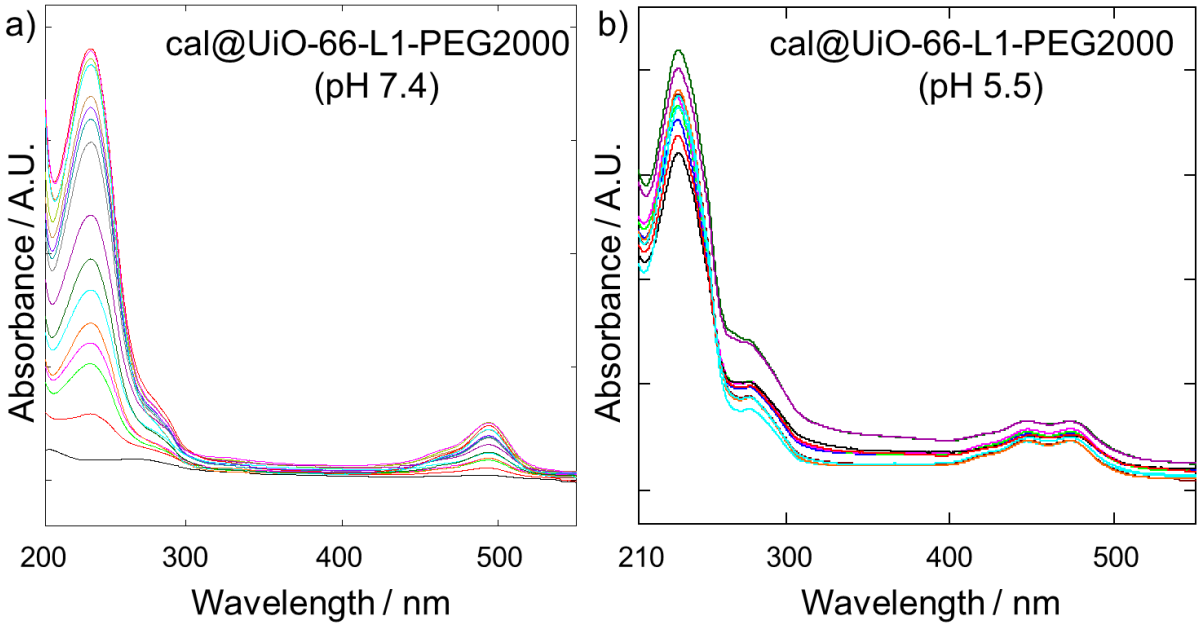

Figure S44. UV-Vis spectra of calcein and bdc release from cal@UiO-66-L1-PEG2000 in PBS at a) pH = 7.4 and b) pH = 5.5.

The calcein release profiles prepared from the UV-Vis spectroscopic data are shown in Figure S45, for the release experiments at pH 7.4, and in Figure S46, for the experiments at pH 5.5.

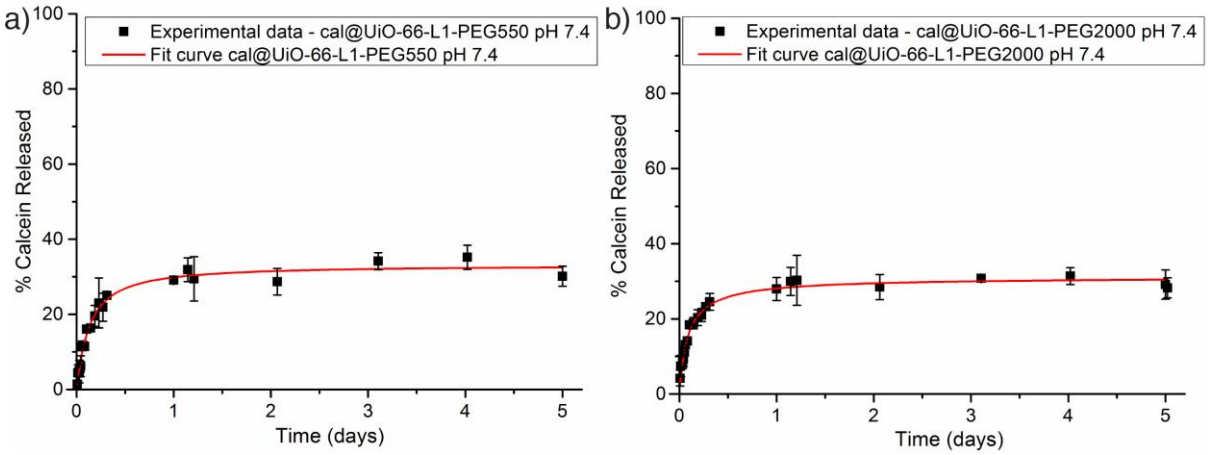

NMOF	Release equation	R^2
cal@UiO-66-L1-PEG550 pH 7.4	% Calcein Released= $33.14264(t^{1.0642}/0.1114+ t^{1.0642})$	R^2= 0.97539
cal@UiO-66-L1-PEG2000 pH 7.4	% Calcein Released= $31.21395(t^{0.90297}/0.1119+ t^{0.90297})$	R^2= 0.99387

Figure S45. Calcein release at pH 7.4 from a) cal@UiO-66-L1-PEG550 and b) cal@UiO-66-L1-PEG2000, which exhibit sigmoidal profiles. Error bars denote standard deviations from triplicate experiments.

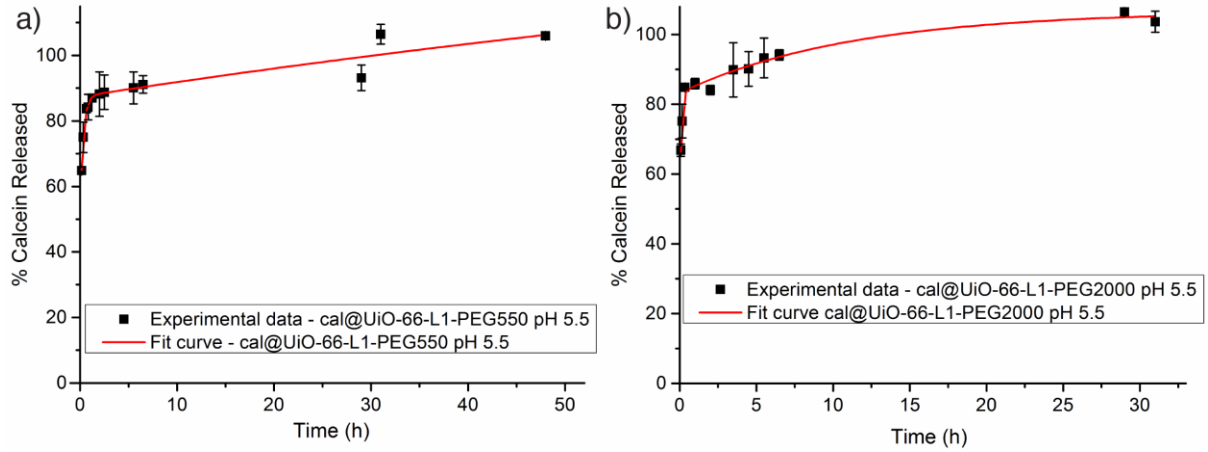

NMOF	Release equation	R^2
cal@UiO-66-L1-PEG550 pH 5.5	% Calcein Released= 48.94399 + 38.48863 $(1-e^{(-t/0.30861)})$ + 70.21881$(1-e^{(-t/153.71876)})$	R^2= 0.91157
cal@UiO-66-L1-PEG2000 pH 5.5	% Calcein Released= 43.52386 + 39.73063 $(1-e^{(-t/0.0987)})$ + 23.4361$(1-e^{(-t/11.16625)})$	R^2= 0.97093

Figure S46. Calcein release at pH 5.5 from a) cal@UiO-66-L1-PEG550 and b) cal@UiO-66-L1-PEG2000, which exhibit sigmoidal profiles. Error bars denote standard deviations from triplicate experiments.

The release profiles for both PEGylated samples are closely related, and show a significant pH dependence. The PEGylated MOFs release around 30% of calcein at pH 7.4, whilst rapidly releasing around 80% of cargo at pH 5.5. This contrasting behaviour is illustrated in Figure S47.

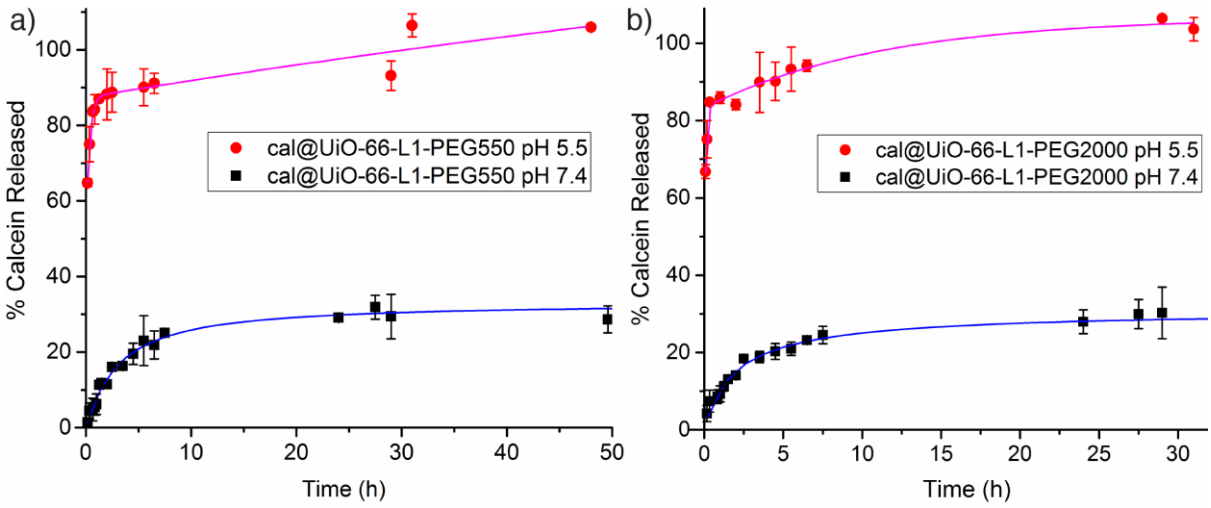

Figure S47. Calcein pH dependence release from PEGylated samples. Error bars denote standard deviations from triplicate experiments.

The release of bdc was also monitored, and is compiled in Figure S48 (pH 7.4) and Figure S49 (pH 5.5). It is clear that degradation occurs much more rapidly at lower pH values, as expected.

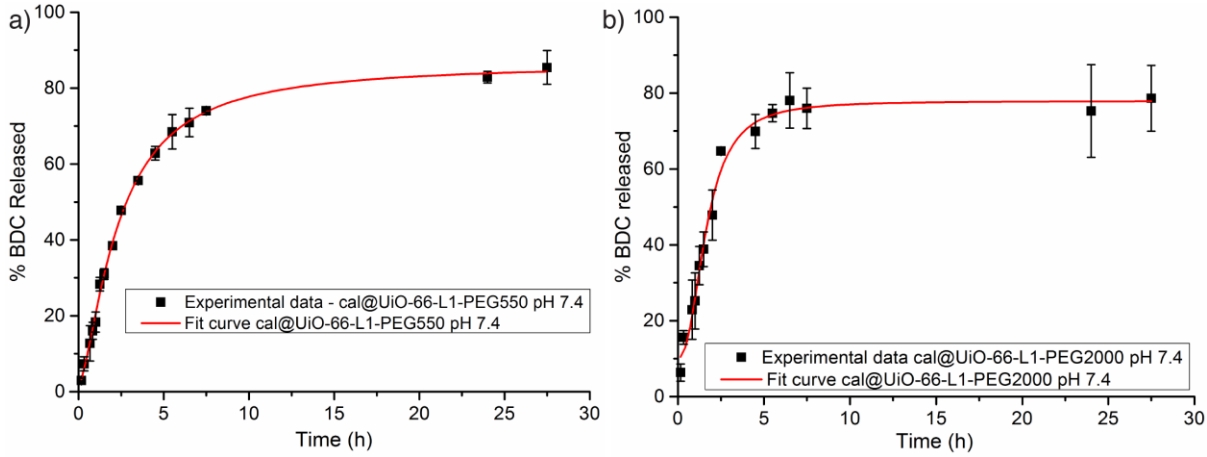

NMOF	Release equation	R^2
cal@UiO-66-L1-PEG550 pH 7.4	% bdc released = 1.24289 + 85.2324 ($t^{1.48297}$/3.4901+ $t^{1.48297}$)	R^2 = 0.99789
cal@UiO-66-L1-PEG2000 pH 7.4	% bdc released = 10.17714 + 67.75258($t^{2.37638}$/3.2658+ $t^{2.37638}$)	R^2 = 0.98549

Figure S48. Release of bdc at pH 7.4 from a) cal@UiO-66-L1-PEG550 and b) cal@UiO-66-L1-PEG2000, which both exhibit sigmoidal profiles with the general equation y= start + (end-start)(x^n/(k^n+x^n)). Error bars denote standard deviations from triplicate experiments.

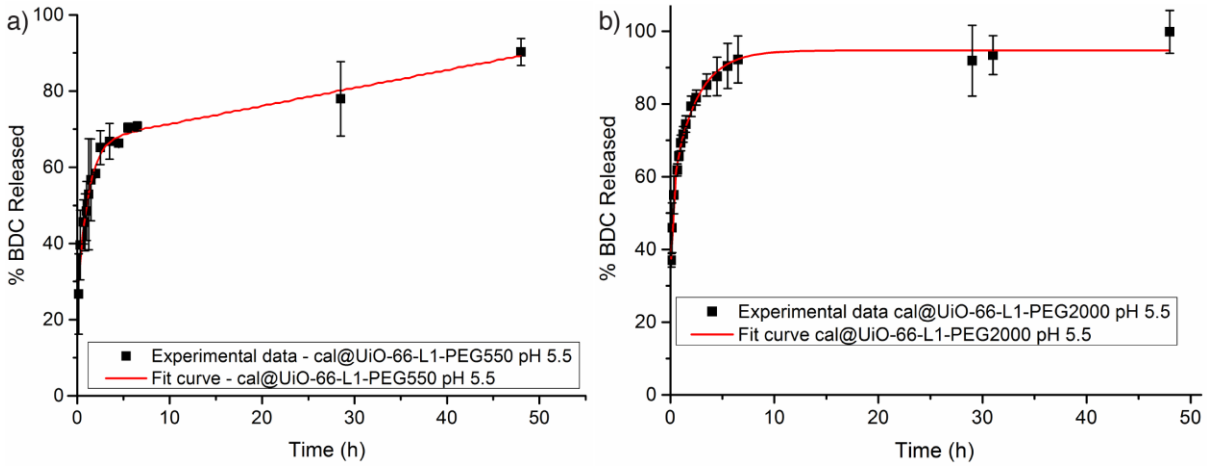

NMOF	Release equation	R^2
cal@UiO-66-L1-PEG550 pH 5.5	% bdc Released= 24.2305 + 42.4435 (1-e $^{(-t/1.1161)}$) + 3.6974E15(1-e$^{(-t/7.806E15)}$)	R^2 = 0.97793
cal@UiO-66-L1-PEG2000 pH 5.5	% bdc Released= 26.59038 + 28.26383 (1-e $^{(-t/0.2338)}$) + 32.89627(1-e$^{(-t/2.32031)}$)	R^2 = 0.98765

Figure S49. Release of bdc at pH 5.5 from a) cal@UiO-66-L1-PEG550 and b) cal@UiO-66-L1-PEG2000, which both exhibit sigmoidal profiles with the general equation y= start + (end-start)(x^n/(k^n+x^n)). Error bars denote standard deviations from triplicate experiments.

PEGylation clearly has a significant effect on calcein release, particularly at pH 7.4, where the coating inhibits calcein release (Figure S50).

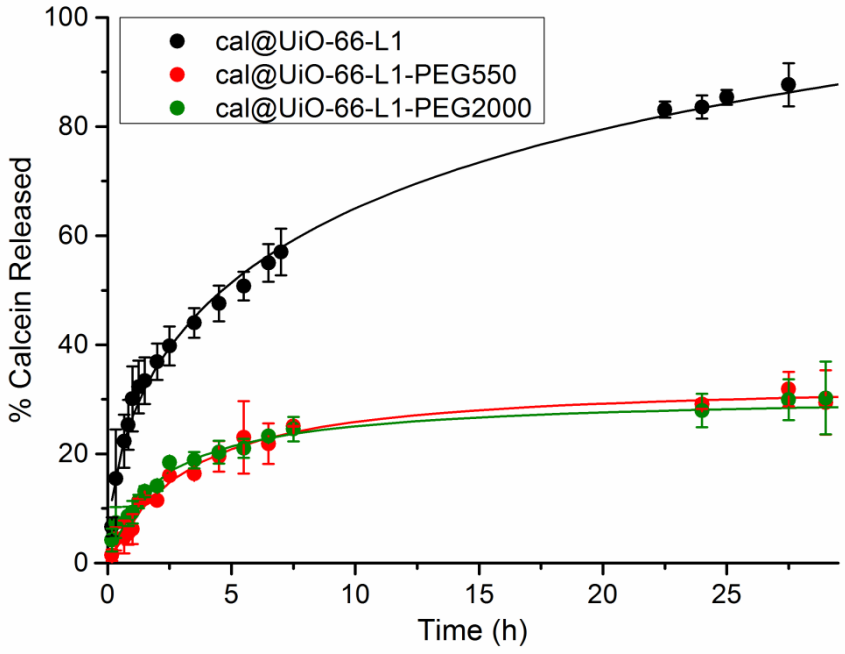

Figure S50. Release of calcein from coated and uncoated UiO-66 at pH 7.4. Error bars denote standard deviations from triplicate experiments.

Stimuli-responsive release of calcein

As the release of calcein from the PEGylated samples reached plateaux after around one day when dispersed in PBS pH 7.4, while a much more significant release was observed at pH 5.5 (Figure S47), a stimuli-responsive release experiment was carried out, where the pH of the release media was adjusted from 7.4 to 5.5 during the course of the experiment to observe if there was further release. To do so, 50 µL of concentrated HCl was added to the 100 mL of PBS pH 7.4 placed in contact with the dialysis bag, in order to obtain pH 5.5. The quantity of concentrated HCl need to change the pH of the dialysis media was determined previous to the experiment. The pH responsive release profile is shown in the main paper in Figure 5.

S8. Characterisation of NMOFs after Calcein Release

To simulate release conditions on a larger scale, 50 mg samples of the calcein-loaded NMOFs were dispersed in 50 mL of PBS pH 7.4, which was stirred at room temperature for 2 days in the case of cal@UiO-66-L1-PEG2000 and for 1 day for cal@UiO-66-L1. Then, the NMOF was collected by centrifugation (4500 rpm, 15 minutes), and washed with water 3 times. The NMOFs were dried for 24 hours under vacuum before further analysis.

PXRD showed that the samples retained some crystallinity, although were somewhat degraded by the release process, likely as a consequence of the extended exposure to phosphates in PBS (Figure S51).

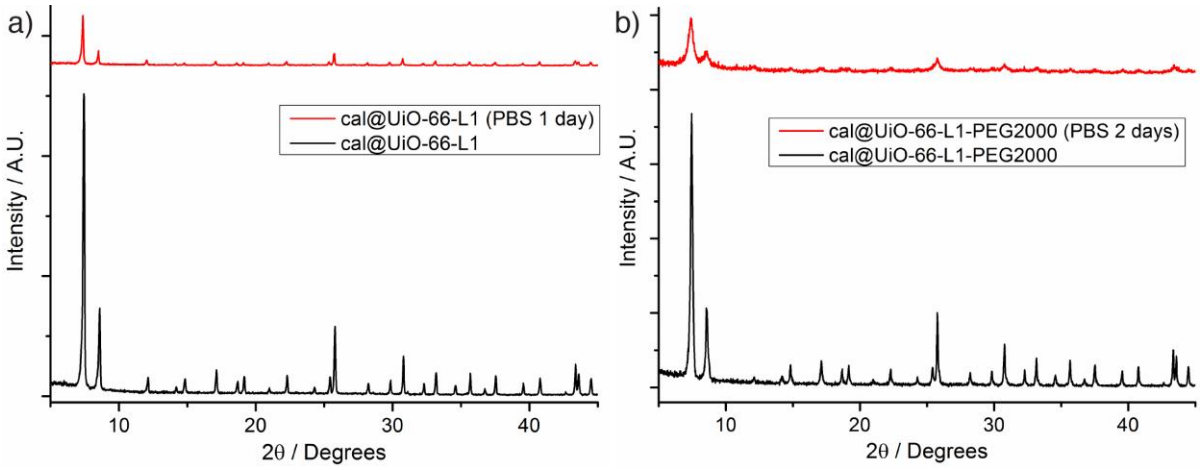

Figure S51. Stacked PXRD patterns of NMOFs before and after simulated release conditions.

Thermogravimetric analysis of the samples in air showed that for cal@UiO-66-L1, a significant amount of calcein had been released (Figure S52a), leaving a higher overall metal oxide residue. For cal@UiO-66-L1-PEG2000, the mass loss events attributed to the PEG chains are not present, suggesting that the PEG chains have been cleaved from the MOF during the exposure to PBS (Figure S52b).

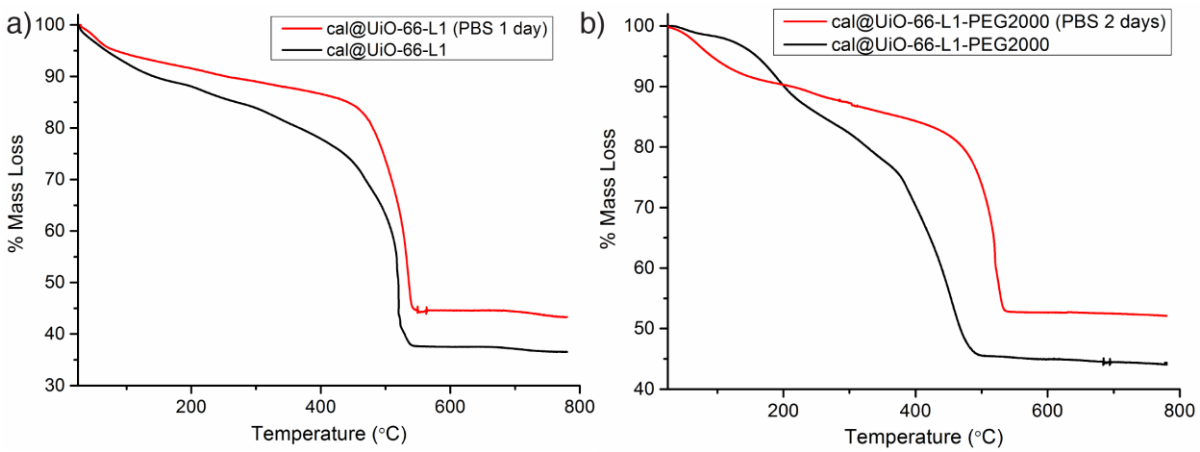

Figure S52. TGA tracess in air of a) cal@UiO-66-L1 and b) cal@UiO-66-L1-PEG2000, before and after release.

The residual calcein content was measured by the UV/Vis spectroscopic method described in Section S6. The uncoated sample cal@UiO-66-L1 contained 5.2% *w/w* calcein after 1 day in PBS, corresponding to 67.5% release. In contrast, cal@UiO-66-L1-PEG2000 contained 5.4% *w/w* calcein after 2 days in PBS, corresponding to 42.7% release. These values correlate well with the smaller scale release profiles in Section S7.

Adsorption isotherms for N_2 at 77 K were collected for the samples (Figure S53), which both showed that after the release, the MOFs retained some porosity. The following surface area data were obtained, and compared to the pristine starting materials collected in Section S6:

cal@UiO-66-L1 S_{BET} = 1002 m^2g^{-1}; pore volume = 0.469 ccg^{-1}.
cal@UiO-66-L1 (1 day in PBS) S_{BET} = 1155 m^2g^{-1}; pore volume = 0.666 ccg^{-1}.
cal@UiO-66-L1-PEG2000 S_{BET} = 683 m^2g^{-1}; pore volume = 0.575 ccg^{-1}.
cal@UiO-66-L1-PEG2000 (2 days in PBS) S_{BET} = 554 m^2g^{-1}; pore volume = 0.442 ccg^{-1}.

The unmodified material shows an increase in gravimetric surface area and pore volume, likely as a result of the release of calcein mass. In contrast, cal@UiO-66-L1-PEG2000 shows a decrease in gravimetric surface area, despite releasing some calcein. We attribute this to an increase in mass resulting from formation of a phosphate corona (from the PBS buffer) at the surfaces of the particles, which is initially aided by the presence of the PEG chains. We expect that the incorporation of these phosphates blocks the release of further calcein.

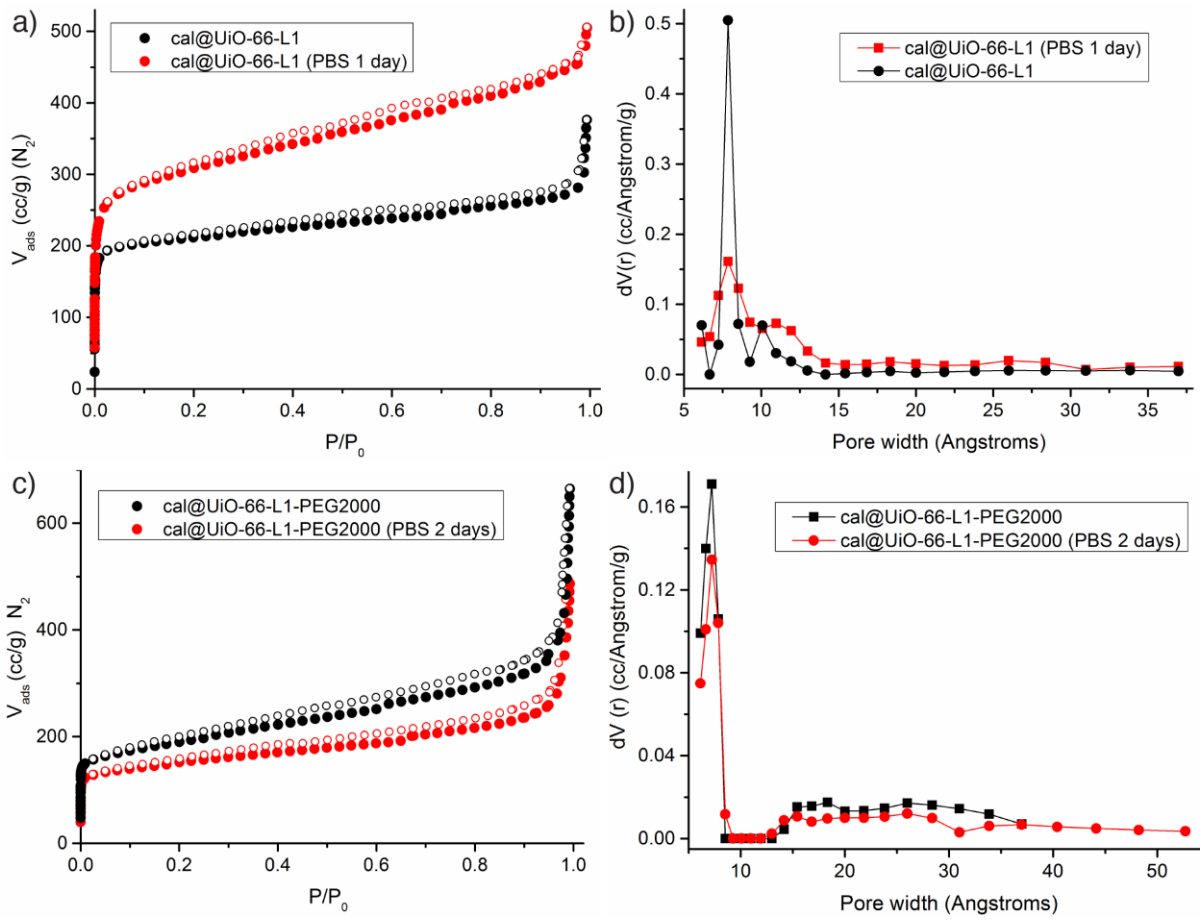

Figure S53. a) N_2 adsorption isotherm (77 K) for cal@UiO-66-L1 after 1 day in PBS compared to the pristine material, alongside b) the calculated pore size distributions (slit pore, N_2 at 77 K on carbon, QSDFT equilibrium model). c) N_2 adsorption isotherm (77 K) for cal@UiO-66-L1-PEG2000 after 2 days in PBS compared to the pristine material, alongside d) the calculated pore size distributions (slit pore, N_2 at 77 K on carbon, QSDFT equilibrium model).

The incorporation of phosphates into the materials can be monitored by FTIR spectroscopy (Figure S54). The growing broad signal at ~1000 cm^{-1} is present in both samples after 2 days, indicating that phosphate accumulation occurs in PBS. However, UiO-66-L1 is able to release the majority of its calcein before significant phosphate incorporation, while UiO-66-L1-PEG2000 is likely to have its release of calcein delayed by the PEG2000 chains and then blocked by phosphate.

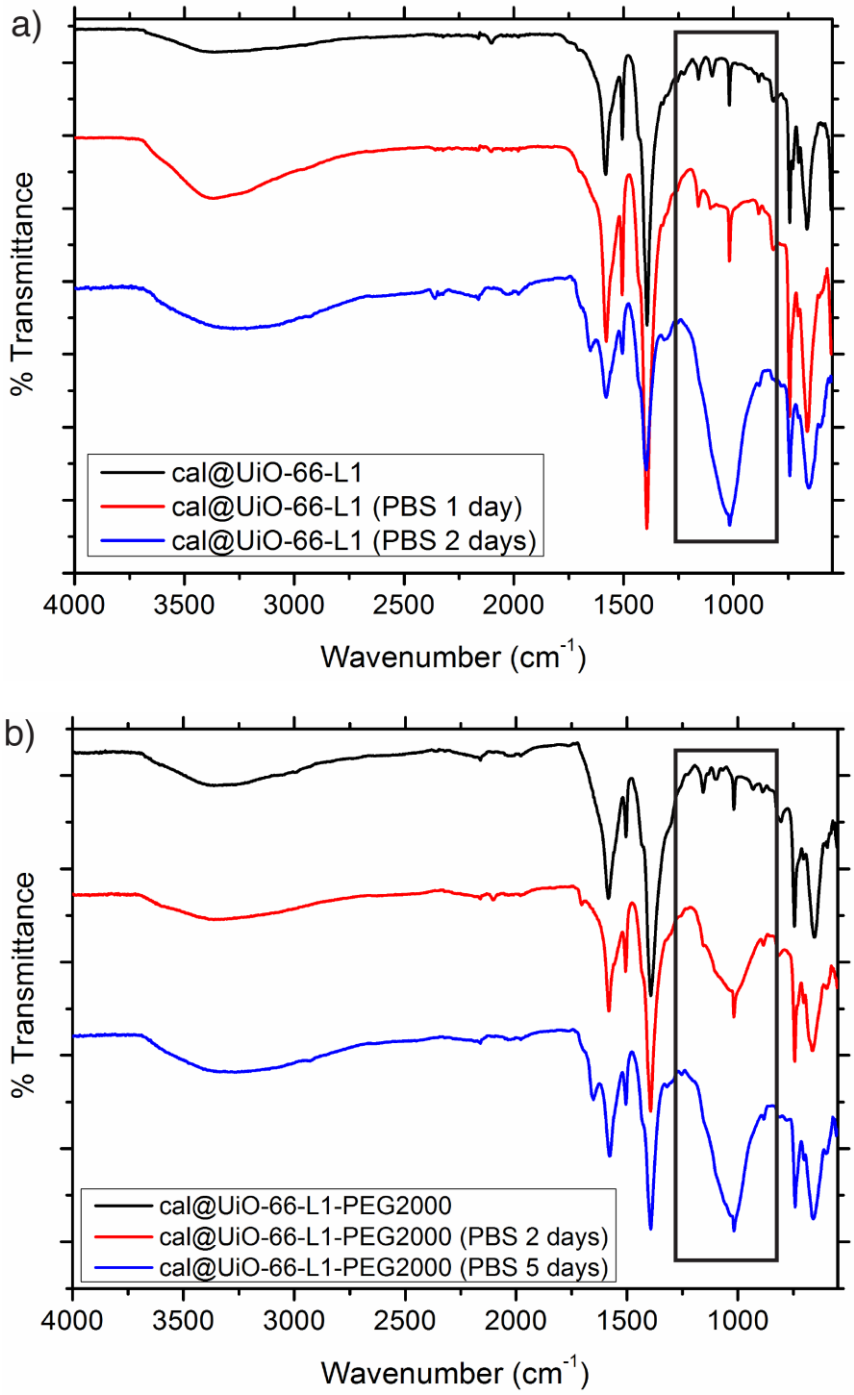

Figure S54. Stacked FTIR spectra of a) cal@UiO-66-L1 compared to the sample after 1 and 2 days simulated release conditions, and b) cal@UiO-66-L1-PEG2000 compared to the sample after 2 and 5 days simulated release conditions.

S9. Endocytosis Studies

Confocal microscopy for cell uptake

For all the confocal microscopy experiments HeLa cells were seeded in a NUNC™ imaging four-well plate at a density of 1.11 x 10^5 cells/mL and incubated for 24 h at 37 ºC with 5% CO_2 in cDMEM. After that the cells were then washed with PBS and incubated with 0.25 mg/mL of MOF in media, the corresponding calcein concentration in media, or only media as a control, for 2 h at 37 ºC with 5% CO_2 in cDMEM. Subsequently, the cells were washed with PBS, and staining solution was added to the wells. The staining solution consisted of 5 µg/mL Hoescht 33342 nuclear stain and 5 µg/mL plasma membrane stain CellMask™ Orange. Cells were incubated for 5 minutes with the staining solution in the absence of light, after which trypan blue (0.4%) was added to quench any external fluorescence. The cells were washed with PBS three further times. Finally, fresh media without phenol red was added to each sample. The four-well plate was placed on a Leica TCS SP5 confocal microscope to be imaged. The microscope was equipped with 405 diode, argon and HeNe lasers. Leica LAS AF software and ImageJ were used to analyze the images, which are shown in Figure 6 in the main manuscript.

The cell morphology changed during the course of the experiment as observed for the control sample, where the cells were incubated only with media. This could be explained due to the necessary multiple PBS washes to completely remove non-internalised MOFs and fluorescent stains.

Flow cytometry assays (FACS)

In all the FACS experiments, HeLa cells were seeded in a Cellstar 24-well plate at a density of 5 x 10^4 cells/well and incubated for 48 h at 37 ºC with 5% CO_2 in complete medium.

Positive controls

After cell growing for 48 h, each well containing cells was washed with PBS and pre-treated with sucrose (102.7 mg/mL, 0.3 M), chlorpromazine (31.9 µg/mL, 100 µM), nystatin (250 µg/mL), and rottlerin (2.6 µg/mL, 5 µM) for 30 min at 37 ºC. Subsequently, endocytosis tracers (transferrin-AlexaFluor-633, 25 µg/mL; BODIPY TR-ceramide, 3.5 µg/mL; and Texas Red-dextran-10 kDa, 0.5 mg/mL) known to specifically go through the clathrin, caveolae, and macropinocytosis pathways respectively, were added and incubated for another 1.5 h. After each treatment, the medium of each well was aspirated and the wells were washed extensively to remove all the conditions. The cells were then harvested by adding 0.1 mL of trypsin and incubated for 5 min at 37 ºC with 5% CO_2. Cells were recovered by centrifugation

(5 min at 1200 rpm) and re-suspended in 100 µL of complete medium without phenol red. Finally the samples were measured in a Cytek DxP8 analyser cytometer within 30 min. The analysis of the data was done using FlowJo and Prism software (Figure S55).

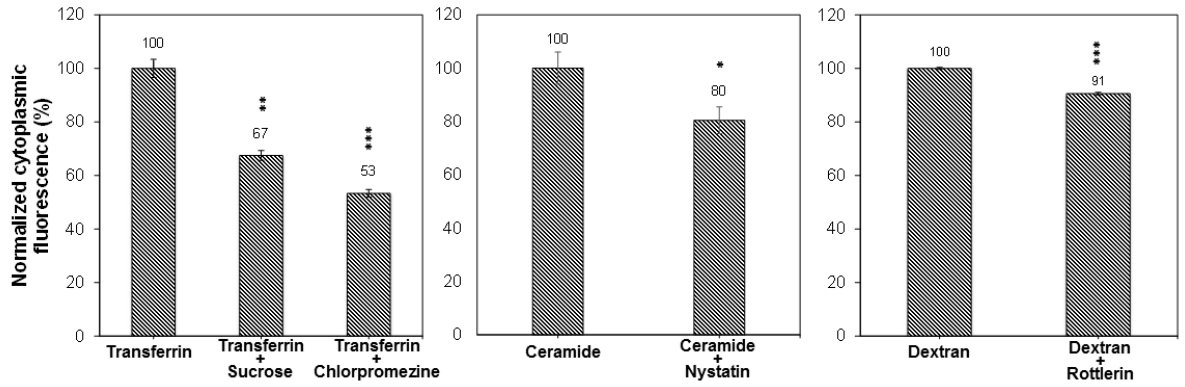

Figure S55. FACs of the positive controls of desired endocytosis routes, showing statistical difference for the concentration of tracers used.

Analysis of the endocytosis pathways of coated and uncoated NMOFs

In a similar way to the positive controls, at 80% cell confluency, each well was washed with PBS and pre-treated with sucrose (102.7 mg/mL, 0.3 M), chlorpromazine (31.9 µg/mL, 100 µM), nystatin (250 µg/mL), or rottlerin (2.6 µg/mL, 5 µM) for 30 min at 37 ºC. Then, either UiO-66-L1, UiO-66-L1-PEG550, or UiO-66-L1-PEG2000, were added and incubated for another 1.5 h. Subsequently, samples were measured by flow cytometry.

In all the FACS experiments, after any treatment, the media of each well was aspirated and the wells were washed extensively to remove all the conditions. The cells were then harvested by adding 0.1 mL of trypsin and incubated for 5 min at 37 ºC with 5% CO_2. The cells were recovered by centrifugation, 5 min at 1200 rpm, and re-suspended in 100 µl of cDMEM without phenol red. Finally the samples were measure in a Cytek DxP8 analyzer cytometer within 30 min. The analysis of the data was done using FlowJo and Prism software and is reported in the main text in Figure 7.

Confocal microscopy for co-localization

For all the co-localization experiments, HeLa cells were seeded in a NUNC^{TM} imaging four-well plate at a density of 1.11 x 10^5 cell/mL and incubated for 24 h at 37 ºC with 5% CO_2 in cDMEM. At the end of the incubation period the four-well plate was placed on a Leica TCS SP5 confocal microscope to be imaged. The microscope was equipped with 405 diode, argon and HeNe lasers. Leica LAS AF software was used to analyse the images.

LysoTracker®-Deep red imaging

The cells were then washed with PBS and incubated with 0.5 mg/mL of UiO-66-L1, UiO-66-L1-PEG550, or UiO-66-L1-PEG2000, along with LysoTracker®-Deep red for 2 h at 37 ºC with 5% CO_2 in cDMEM. Subsequently, the cells were washed with PBS to remove the conditions, with trypan blue (0.4%) to quench any external fluorescence, and again three times with PBS. Finally, fresh media without phenol red was added to each sample.

On the one hand, calcein cannot cross the cell membrane alone, on the other hand, it self-quenches, and so the green fluorescence is only observed upon release of calcein from the internalised NMOF. Despite the fact that the release profiles determined that PEGylated UiO-66 samples only release ~15% of calcein at pH 7.4 after 2 hours of exposure, the green fluorescence is clearly visible outside the lysosome, suggesting a proportion of cal@UiO-66-L1-PEG2000 is internalised by a different uptake mechanism (in the more acidic lysosome 85% of calcein would be expected to be released in pH 5.5 at the same exposure time).

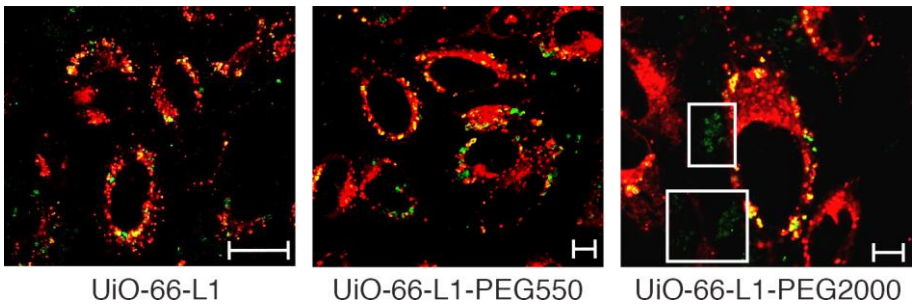

Figure S56. Confocal fluorescence microscopy images of NMOF uptake into HeLa cells using a lysotracker (red) to stain the lysosome and showing calcein internalisation (green). Non-lysosomal calcein is highlighted in white boxes for UiO-66-L1-PEG2000. Scale bars represent 25 μm, 10 μm and 7.5 μm, from left to right.

S10. Therapeutic Efficacy of Drug-Loaded NMOFs

To assess the ability of the surface functionalised UiO-66 nanoparticles to deliver cytotoxic agents into cells, the known anticancer drug dichloroacetic acid (DCA)[S11] was incorporated into solvothermal syntheses of UiO-66 and UiO-66-L1 in place of acetic acid, yielding DCA@UiO-66 and DCA@UiO-66-L1. The presence of L1 and DCA in DCA@UiO-66-L1 was confirmed by ^{1}H NMR spectroscopy of digested samples (Figure S57).

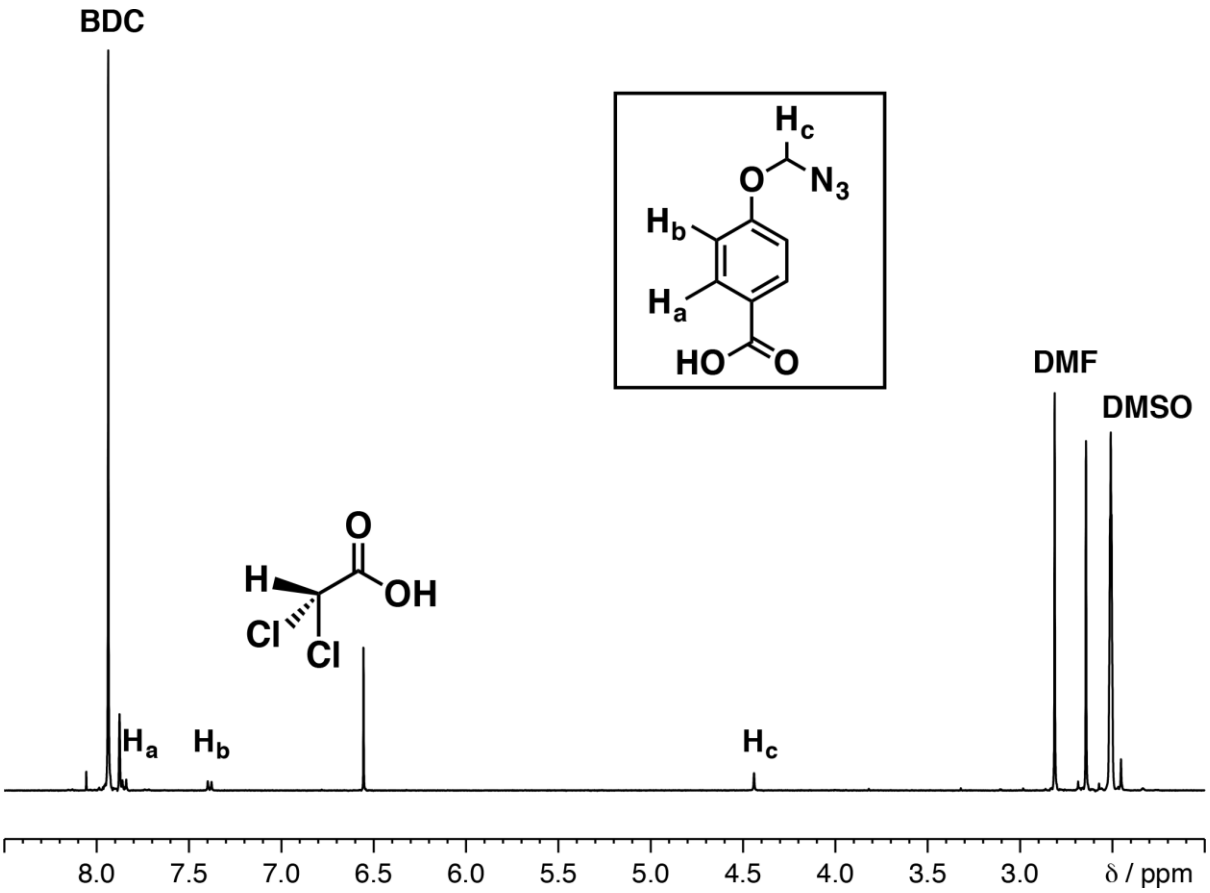

Figure S57. ^{1}H NMR spectrum (D_2SO_4 / DMSO-d_6, 293 K) of DCA@UiO-66-L1, showing the presence of the modulator L1 and DCA.

The crystallinity of the samples was confirmed by PXRD (Figure S58a) and DCA@UiO-66-L1 was found to consist of nanoparticles around 150 nm in diameter by SEM (Figure S58b). The same CuAAC procedure detailed in Section S4 was used to surface functionalise DCA@UiO-66-L1 with the longer PEG chain, yielding DCA@UiO-66-L1-PEG2000, which did not affect crystallinity.

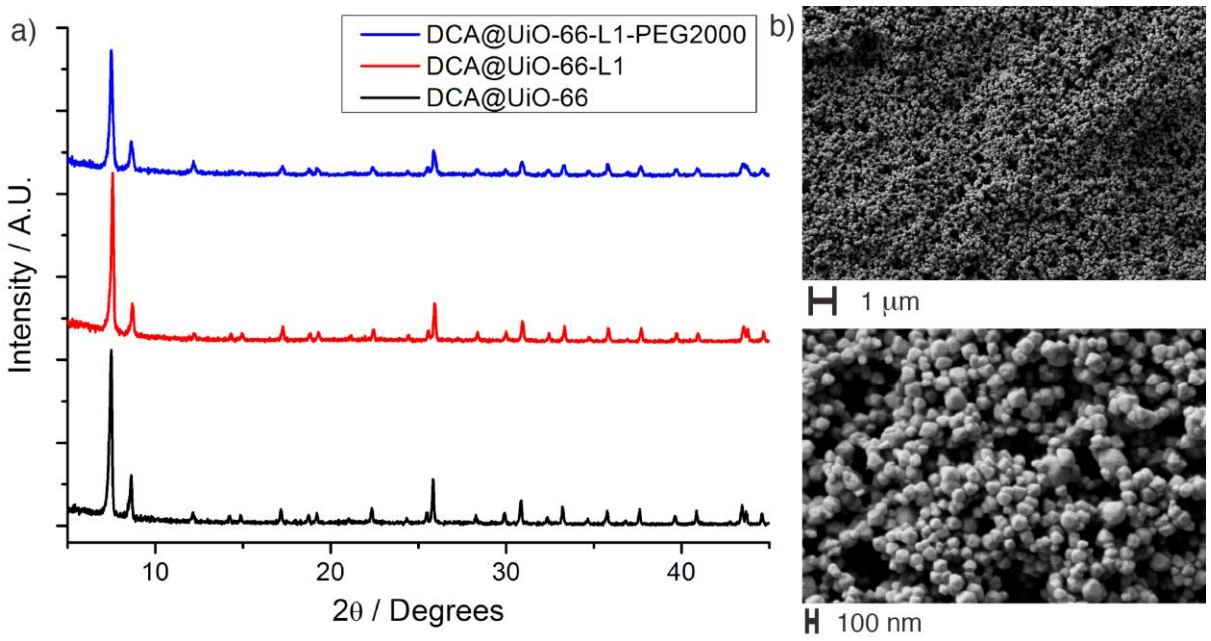

Figure S58. a) PXRD patterns of UiO-66 samples loaded with DCA. b) SEM micrographs of as synthesised DCA@UiO-66-L1.

The DCA content of the samples was assessed by TGA and by inductively coupled plasma mass spectrometry (ICP-MS) determination of chloride content (Figure S59).

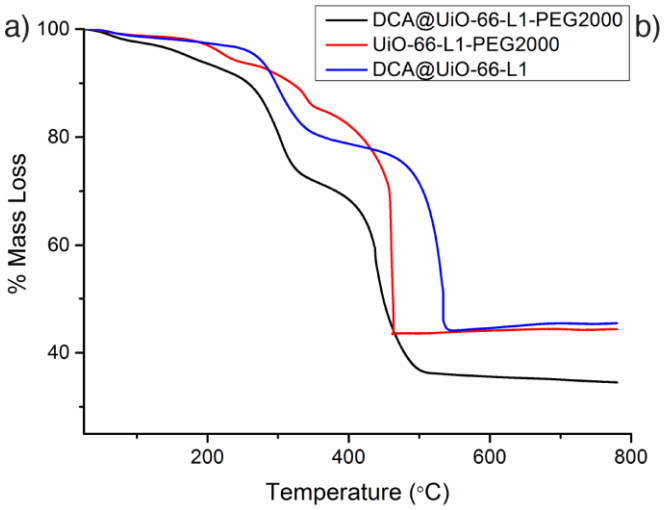

b)

	DCA Loading (wt%)	
	TGA	ICP-MS
DCA@UiO-66	17.5%	14.7%
DCA@ UiO-66-L1	15.8%	13.7%
DCA@UiO-66-L1-PEG2000	n/a	12.1%

Figure S59. a) TGA traces for DCA loaded UiO-66 samples compared to UiO-66-L1-PEG2000, confirming the presence of both DCA and PEG chains in DCA@UiO-66-L1-PEG2000. b) Comparison of DCA loading values for the samples calculated by TGA and ICP-MS.

Close correlation between the DCA loading values derived from TGA mass loss events and ICP-MS was observed, with a gradual decrease in DCA loading occurring as the mass of the

surface functionality increased, as would be expected. The TGA values are likely slightly higher than the ICP-MS values due to other mass loss events occurring alongside the DCA thermal decomposition. While TGA analysis confirmed the presence of the PEG functionality in DCA@UiO-66-L1-PEG2000, the mass loss events for DCA and the PEG chains occurred simultaneously, precluding calculation of DCA loading, and so the ICP-MS methodology was used.

To determine cytotoxicity, MTS assays were again performed on HeLa cells incubated with DCA@UiO-66-L1 and DCA@UiO-66-L1-PEG2000. The results are presented in the main text in Figure 8, showing the PEGylated materials are more toxic than the unfunctionalised derivatives, presumably because of enhanced lysosome-escaping capabilities and stability. The effect is even more prevalent when the data are presented by dose of DCA rather than MOF (Figure S60), as the PEGylated materials contain less DCA by weight. The therapeutic efficacy of DCA is greatly enhanced by delivery within the PEGylated NMOF.

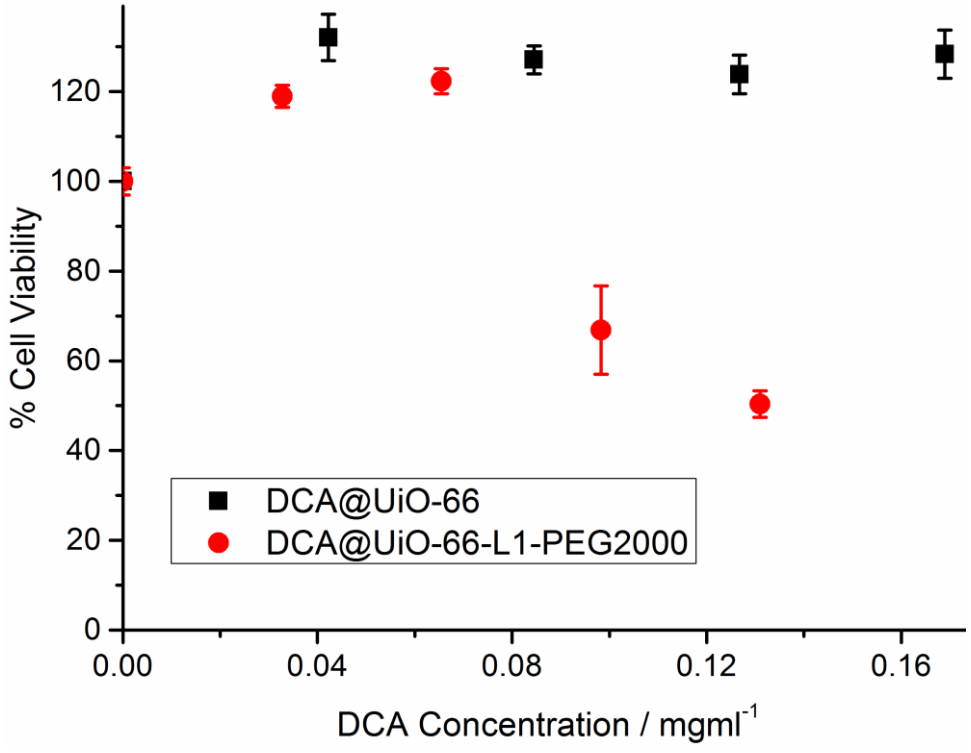

Figure S60. Metabolic activity of HeLa cells after 72 h of exposure to DCA@UiO-66-L1 and DCA@UiO-66-L1-PEG2000, measured by MTS assay.

S11. References

(S1) Wrobel, M.; Aubé, J.; König, B. (2012). Parallel solid-phase synthesis of diaryltriazoles. Beilstein J. Org. Chem. *8*, 1027.

(S2) Pandey, S.; Kolli, B.; Mishra, S. P.; Samui, A. B. (2012). Siloxane polymers containing azo moieties synthesized by click chemistry for photo responsive and liquid crystalline applications. J. Polym. Sci. A Polym. Chem. *50*, 1205.

(S3) Wu, H.; Chua, Y. S.; Krungleviciute, V.; Tyagi, M.; Chen, P.; Yildirim, T.; Zhou, W. (2013). Unusual and Highly Tunable Missing-Linker Defects in Zirconium Metal–Organic Framework UiO-66 and Their Important Effects on Gas Adsorption. J. Am. Chem. Soc. *135*, 10525.

(S4) He, X.-P.; Zeng, Y.-L.; Zang, Y.; Li, J.; Field, R. A.; Chen, G.-R. (2016). Carbohydrate CuAAC click chemistry for therapy and diagnosis. Carbohydr. Res. *429*, 1.

(S5) Ryu, M.-H.; Choi, J.-W.; Kim, H.-J.; Park, N.; Cho, B.-K. (2011). Complementary Hydrogen Bonding Between a Clicked C3-Symmetric Triazole Derivative and Carboxylic Acids for Columnar Liquid-Crystalline Assemblies. Angew. Chem. Int. Ed. *50*, 5737.

(S6) Katz, M. J.; Brown, Z. J.; Colon, Y. J.; Siu, P. W.; Scheidt, K. A.; Snurr, R. Q.; Hupp, J. T.; Farha, O. K. (2013). A facile synthesis of UiO-66, UiO-67 and their derivatives. Chem. Commun. *49*, 9449.

(S7) Cavka, J. H.; Jakobsen, S.; Olsbye, U.; Guillou, N.; Lamberti, C.; Bordiga, S.; Lillerud, K. P. (2008). A New Zirconium Inorganic Building Brick Forming Metal Organic Frameworks with Exceptional Stability. J. Am. Chem. Soc. *130*, 13850.

(S8) Shao, C.; Wang, X.; Zhang, Q.; Luo, S.; Zhao, J.; Hu, Y. (2011). Acid-base jointly promoted copper(I)-catalyzed azide-alkyne cycloaddition. J. Org. Chem. *76*, 6832.

(S9) Orellana-Tavra, C.; Baxter, E. F.; Tian, T.; Bennett, T. D.; Slater, N. K. H.; Cheetham, A. K.; Fairen-Jimenez, D. (2015). Amorphous metal-organic frameworks for drug delivery. Chem. Commun. *51*, 13878.

(S10) Sebby, K. B.; Mansfield, E. (2015). Determination of the surface density of polyethylene glycol on gold nanoparticles by use of microscale thermogravimetric analysis. Anal. Bioanal. Chem. *407*, 2913.

(S11) Bonnet, S.; Archer, S. L.; Allalunis-Turner, J.; Haromy, A.; Beaulieu, C.; Thompson, R.; Lee, C. T.; Lopaschuk, G. D.; Puttagunta, L.; Bonnet, S.; Harry, G.; Hashimoto, K.; Porter, C. J.; Andrade, M. A.; Thebaud, B.; Michelakis, E. D. (2007). A Mitochondria-K^+

Channel Axis Is Suppressed in Cancer and Its Normalization Promotes Apoptosis and Inhibits Cancer Growth. Cancer Cell *11*, 37.